Optimal integration of wind energy with a renewable based microgrid for industrial applications

HALLA NASER AL MOSTAFA

SUPERVISORS
Sathyajith Mathew
Ghali Yakoub

University of Agder, 2022
Faculty of Engineering and Science
Department of Engineering Sciences

Abstract

Wind energy in urban environments is a rapidly developing technology influenced by the terrain specifications, local wind characteristics and urban environments such as buildings architecture. The urban terrain is more complex than for open spaces and has a critical influence on wind flow at the studied site. This approach proposes an integration of the surrounding buildings in the studied site and then simulating the wind flow, considering both simple and advanced turbulence models to quantify and simulate the wind flow fields in an urban environment and evaluate the potential wind energy. These simulations are conducted with an accessible computational fluid dynamic tool (Windsim) implementing available commercial wind turbines and performed on a case study at Agder county in the southern part of Norway for an industrial facility specialized in food production. Several simulations were considered and repeated to achieve a convergence after adding the buildings to the domain, which mainly simulates the wind flow patterns, power density, and annual energy production. These simulations will be compared with previous results, which adapted different manipulation techniques applied on the same site where the elevation and roughness data were manipulated to mimic the actual conditions in the studied urban site. The current approach (adding the buildings) showed a reduction in the average wind speed and annual energy production for certain levels with increased turbulence intensity surrounding the buildings. Moreover, a feasibility study is conducted to analyze the techno-economic of the facility's hybrid system, including the planned installation of a wind energy system using commercial software (HOMER). The simulation results indicated that HOMER is conservative in estimating the annual energy production of both wind and solar power systems. Nevertheless, the analysis showed that integrating a wind turbine of 600 kW would significantly reduce the dependence on the grid and transform the facility into a prosumer with more than 1.6 GWh traded with the grid annually. However, the proposed system's net present cost would be 1.43 M USD based on installation, maintenance, and trading with the grid, without including self-consumption, which counts for approximately 1.5 GWh annually. Moreover, the proposed system has a low levelized cost of energy of 0.039$ per kWh, which is slightly above the levelized cost of wind energy but 2 to 4 times less than the installed solar panels.

Preface

This thesis is submitted for the degree of Master of Engineering and Science at the University of Agder. It is written as part of a two-year master's program in Renewable Energy. The research described herein is conducted under the supervision of Professor Sathjajith Mathew

Acknowledgement

Several persons have contributed academically, practically and with support to this master thesis. Firstly, I would like to thank my head supervisor, Prof. Sathjajith Mathew and co-supervisor PhD candidate Ghali Yakoub for their time, valuable input, and support throughout the entire master's period. Furthermore, I would like to thank Svendsengruppen AS (Gorines), particularly Simon Tjomsland and Kjell Rune Nakkestad, for their immense help throughout the entire process of providing necessary information and the required data for the project. Finally, I would like to thank my family and friends for being helpful and supportive during my time studying at the University of Agder.

May 2022

Individual/group Mandatory Declaration

The individual student or group of students is responsible for the use of legal tools, guidelines for using these and rules on source usage. The statement will make the students aware of their responsibilities and the consequences of cheating. Missing statement does not release students from their responsibility.

1.	I/We hereby declare that my/our report is my/our own work and that I/We have not used any other sources or have received any other help than mentioned in the thesis.	☒
2.	I/we further declare that this thesis: - has not been used for another exam at another department/university/university college in Norway or abroad; - does not refer to the work of others without it being stated; - does not refer to own previous work without it being stated; - have all the references given in the literature list; - is not a copy, duplicate or copy of another's work or manuscript.	☒
3.	I/we am/are aware that violation of the above is regarded as cheating and may result in cancellation of exams and exclusion from universities and colleges in Norway, see Universitets- og høgskoleloven §§4-7 og 4-8 og Forskrift om eksamen §§ 31.	☒
4.	I/we am/are aware that all submitted theses may be checked for plagiarism.	☒
5.	I/we am/are aware that the University of Agder will deal with all cases where there is suspicion of cheating according to the university's guidelines for dealing with cases of cheating.	☒
6.	I/we have incorporated the rules and guidelines in the use of sources and references on the library's web pages.	☒

Publishing Agreement

Authorization for electronic publishing of the thesis.

Author(s) have copyrights of the thesis. This means, among other things, the exclusive right to make the work available to the general public (Åndsverkloven. §2).

All theses that fulfill the criteria will be registered and published in Brage Aura and on UiA's web pages with author's approval.

Theses that are not public or are confidential will not be published.

I hereby give the University of Agder a free right to

make the task available for electronic publishing: ☒JA ☐NEI

Is the thesis confidential? ☐JA ☒NEI

(confidential agreement must be completed and signed by the Head of the Department)

- If yes:

Can the thesis be published when the confidentiality period is over? ☐JA ☐NEI

Is the task except for public disclosure? ☐JA ☐NEI

(contains confidential information. see Offl. §13/Fvl. §13)

Table of Contents

Abstract 1
Preface 2
Acknowledgement 2
Individual/group Mandatory Declaration 3
Publishing Agreement 4
Table of Contents 5
List of Figures 7
List of Tables 9
1 Introduction 10
1.1 Renewable energy (Developments & Current status) 10
1.1.1 Solar power 10
1.1.2 Wind power 10
1.1.3 Battery storage system 11
1.2 Microgrid 12
1.3 Problem description and research questions 13
2 Theory 14
2.1 Wind energy conversion system (WECS) 14
2.2 Wind energy system Micro-siting 15
2.3 Wind resource assessment in an urban environment 17
2.4 Photovoltaic system (PV) 18
2.5 Distributed Energy Resources 21
2.6 Battery energy storage system (BESS) 23
2.7 Inverter 24
2.8 Economics of a micro-grid system 25
2.8.1 Net Present Value 25
2.8.2 Levelized Cost of Energy 26
3 Literature review 27
3.1 Wind energy micro-siting and wake challenges 27
3.2 Microgrids 28
3.3 Hybrid microgrid design and optimization Techniques 31
3.4 Wind energy integration into a microgrid 32
3.5 Preliminary Study 34
4 Study case 36
4.1 Introduction 36
4.2 Terrain and roughness data 37

4.3 Wind data 37
4.4 Solar data 40
4.4.1 Location horizon and sun path 40
4.4.2 Gorines' installed solar panels 40
4.5 Battery 42
4.6 Load profile 42
4.7 Electricity data 43
5 Methods 44
5.1 Micro-siting using (WindSim) 44
5.1.1 Digital terrain module 44
5.1.2 Wind Field module 45
5.1.3 Objects module 46
5.1.4 Results module 46
5.1.5 Wind resources module 46
5.1.6 Energy module 47
5.2 Python 47
5.3 Techno-economic design and optimization (HOMER Pro) 47
5.4 Modelling and simulation methodology 48
6 Results and discussion 50
6.1 Wind energy system simulation 50
6.1.1 Layout setups 50
6.1.2 Simulation based on k-epsilon turbulence model 51
6.1.3 Simulation based on k-omega turbulence model 52
6.1.4 Techno-economic analysis 53
7 Conclusion 58
Reference 59
Appendices 66
Appendix A 66
Python code integrating the buildings 66
Appendix B 70
1. K-epsilon simulations results 70
1.1 Spot and residual values versus number of iterations 70
1.2 Wind speed (3D) and turbulent intensity maps 72
2. K-omega simulations results 75
2.1 Spot and residual values versus number of iterations 75
2.2 Wind speed (3D) and turbulent intensity maps 78

List of Figures

Figure 1. Trends in installed Solar power capacity (MW), source: IRENA statistics.....10
Figure 2. Solar generation cost in comparison with power, source: IRENA statistics.....10
Figure 3. Trends in installed wind power capacity MW, source: IRENA statistics. 11
Figure 4. Annual financial commitments in the wind power sector, source: IRENA statistics. 11
Figure 5. Stationary battery storage's energy capacity growth, 2017-2030, source: IRENA statistics..12
Figure 6. Wind turbine connection schematic[16].....15
Figure 7. Sketch of the urban boundary layer structure the mesoscale perspective [32].....18
Figure 8. Sketch of the urban boundary layer structure of the near-surface layer [32].....18
Figure 9. Grid-interfaced Solar PV system [36].....19
Figure 10. PV cell is modelled as a diode circuit [37]. 19
Figure 11. Solar cell I-V characteristic curve [16].....20
Figure 12. Distributed Energy Resources (DER) technologies, adapted from [14].....22
Figure 13. Centralized structure of a DC Microgrid [52]. 23
Figure 14. Previous research methodology flowchart.....34
Figure 15. Raw grid data (top) vs modified grid data (bottom).....35
Figure 16. Map of the south part of Norway, source: NVE Atlas. 36
Figure 17. Gorines location in the red polygon, source: Google maps. 36
Figure 18. Real-time monitoring for total energy production and consumption. 37
Figure 19. The average daily wind speed. 38
Figure 20. The average daily wind direction.....38
Figure 21. The site wind rose (speed vs direction). 38
Figure 22. Hourly wind direction versus wind speed.....39
Figure 23. The power curve of 600 kW wind turbine. 39
Figure 24. The power curve of 150 kW wind turbine. 39
Figure 25. Horizon and sun path diagram of company location (source: Global Solar Atlas).....40
Figure 26. Gorines' roof equipped with solar cells.....40
Figure 27. Simulated profile of solar energy production.....41
Figure 28. Gorines' solar power system production for 2021.....42
Figure 29. Daily profile of the electric load.....42
Figure 30. Hourly profile vs hourly price of the electric load.....43
Figure 31 Monthly profile of the electric load. 43
Figure 32. Hourly power prices in Dollars for 2021. 43
Figure 33. WindSim Software components. 44
Figure 34. Digital terrain model-Grid (xy) (left), Digital terrain model- Grid (z) (right). 45
Figure 35 HOMER diagram system [125].....48
Figure 36. Potential areas for the wind energy system.....50
Figure 37. Terrain data with integrated buildings.....51
Figure 38. K-epsilon spot (left) and residual values versus the number of iterations for sector 240°....51
Figure 39. Mean wind speed and power density at the hub height based on the k-epsilon. 52
Figure 40. K-omega spot (left) and residual values versus the number of iterations for sector 240°.....52
Figure 41. Mean wind speed and power density at the hub height based on the k-omega model.....53
Figure 42. The planned architecture of the grid-connected hybrid system.....53

Figure 43. system components` optimization analysis options. 54
Figure 44. Wind turbine monthly power production.....54
Figure 45. Canadian solar panels` monthly power production.....55
Figure 46. Jinko Eagle solar panels` monthly power production. 55
Figure 47. The total cost and revenue summary of the selected system components. 56
Figure 48. Monthly system components production and annual system production and consumption. 56
Figure 49.Hourly energy purchase and selling. 57

List of Tables

Table 1. Layouts' turbines specifications. 34
Table 2. Selected turbines` specifications.....39
Table 3.Solar poanels properties.....41
Table 4. Cost summary of the installed solar panels.....41
Table 5. The installed battery specifications. 42
Table 6. Simulations' general configurations.....49
Table 7. Wind turbine's energy estimation with the k-epsilon model.....52
Table 8. Wind turbine's energy estimation with the k-omega model. 53
Table 9. Wind turbine simulation results.....54
Table 10. PV simulation results.....55
Table 11.The cost summary of the selected system and its components.....55
Table 12. Annual production and consumption of the selected system. 56
Table 13. Monthly and annual energy purchasing from and selling to the grid. 56

1 Introduction

1.1 Renewable energy (Developments & Current status)

1.1.1 Solar power

During the 1950s and 1960s, solar cells provided electrical power to satellites. Through the 1970s, improved manufacturing techniques and lower prices can provide low-power electrical connections to remote terrestrial applications. Following the energy crises during the 1970s, many countries started developing photovoltaic (PV) power systems for commercial and residential use [1]. The demand for these products remained a significant portion of the global market for PV. In 2019, solar PV's global capacity reached 586 gigawatts, as shown in Figure 1, equivalent to nuclear and fossil fuel plants' total power generation capacity. It was also the most attractive power source for new installations.

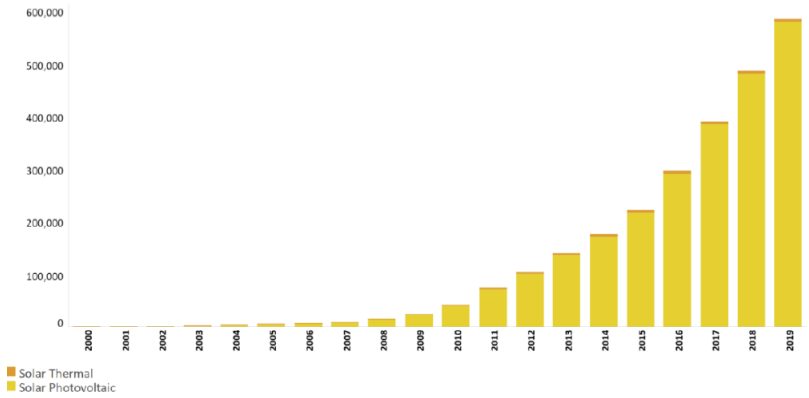

Figure 1. Trends in installed Solar power capacity (MW), source: IRENA statistics.

One of the main reasons solar's success has been due to its rapid cost reduction is because it has led to it becoming the cost leader in terms of electricity generation. This has led to solar becoming less costly than many other technologies, as shown in Figure 2.

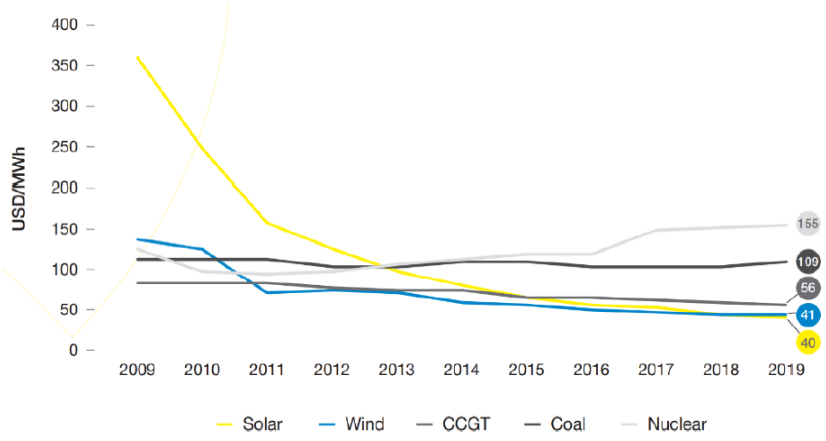

Figure 2. Solar generation cost in comparison with power, source: IRENA statistics.

Moreover, Solar PV has the most significant share of global renewable energy investments. From 2013 to 2018, it had a share of more than half of the total. The global PV expansion is expected to accelerate significantly after 2022, as various government policies and cost reductions help boost the adoption of distributed PV. This growth potential is estimated to reach 165 gigawatts by 2023-25 [2].

1.1.2 Wind power

The history of wind power can be traced back to the 19th century. It started to become widely used after the invention of the electric generator in the 1830s. In the UK and the US, wind power generation began in 1887 and 1888. In Denmark, the first horizontal-axis wind turbines were constructed in 1891 [3]. The

primary motivation for wind power research was to develop a way to make agriculture more self-sufficient. However, as the industrial world started to electrify, the role of wind power began to decrease.

Nevertheless, World War II and the lack of fossil fuels renewed interest in wind power during the First World War. However, the price of wind-powered electricity was still not competitive [4]. The rise of oil prices and the resulting supply problems during the 1970s put wind power back on the global agenda. This was because the Western part of the world was suddenly vulnerable to energy shortages. Although the financial and technical conditions for large-scale wind power production were still not clear during that period, many countries continued to explore the potential of this resource.

After the oil crisis, many companies and research institutions were funded by governments. Some had short-lived and failed, while others saw a potentially bright future [5]. Due to wind power's continuous development and increasing popularity, its costs are now significantly lower. This technology is also becoming more prevalent in various countries.

According to the latest data released by IRENA, the total installed capacity of wind power has increased by about 75% in the past two decades, as seen in Figure 3. Wind energy has become an integral part of the energy mix in many regions worldwide. In 2016, wind energy contributed 6% of the electricity produced by renewable sources [6].

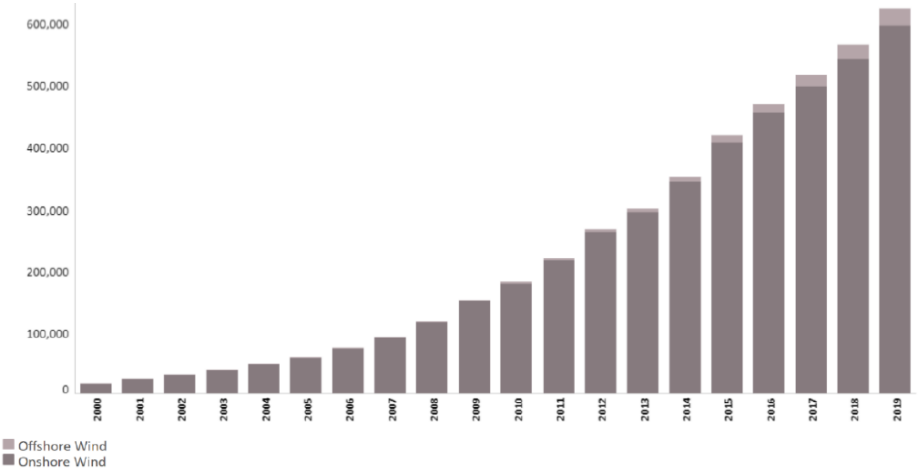

Figure 3. Trends in installed wind power capacity MW, source: IRENA statistics.

Today's wind turbines have a capacity equivalent to about 2 MW on an onshore platform and up to 5 MW offshore. In 1985, the average rated capacity of a wind turbine was 0.05 MW. In 2013, onshore wind energy became the leading source of renewable energy investments globally, as shown in Figure 4. This trend continued to grow in 2018, with offshore wind projects becoming more attractive [7].

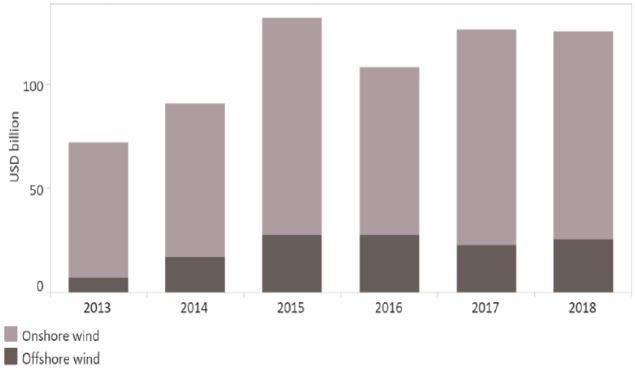

Figure 4. Annual financial commitments in the wind power sector, source: IRENA statistics.

1.1.3 Battery storage system

The Battery Storage Plant has gained widespread acceptance due to its ability to store and use electricity. Its stored energy can be used immediately, allowing immediate access to real-time power. Battery storage plants are designed to improve the reliability and security of the electricity supply. The first

commercial project to use this strategy was the Bewag plant in 1987. It can also help monitor and control the electricity supply in West Berlin [8]. Afterwards, battery storage systems are becoming more prevalent in the power industry as they help integrate renewable energy sources such as wind and solar. A recent analysis by the International Renewable Energy Agency (IRENA) highlighted how they could be used in various applications [9]. Battery storage systems can help boost the amount of electricity that flows to the grid when combined with renewable generators. They can also provide cheaper and more reliable electricity to rural communities.

Utilities-scale battery storage systems are currently being used in various countries, such as Australia, Japan, the UK, and the US. One of the most powerful systems in terms of capacity is Tesla's 100 MW Hornsdale Wind Farm battery storage project. In addition, off-grid communities and island-grids are investing in large-scale battery storage projects to improve the reliability of their electricity supply and manage the excess production of solar energy

In emerging markets, the deployment of energy storage is expected to increase significantly over the next couple of years, as seen in Figure 5. Behind-the-meter batteries are connected to the utility meter to provide electricity savings to customers. The increasing popularity of electric vehicles and smart grids has led to the rise of BTM batteries globally. In Germany, for instance, 40% of the recent solar PV installations were made with BTM batteries. Australia aims to reach 1 million BTM battery installations by 2025. In stationary applications, its total battery capacity could grow from 11 to 420 gigawatt-hours (GWh).

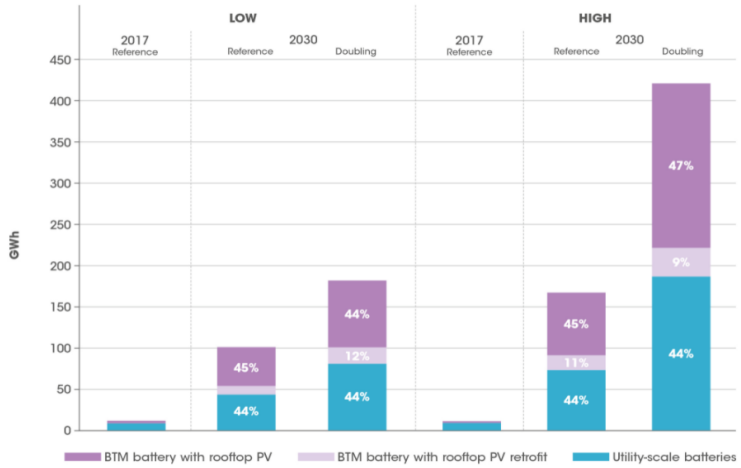

Figure 5. Stationary battery storage's energy capacity growth, 2017-2030, source: IRENA statistics.

1.2 Microgrid

The microgrid is a distributed energy system that combines different energy sources into one. It can operate seamlessly even when connected to the utility grid. The concept of microgrids was first introduced in the 1990s by the consortium for electric reliability technology solutions. They have since enhanced the system's flexibility. Thomas Edison established the first public power station in London in 1882. He proposed using D.C. generators to provide electrical power to the locals. Like Edison's system, microgrids are decentralized and can be generated locally. They can also integrate grid connections when necessary.[10]. The excessive centralization of networks has led to various problems, such as increased congestion and threats from non-biodegradable fuels. The increasing popularity of renewable energy has led to the development of distributed generation. A distributed generation facility (D.G.) is a power plant that uses a small number of electricity generators, which can be placed anywhere that is connected or not to the utility grid. This allows the distributed generation of green energy to be utilized. Since they can be easily controlled, microgrids are usually less costly than traditional energy generators.

Various technologies can be used for (D.G.) such as gas turbines, internal combustion engines and renewable energy. Concerning renewable energy, D.G. systems implement different sources such as wind turbines, photovoltaics, and fuel cells, generating a DC or AC voltage using the distribution system. They have numerous advantages, such as lower maintenance costs and high flexibility.

However, traditional generators can also be used as backup sources, defined as a hybrid solution. Hybrid solutions are composed of multiple renewable energy sources and traditional electricity generation, which overcome the intermittent nature of wind and solar energy. Moreover, these solutions. Hybrid energy systems are becoming more prevalent due to the increasing energy demands that can be connected to the main grid (on-grid) or isolated (off-grid), and they are commonly used to provide electricity in rural and urban areas. Unfortunately, the complexity of these systems makes it challenging to identify the most advantageous use of these resources [11]. Therefore, the optimal utilization of different electricity sources is an essential aspect of any microgrid project, which is done by identifying the most cost-effective and energy-efficient options. Because of the complexity of the issue and the varying characteristics of renewable energy sources, techniques and tools related to microgrids have become the sought-after topics in recent years.

Hybrid energy systems have various advantages over traditional sources-based methods. These include higher reliability, better efficiency, and reduced energy storage capacity when optimum design technique is used. However, hybrid energy systems are oversized or not adequately planned in most cases, resulting in high installation costs. A hybrid system's technical and economic analysis is essential for efficient utilization. This process can be done by using various software tools and models that can help design, analyze, and plan hybrid energy systems. The Hybrid Optimization Model (HOMER) is widely used as a software tool for assessing and planning electric renewable energy systems. It can be utilized for carrying out quick and accurate calculations.

1.3 Problem description and research questions

The development of wind energy systems in urban environments, characterized by high turbulence conditions, requires an in-depth understanding of the induced turbulence within the studied site. This requires utilizing several turbulence models to simulate urban site wind flow fields. This work conducts a feasibility study for an urban site clarifying the wind conditions by micro-siting a wind energy system while simulating the wind flow and estimating the potential annual energy production (AEP) for an industrial site (Kjerlingland) in Lillesand municipality. This work integrates the surrounding buildings (obstacles) within the studied domain and utilizes several turbulence models in order to simulate the wind flow and estimate the annual energy production of the proposed wind energy system. In addition, a techno-economic feasibility study is conducted to outline the economic needed and the profits that can be gained throughout the project's lifetime. Generally, the study has the following objectives:

- To design and micro-siting a prospective wind energy system in an industrial environment with buildings.
- To estimate the annual energy production from the system under varying wind conditions.
- To optimally integrate the wind energy system with an existing microgrid with solar PV with battery storage solutions.

Specific Research Questions of the study are:

- How can a wind energy system be optimally sited in an urban industrial environment and its performance be estimated under the complex flow conditions over the buildings?
- How can the above system be optimally integrated with an existing microgrid with solar PV systems and battery-based storage solutions?
- What are the economics involved in such a hybrid system, and would it be feasible for such a facility?

2 Theory

2.1 Wind energy conversion system (WECS)

A wind turbine is a type of electrical equipment that converts the power from the wind into electricity. It uses the kinetic energy of the air to generate electricity. In general, it can operate at a speed of 4 to 25 [m/s] [12]. Wind turbines are used in various applications. The more significant variants are commonly used in utility-scale applications, while the smaller ones are used in commercial and residential setups. A typical wind turbine consists of the following components:

- Blades
- Nacells
- Tower(stell /concrete)
- electrical installation and grid connection
- foundation(with basket/with section/for concrete tower)

The aerodynamic force of lift is used in wind turbines to generate a net positive torque, which translates into mechanical power. The output of a wind turbine is continuously variable, which makes it non-dispatchable. This means that it can immediately respond to wind conditions [13]. Different factors such as wind resource, reliability, maintenance, and spare parts availability can affect the selection of a wind turbine for a specific application. The size of wind turbines has grown remarkably during the last couple of decades. For instance, the largest units now have a maximum size of 14 MW compared to the 1970s, when unit sizes were below 20 kW. The increasing size of wind turbines has necessitated variable speed systems to overcome mechanical stresses [14]. Single units can be integrated into the grid with a 10–20 kV connection. However, the main challenge is transporting components of wind turbines in rural areas. These high-quality machines have blades with long sections, which cannot be transported using standard transportation.

The conversion of wind energy into electrical energy occurs in two stages. The first stage involves converting the kinetic energy of wind into mechanical energy, and it is used to drive a wind generator's shaft. The power coefficient *Cp* measures the efficiency of the first stage of wind energy conversion. It shows how much power is captured by the blades [15]. The power coefficient of the rotor is defined as the ratio of actual power developed by the rotor to the theoretical power available in the wind

$$Cp = \frac{Pmech}{Pwind} \tag{1}$$

The second stage involves converting the mechanical energy of wind turbines into electrical energy. Various parameters carry out this process, such as gearbox efficiency η_{gear}, generator efficiency η_{gene} and electrical efficiency $\eta_{elec.}$. so, the total power conversion efficiency of wind to electricity η_t, is given by these parameters.

$$\eta t = \eta mech * \eta gene * \eta elec \tag{2}$$

The wind power reaching the turbine blades is proportionate to the cube of the wind speed and can be described as:

$$Pwind = \frac{1}{2} * \rho * A * u^3 \tag{3}$$

Where: ρ is the air density [kg/m^3], A is the area swept by the blades [m^2], u^3 is the wind velocity [m/s]

Therefore, the effective power output of the wind turbine is

$$Peffc = \eta t * Pwind \tag{4}$$

The wind turbine power curve is a relationship between the wind speed and the wind turbine's power. It shows the turbine's performance and helps in controlling it. The manufacturers use the power curve of a wind turbine to estimate the potential of a site. It can also help in planning and expanding a wind farm. The power curve of a wind turbine is computed using the equation above. It gives the turbine's power

output as a function of the wind speed. The turbines generally start producing usable power at a low wind speed, referred to as the cut-in wind speed, around 4 [m/s]. This power output increases continuously and reaches the rated power. The output power of a wind turbine is measured by the wind speed at which it is powered. The higher the wind speed, the greater the output power. If the wind speed gets too large, the wind turbine should be shut down immediately to prevent damage, described as the cut-off wind speed.

Moreover, the wind turbine generation unit can use various generators, such as permanent magnet synchronous or induction generators. It can also be equipped with a dual-fed induction generator. A pulse width modulation converter is commonly used to control a generator's rotational speed. The power from generators is transported to the grid through a pair of components known as a generator-side converter and a grid-side inverter [16]. The power quality of a wind turbine depends on its system design. It can be affected by the availability of fuel and the effects of a direct connection to a synchronous generator. Direct connection to a synchronous generator can increase the frequency of flickers and generate significant active power variations [14]. Figure 6 shows the interconnection of the wind energy conversion system (WECS).

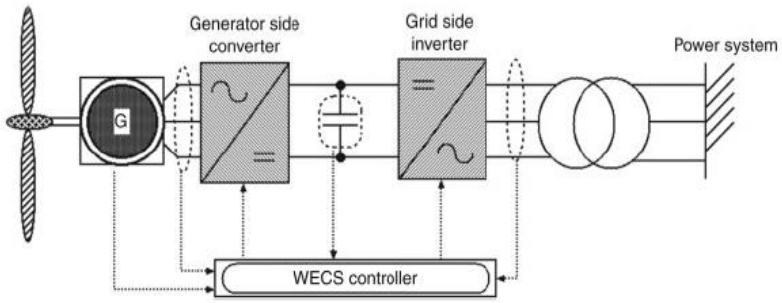

Figure 6. Wind turbine connection schematic[16].

It is no secret that wind turbines are expensive. For commercial projects, the cost of a single turbine can reach a million dollars per MW installed capacity. The cost of installing a wind turbine is typically a lot, and it takes a long time for the investment to pay off. Once the turbine is operational, it generates significant amounts of electricity and sells it back to the power grid. According to the analysis of the various markets, there are varying prices for wind turbines. The wide variation in the costs can be attributed to multiple factors such as the level of competition in a given market, the country's support policies for wind, and the presence of local low-cost manufacturers [17]. The cost depends on several factors, such as the size of the turbine, the location of the facility, and the various equipment and services required to operate it, the cost of cables, and the transportation of the turbine.

In addition, the operation and maintenance costs (O&M) of a wind turbine are typically a portion of the total annual costs of the system. These costs may count for around 25% of the levelised cost per kilowatt for a new model. If the wind turbine is new, the share of O&M costs may only be about 10%, but this could increase to around 35% by the end of the model's lifetime. As a result, manufacturers are developing new designs to reduce service visits and downtime. These cost components are typically categorized into three main categories: insurance, regular maintenance, and repairs. Some of these cost components are relatively easy to estimate. Aside from insurance, it is also possible to secure standard contracts for regular maintenance and repairs of a wind turbine. However, these costs are usually more difficult to predict. Although the cost of repairs and replacement parts for a wind turbine generally increases as it gets old, this factor is typically driven by its age. Only a few wind turbines have reached their expected lifespan of 20 years. These are significantly smaller than the ones currently available on the market. Their estimated costs are unpredictable since these turbines are relatively new [18].

2.2 Wind energy system Micro-siting

In the wind energy system planning phase, micro siting refers to the optimal placement and arrangement of individual turbines in the terrain. Different methods have been proposed to tackle this problem with linear and non-linear optimization techniques. The use of Generic Algorithms (GAs) prevails with the

more recent implementation of meta-heuristic algorithms and applications of realistic models of integrated economic behaviour of the wind energy system. The whole process is a challenging subject involving fluid dynamics and decision making and could play a crucial role in local wind energy planning [19]. Nevertheless, the methods used so far concentrate on optimizing several relatively restricted parameters related to minimizing initial investment and maximizing total electricity

production and overall life-cycle cost. For the purpose of achieving this, particular criteria used for positioning individual wind turbines in predefined sites are:

- Minimization of distance to access roads
- Minimization of the wake effect
- Minimization of Electrical infrastructure total land requirements and land cost
- Maximization of operational safety and the minimization of the topographic effect

Although these criteria provide limited consideration to social and environmental issues, they may also exist as elements that can be involved in the optimal micro-design for wind farms. Such critical factors can be the visual impact, noise propagation, bird disturbance, biodiversity loss, and impact on wildlife and habitats. These factors can be considered during the micro-siting of wind farms. In this way, it would be possible to evaluate and decrease the particular local influence of the wind project on the environment [20]. The initial step in wind energy system micro-siting is evaluating the wind resource of the studied site. Once the wind resource for a specific site is established, the configuration of the wind energy system can be designed to select the optimal location for wind turbines. In the case of onshore wind farms, the overall trend is to install the wind turbines in positions where the wind is the highest whilst observing a given distance between the turbines in the general wind direction in order to limit any unnecessary wake effect (where a wind turbine extract the kinetic energy of the wind that goes through its rotor, while creating a turbulent flow, and slower downstream)[21]. Moreover, other issues could be considered, such as the land requirement for the wind energy system, considering the infrastructure and land availability needed [22].

However, accurately quantifying power losses due to wind turbine wakes in various wind climates and wind farm layouts is crucial for optimal wind farm design. Several approaches exist to model wind turbine wakes, namely, analytical and numerical models [23]. Analytical wake models practice self-similar velocity shortage profiles received from experimental and theoretical work on co-flowing jets. Despite the benefit of being simple and computationally efficient, their forecasts cannot consider all the complex fluid mechanics that occur in wind farms. In contrast, Numerical models rely on Computational Fluid Dynamics (CFD) and give higher accuracy and adaptability to consider different ambient conditions and terrain features. Recent research has clearly focused on using CFD models for the optimal design of wind farms. An essential part of CFD models uses extensive laminate eddy simulations (LES) to determine the flow field. Although LES models have a significant level of accuracy when simulating turbulent flows, their use is still restricted by the extensive computational resources they need to solve the flow equations. Most CFD models are instead based on Reynolds-averaged Navier-Stokes (RANS) equations to solve the flow field.

The utilisation of this time-averaging procedure decreases the computational cost of the simulations but creates the need for additional turbulence models to close the system of equations [24]. Most studies have concentrated on optimizing layouts on flat and uniform topography[25] [26]. However, wind flow over complex terrains is more complex than flat ones since complex flow structures can work as wind flows over various land features. Consequently, turbine power production is strongly affected by local topography. Moreover, the lack of analytical closed-form mathematical models for wakes over complex terrains makes it challenging to estimate and optimize wind farm layouts. As a result, decreasing the computational cost of wake evaluations while maintaining high accuracy during optimization remains a challenge [26]. The CFD simulation model creates a flow field over the complex terrain without turbines using CFD. The initial wake effects can be determined by superimposing a flat terrain wake onto the complex terrain. This initial problem is then solved to determine where the turbines should be installed.

Nevertheless, due to errors in the initial wake estimate, placing turbines at these locations may not provide the optimal layout. Hence CFD simulations are managed at these locations to develop the accuracy of the initially estimated wake effects. This method is repeated until no new developing turbine

locations are found [27]. In different words, the wake effects defined in the optimization model convert more accurate with each iteration. Hence, the optimal solution of the current iteration is more accurate than those observed in previous iterations. If the problem cannot be solved optimally due to run-time limits, matching the near-optimal solutions from previous iterations becomes essential. Moreover, other optimization techniques such as metaheuristics also fit with this algorithm; however, without proof of optimal solution, the finish criteria for the optimization problem would need to be defined appropriately [28].

2.3 Wind resource assessment in an urban environment

Wind resource assessment evaluates potential wind flow for a particular site, which plays a vital role in a wind energy project. A comprehensive wind resource assessment usually entails the following tasks:

- Site prospecting: description of a correct site using cartography (e.g., wind maps, political maps.
- Measurement operations: characterise the on-site wind resource by reading the winds for 1 to 4 years as close to hub height, with temporary meteorological masts (possibly completed or supplemented with remote sensing instruments).
- Microscale vertical extrapolation: change of the measurements to hub heights.
- Long-term extrapolation: distance measurements to the 10 to 30-year-long development lifetime using historical observations (e.g., nearby tall towers, surface weather stations, and modelled data sets such as reanalysis and often statistical methods [29].
- Wind farm layout design: establishing turbine locations related to wind resource estimation (e.g., using standard wake models or computational fluid dynamic models).
- Gross energy production estimate: estimate the possible wind energy production over a year (or over the lifetime) for the whole site.
- Energy losses assessment: evaluation of losses due to different reasons equipment downtime, array losses and others [30].

In urban environments, city blocks create complex and turbulent wind fields due to the significant spatial heterogeneity of urban morphology. The mean flow profiles, unsteadiness of the flow, and turbulence characteristics in urban environments have been studied in many wind tunnel experiments, numerical simulations, and full-scale measurements [31]. The research explains that the urban boundary layer (UBL) can be artificially divided into several sub-layers, as seen in Figure 7. From the top of the UBL is the mixing layer (ML). The surface roughness does not directly influence the turbulence characteristics in ML, but the convective air motions create turbulence (e.g. Rayleigh–Taylor instability). Below the ML layer is the near-surface layer (NSL), divided into three sub-layers, as shown in Figure 8, each with different flow and turbulence characteristics. The inertial sub-layer (ISL) is at the top of NSL, which can be called the constant–flux layer alternatively. The lower base of this layer is at about 10% of the height of the UBL, which is called the urban canopy layer where the city blocks are located. The complex structure of UBL makes the wind resource assessment in urban environments very challenging. The most straightforward way to estimate the wind potential in cities is to perform the long-term (several years long) measurement operations at the proposed wind turbine(s) installation location. The obvious disadvantages of this method are related to the complexity and the length of such campaigns. A popular choice in the industry is to use commercial wind resource assessment tools (wind modelling, RETScreen, AWS Truepower). Nevertheless, most of this software is developed and designed for wind resource assessment in rural areas with smooth to moderate surface complexity. Due to the non-linearity of the flows in cities, these methodologies are not suitable for urban wind resource assessment [32]

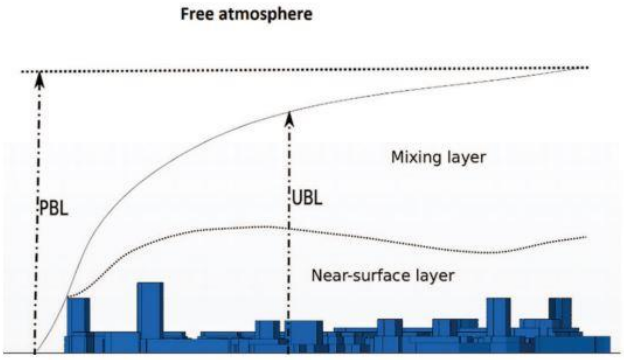

Figure 7. Sketch of the urban boundary layer structure the mesoscale perspective [32].

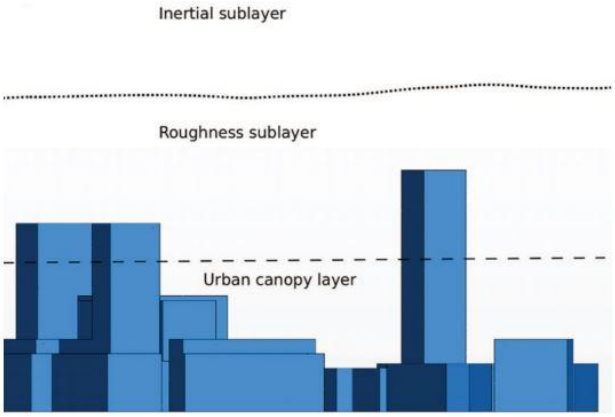

Figure 8. Sketch of the urban boundary layer structure of the near-surface layer [32].

2.4 Photovoltaic system (PV)

The solar photovoltaic system is a device that uses sunlight to convert it into electricity, which helps reduce greenhouse gas emissions and provides sustainable electricity. The main component of this technology is the purity of the silicon used in the production of the cells. This ensures that the cells are as efficient as possible. The most commonly used materials for solar energy conversion are poly-crystalline silicon, thin-film, and mono-crystalline silicon. However, the performances of these modules vary by region. The power output of a typical solar cell is about 1 W. This means many cells are connected to a single module in series and parallel [33]. The power output of a solar panel is proportional to its surface area and footprint size. This technology could be standalone or connected to the grid. Since the size of the solar panel is a critical factor, it should be relatively large to achieve a high power output [14]. When a PV panel is connected to an array, the electricity produced by the system is constant. A critical controller is a solar radiation that regulates the DC voltage. An inverter then manages the DC voltage. Although the existing standards are adequate, more studies are needed to investigate the effect of multiple inverters on the system [14]. The varying weather conditions that affect electricity production from a PV array can affect the system's output voltage. This is why it is essential to control the output voltage using a technique known as maximum power point tracking[34]

A PV module's maximum power output is usually obtained near its knee due to its characteristics. Since the temperature and solar radiation affect the output current of a PV, a maximum power point tracking stage is required in a conversion device to ensure that the system gets the maximum output [35]. The DC-DC converter is a vital component of the grid-tie PV system. It is commonly used for converting DC to AC. Nevertheless, there are four types of DC-DC converter, buck converter, boost converter, buck-boost converter and Cuk converter. Buck-boost, Cuk, and conventional boost are commonly used for solar applications [36]. Figure 9 shows a block diagram of the complete architecture of the grid-tie PV system

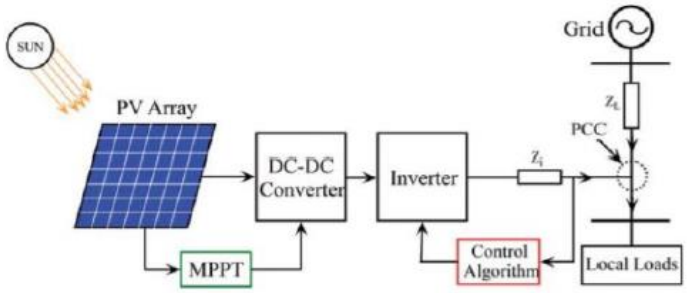

Figure 9. Grid-interfaced Solar PV system [36].

The complex physics of a solar cell can be represented by the electrical circuit shown in Figure 10. The following equation describes the corresponding I-V characteristic

$$I = Iph - I0[\exp\left(\frac{V + IRs}{\frac{KbT}{q}}\right) - \frac{V + IRs}{Rsh}] \quad (5)$$

Where *Iph* is the photo-current, and it is related to the photon flux incident on the cell end dependent on the wavelength of the light, *I0* is the diode saturation current [A], *Kb* is the Boltzmann constant (1.38 $*10^{-23}m^{-2}kgs^{-2}k^{-1}$), *Rs* is the series resistance. It represents the internal resistance to the current flow and depends on the n-p junction depth, *T* is the absolute temperature [K], *I* is the load current [A], *V* is the voltage at the terminals of the cell [V], *Rsh* is the shunt resistance, and it is inversely related to the leakage current to the ground and *q* is the electronics charge [C].

The power curve and the I-V characteristics of a solar cell are represented by the open-circuit voltage and the short circuit current. The short circuit current is the most significant current generated by the cell when the cell output is short-circuited.

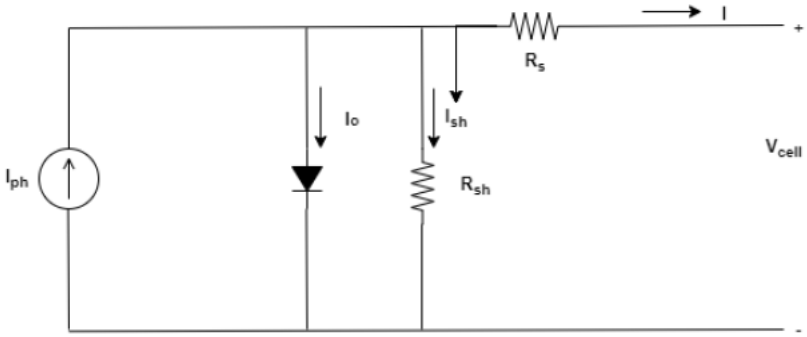

Figure 10. PV cell is modelled as a diode circuit [37].

The power output of a cell is the sum of its output voltage and current. Figure 11 shows the cell's zero current output. The maximum power point is when the cell can generate its maximum output power. The voltage and current parameters of a solar cell are represented by their respective numbers in the manufacturer's datasheet as Vmpp and Impp. Since the ground leakage current and the small diode can be ignored in the circuit, the short circuit current is equal to the photogenerated current. The open-circuit voltage is described as:

$$Voc = \frac{Kb\ T}{q} * In(1 + \frac{Iph}{I0}) \quad (6)$$

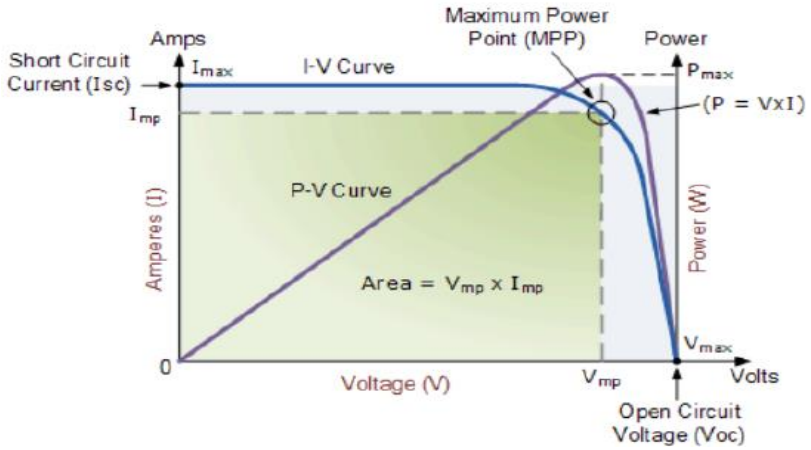

Figure 11. Solar cell I-V characteristic curve [16].

The temperature of individual cells within a PV module is known as *Tc*. It is the proper temperature to predict the module's electrical performance. Although it is generally higher than the back-side temperature *Tb*, the difference can be attributed to various factors such as the materials used and the solar radiation flux. The simple linear expression can describe the relationship between the two temperatures:

$$T_C = T_b + \frac{G_T}{G_{ref}} * \Delta T_{Gref} \tag{7}$$

In which G_{ref} is a reference solar radiation flux incident on the module [1000 W/m^2], and ΔT_{Gref} is the temperature difference between the PV cells and the module backside at this reference solar radiation flux, *GT* is the solar radiation striking the PV array [kW/m^2] [38].

An established procedure for formulating *Tc* using the energy balance of a cell/module involves using the nominal operating cell temperature *NOCT*, described as the temperature of a device at the requirements of the nominal terrestrial environment (*NTE*): Solar irradiance 800 [W/m^2], ambient temperature 20 [°C], average wind speed 1 m/s, zero electrical loads, and free-standing mounting frame oriented [39, 40].

$$NOCT = (T_C - T_a)_{NTE} + 20(C^\circ) \tag{8}$$

The temperature difference (T_C - T_A) between the sides of a module can be computed by observing that the temperature difference is proportional to the solar radiation flux [41]. In addition, it causes the approximation that the general thermal loss coefficient, UL, is constant to be obtained by the NOCT test [42]. Since the factors such as wind speed, humidity, and temperature, can affect the operating temperature of a module, this method excludes them from calculating the thermal loss coefficient [43].

If the steady-state energy balance, namely [PV electrical power]=[absorbed solar power]–[dissipated power], is written for a unit module area, i.e.:

$$\eta_c G_T = (\alpha\tau) G_T - U_L (T_c - T_a) \tag{9}$$

Where, τ is the solar transmittance of the cover of the PV array [%], α is the solar absorptance of the PV array [%], G_T is the solar radiation striking the PV array [kW/m^2], η_c is the electrical conversion efficiency of the PV array [%], U_L is the coefficient of heat transfer to the surroundings [kW/m2C°], T_c is the PV cell temperature [C°], and T_a is the PV cell temperature [C°].

A simple rearrangement leads to the following expression for the operating temperature [43]

$$T_c = T_a + (\alpha\tau)\left(\frac{G_T}{U_L}\right)\left[1 - \frac{\eta_c}{(\tau\alpha)}\right] \tag{10}$$

This last equation can be applied to *NOCT* conditions (i.e. for η_c=0) and solved for the assumed constant U_L, which is found to be

$$U_L = \frac{(\alpha\tau)G_{NOCT}}{T_{NOCT} - T_{a,NOCT}} \tag{11}$$

Substitution of this last expression back into Eq.(10) then leads to the equation

$$T_c = T_a + \left(\frac{G_T}{G_{NOCT}}\right)\left(T_{NOCT} - T_{a,NOCT}\right)[1 - \frac{\eta_c}{(\tau\alpha)}] \tag{12}$$

For simplicity, we have written G_{NOCT} and T_{NOCT} instead of $G_{T,NOCT}$ and $T_{c,NOCT}$, respectively. However, the constant *UL* approximation is not necessary, as it does not lead to a substantial simplification. Thus, if the energy balance equation (9) is written for *NOCT* conditions (i.e. with $\eta c=0$) and the resulting equation is combined with Eq. (9), an expression for *T*c similar to Eq.(12) can be easily obtained in the form:

$$T_c = T_a \ + (\frac{G_T}{G_{NOCT}})(\frac{U_{L,NOCT}}{U_L})(T_{NOCT} - T_{a,NOCT})[1 - \frac{\eta_c}{(\alpha\tau)}] \tag{13}$$

Eq. (13) is an implicit equation that can be used to determine the operating temperature of a solar cell or module. It can be used in situations where the modules are mounted free-standing. However, it should not be used for applications where the modules are subjected to different environmental conditions. For instance, in Building-integrated photovoltaics(BIPV) systems, the modules are mounted in other locations and have different environmental conditions [44].

Moreover, the power rating of a solar panel tells how much electricity it can produce. It measures how much power a panel can provide when operating in its ideal conditions. The amount of electricity that a solar panel can produce depends on its efficiency, type, and working conditions. From [45] [46] [47], the energy generation cost of a PV system has been calculated. The following shows the energy generated from the system and its use. The energy generation cost of a PV system has also been linked to the system's modules and inverter, and the system's battery is an independent energy source. The equation has defined the PV system generation cost (E_{PV})

$$E_{PV} = \frac{NCF_{SYS} * CRF_{PV}}{\sum_{m=1}^{12} N_D * M_{PV}} \tag{14}$$

Where N_D is the number of days in a month, M_{PV} is a monthly average generated by a PV system, NCF_{sys} is the total net present cost of a PV system, which is the sum of the investment cost of PV (C_{PV}), operation and maintenance cost (OM_{sys}) and replacement (R_{INV}) of system inverter, and CRF_{PV} is the capital recovery factor, which is given by:

$$CRF_{PV} = (\frac{b}{1 - (1 + b)^{-M}}) \tag{15}$$

Where: *b* is the discount rate, and *M* is the project lifetime

2.5 Distributed Energy Resources

The development of renewable energy sources has opened up the possibility of electricity transmission to remote and industrial communities. There are many communities in developing countries that do not have electricity. Many rural communities in developing nations lack electricity due to the high cost of implementing transmission and distribution infrastructure. In some cases, individuals rely on diesel generators to provide their electricity. Since the cost of extending the national grid is very high, it is not feasible for utility companies to provide electricity to remote villages, industrial and remote island areas. Instead of paying for the additional expenses of extending the national grid, solar and wind energy systems are becoming more cost-effective solutions for providing electricity to these areas. Modern renewable energy systems include wind turbines, photo-voltage systems, and battery storage [48]. They can be commonly installed in almost any location since sunlight is widely available in most areas. However, the other technologies can only be utilized in places where the resources are sufficiently available. For example, bioenergy and mini-hydro plants require different types of water and biomass to operate successfully. A suitable system should also take into account the geographical location.

Although the cost of solar and wind energy systems is still relatively high compared to fossil fuel-based electricity, they provide more reliable power. Unfortunately, renewable energy sources are intermittent and are prone to fluctuate, which means that they are unreliable and can be prone to failure.

Interestingly, using multiple renewable energy resources provides more reliable electricity than a single renewable energy source has been recognized as one solution to these problems. A conventional energy source is often combined with a renewable energy source to provide a more cost-effective and reliable energy system. A renewable energy hybrid system combines a traditional energy source and a renewable energy source. The grid formed by this system, known as a microgrid, is a type of hybrid system that uses a combination of solar and wind energy sources. It uses a diesel generator and a wind turbine to provide backup energy. In addition, a battery bank is used as an energy storage medium [49].

To illustrate more, the distributed energy resource is a power source located at a customer's load side and provides electricity to the end-user. It can be used to meet the load requirements of a particular customer. It can be composed of both generation units such as a fuel cell, a micro-turbine, a solar panel, a wind turbine, [50] and energy storage technologies like batteries, flywheels, or superconducting magnetic energy storage [14]. Figure 12 illustrates the technologies that can support distributed energy resource systems.

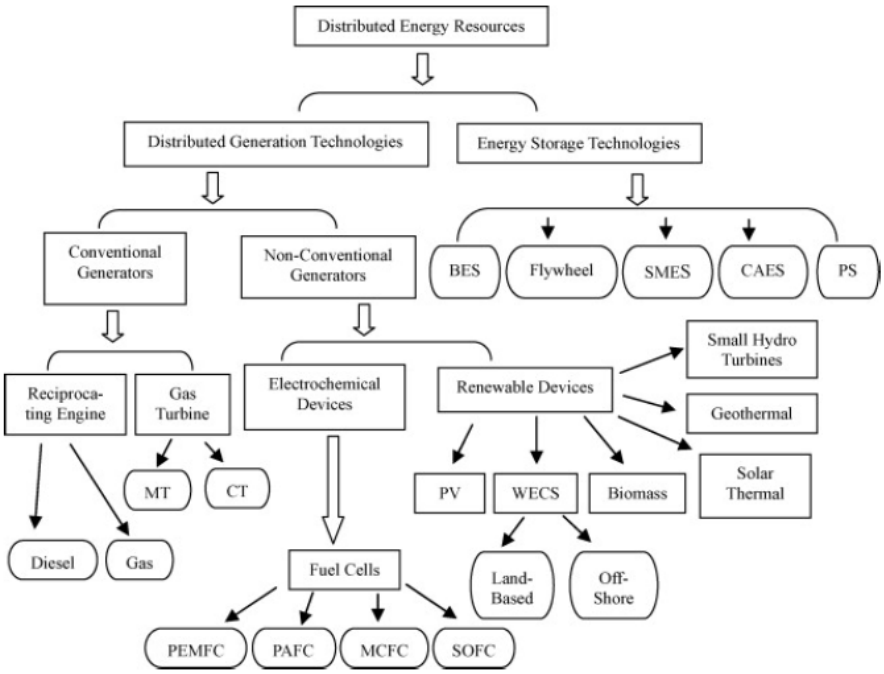

Figure 12. Distributed Energy Resources (DER) technologies, adapted from [14].

Moreover, DC microgrids mainly comprise renewable energy sources and energy storage systems, as shown in Figure 13. According to the type of bus that will link the different components together, hybrid systems can be classified as follows [51]:

- DC coupled Hybrid system
- DC/AC coupled hybrid system
- AC coupled hybrid system

A DC microgrid is very popular due to its simplicity and ability to integrate with different energy sources seamlessly, and it can also be built with a low voltage distribution network to minimize the losses incurred due to the frequent conversion of AC and DC power. Therefore, they offer better reliability and efficiency than AC microgrids [52]. However, DC-coupled topologies are commonly used in small systems. Usually, the generators are DC and are mainly used for the PV. DC coupled generators are usually connected to a battery and a charge regulator. AC consumers are typically connected to an inverter, whereas DC consumers are also related to the DC side. When systems size increases, they are usually converted to AC-coupled hybrid systems. This eliminates the need for DC coupling, and the

battery is equipped with additional power electronics. This system can be used with various equipment, simplifying adding new equipment. The Ac/dc system is a combination of two methods that can be achieved to extract the advantages of each other[53].

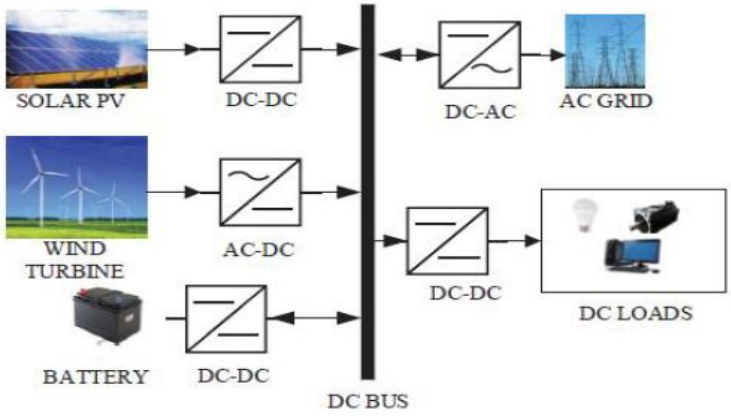

Figure 13. Centralized structure of a DC Microgrid [52].

2.6 Battery energy storage system (BESS)

Although solar, wind, and hydro can produce electricity, they are intermittent sources. In these cases, the power system must have some energy storage ability to overcome the fluctuations in the energy supply. In some cases, energy storage can provide a means to harness the excess energy produced by utilities. Energy storage is a process that converts electrical energy into another form of energy. There are various types of energy storage systems, such as batteries, flywheels, and pumped storage [54].

The primary function of battery energy storage systems is to provide spinning reserve if the power grid gets interrupted. For these systems, rechargeable batteries are utilised to store electricity in the form of chemical energy. The ideal battery for energy storage has high energy density, high power, long life, and low initial cost. The bulk of today's utility-scale battery storage systems comprises many lead-acid cells. Aside from energy storage, batteries are also used for various applications such as load levelling, frequency control, and voltage regulation. These batteries provide a quick response time and are ideal for applications that require proximity to load centres. They are also quiet and non-polluting. Lithium-ion batteries, nickel-metal hybride batteries, and lead-acid batteries have been used in various energy storage applications [14] [55].

These batteries comprise stacked cells arranged to convert chemical energy into electrical energy. The desired current and voltage are obtained by connecting the cells in parallel and series. There are two types of batteries, namely primary and secondary [17]. The primary batteries are used only once and can only be charged once, while the secondary batteries can charge multiple times. Renewable applications use secondary batteries. The voltage of a battery is also determined by its open circuit.

Current advancements in battery technology are still ongoing. Some of the commercially available batteries are still in the experimental stage. The most common type of battery used in power system applications is deep cycle batteries. These are similar to the ones used in electric vehicles. They have energy capacities ranging from 17 to 40 MWh and have efficiencies of around 70%. Lead-acid batteries are the oldest and most mature type of battery. They have been used for a majority of devices. Each lead-acid battery cell contains a negative electrode and a positive electrode, separated by a micro-porous material and immersed in an aqueous sulfuric acid electrolyte. However, the Li-ion, NaS and NiCd batteries represent the leading technologies, but Li-ion is considered the most promising type of battery for high-power-density applications. Li-ion batteries are ideal for portable devices due to their high energy density and low weight. Some of the disadvantages of Li-ion batteries are their high cost, complex circuitry, and the harmful effect deep discharging has on its lifetime [56].

The characteristics used to determine the cell's performance are also important when choosing the correct battery, such as discharge curves, cell chemistry, temperature characteristics, self-discharge characteristics, temperature effects, internal impedance, and discharge rates [8]. The state of charge is the percentage of the energy stored inside the battery. The load power and the renewable energy sources

that the battery uses are also affected by the battery. The state of charge can be calculated using the following equation.

$$SOC(t) = SOC(t-1) + \int_0^t \frac{I}{C_{bat}}.dt \quad (16)$$

Where *SOC(t)* is the battery state of charge [%] at time *t*, *SOC(t-1)* is the initial battery state of charge [%], *I* is the charge and discharge current [A], *t* is time [h], C_{bat} is the battery capacity [Ah]. The state of charge is the minimum charge that the battery must maintain to avoid permanent damage. The efficiency is the percentage of energy that can be withdrawn back out. The maximum discharge current is the amount of electricity that can be discharged from a battery at any one time.

The battery life is a measure of the performance and longevity of a battery. It can be calculated by estimating its run time on a full charge or by the number of charge cycles until the end of its useful life. The life of a battery is mainly affected by its operating temperature and the depth of discharge. The manufacturer usually provides a nominal number of charge and discharge cycles for its products. Lifetime throughput of the battery, which also depends on the number of cycles to failure can be calculated using the following equation.

$$Q_{lifetime,i} = f_i d_i (\frac{q_{max} * V_{nom}}{1000}) \quad (17)$$

Where $Q_{lifetime,i}$ is the lifetime throughput [kWh], f_i is the number of the cycle to failure, d_i is the depth of discharge [%], q_{max} is the maximum capacity of the battery [Ah], V_{nom} is the nominal voltage of the battery [V].

Various factors can affect a battery's overall lifespan and performance. For example, the ambient temperature is of the battery typically measured at around 25 degrees Celsius. This can affect its performance and lifespan. Battery chemistry can affect the longevity of electrical power. It is essential to regularly check and replace them if they are no longer working correctly. When a utility power failure occurs, a power supply system uses battery power to keep the equipment running. After the utility power is restored, the battery is recharged, and the system is fully operational, so The discharge and recharge cycles affect the battery's capacity. The length and quantity of these cycles determine the reduction in battery capacity [57].

2.7 Inverter

The increasing utilization of renewable energy sources and the local energy generation from distributed generation has resulted in many energy sources on the grid. Most micro-turbines, wind farms, and fuel cells generate electrical power as a direct current DC. They then convert it to an AC-based system using an inverter [58]. The wide range of applications that an inverter can support makes it an essential component of any grid power system. It converts the DC voltage to a sinusoidal current and interfaces between the local load and the grid. The different levels of electricity that it receives due to the different levels of generation by the local load and the grid voltages can be handled by an inverter [59]. The main component of smart grids built in the future is inverters. These devices control the frequency and voltage of the grid.

These devices are often paralleled to create power systems improving their performance. Compared to a single centralized source, the parallel operation of an inverter offers higher reliability. This advantage can be attributed to the fact that one of the generators can fail without disconnecting the whole system. This is also beneficial considering the growth of renewable energy sources such as photovoltaic and wind[60].

Various types of inverters can be categorized based on the waveform they produce. For instance, a square wave inverter is commonly used for small appliances. The output voltage control and limited surge capacity of an inverter are some of its disadvantages. It also has a high harmonic distortion rate. The presence of harmonic distortion distorts the current flowing from the supply. A modified sine wave inverter, on the other hand, can produce output with less distortion. Although a standard sine wave inverter is expensive, it has a wave shape close to the grid voltage [61].

The efficiency of an inverter is a critical component of its design. It measures the amount of current that can convert into alternating current without experiencing loss or damage. The size of an inverter depends on its potential to generate income or save energy. Different capacities are also considered when it comes to choosing a design. The input rating of an inverter should not be less than the total output of the connected appliances. The size of the inverter should be larger than the total number of devices. In the case of a motor or a compressor, the size should be three times the capacity of the appliances.

Generally, solar inverters are rated at around 93% to 96% efficiency. However, they can still lose some of their power due to the heat they generate. They can also be powered by standby power. The efficiency of an inverter is directly related to the total energy production of a power system. Although the efficiency of an inverter is a commonly stated number, it is not a fixed number. Instead, it has a curve that shows how its efficiency fluctuates depending on the input voltage and power supply. Various techniques improve solar inverters' efficiency, such as reducing the total harmonic distortion and controlling the output voltage, using an auxiliary inductor in a single-phase inverter to achieve zero-voltage switching, which can help improve the efficiency of the device. It is possible to protect an electronic device from inrush and overcurrent by adding a series of parallel clamps to its resonant capacitance [62].

2.8 Economics of a micro-grid system

The initial capital cost is the total amount of equipment and installation cost that a project will require at the beginning of its life cycle. In most cases, the cost of civil work and electric connections are the other components of the project's initial cost. The replacement cost refers to replacing a feature that has already completed its economic life cycle. It may differ from the initial capital cost for some reasons, such as Some components of hybrid systems may not require replacement after their life cycle. Subvention can help decrease the initial cost of the project. The operation and maintenance (O&M) cost is the total cost of maintaining and operating a facility for its life. It usually includes various components such as generators and equipment. The O&M cost for the national grid is the annual power purchase from the grid. It is divided into multiple costs, such as penalties and emissions. Other costs such as capacity shortages and penalties are also included in the O&M cost. The salvage value is the remaining portion of the energy system left after the project's lifetime [63].

2.8.1 Net Present Value

The net present value is the difference between the cash outflows and the cash inflows. The net current value is a critical component of a project's profitability. It is used in planning and investing. NPV is the result of calculations used to find today's value of a future stream of payments.

$$NPV = \sum_{t=1}^{n} \frac{R_t}{(1+i)^t} \tag{18}$$

Where R_t is net cash inflow-outflows during a single period of time, i is the discount rate or return that could be earned in alternative investments, and t is the number of timer periods.

The net present value can also compare the various investment options. It considers the time value of money and the discount rate applied to the capital required to invest. One of the main drawbacks of NPV analysis is that it assumes that future events are not reliable. The concept of an NPV is that it considers the profitability of an investment based on the assumption that the dollar in the future will not be worth the same as it is today. Unfortunately, due to inflation, money loses value over time. However, it can be invested and earn a return, making its future value higher than it is today. The NPV formula considers the expected future cash flows of an investment. It discounts these to the present-day value. If the initial cost is less than the sum of the future cash flows, then the investment is worthwhile. A positive NPV indicates that the expected earnings from a project or investment exceed the costs. A negative NPV is a negative indicator that suggests that the expected earnings from a project or investment are not enough to cover the costs.

2.8.2 Levelized Cost of Energy

The levelized cost of energy is a vital metric that will help determine if a project will be profitable or not. If the LCOE is unfavourable, the firm will not proceed with the project. This is one of the first steps a company takes to assess a project. Moreover, The LCOE is a valuable tool that enables financial analysts to evaluate the various energy-producing technologies. It allows for comparing different energy-producing technologies based on multiple factors such as the life span, capital costs, and the risk associated with each project. The LCOE is computed by considering the cost of electricity generated and the risk associated with each project. It also takes into account the discount rate that each power-generating asset uses. The Levelized cost of energy is a measure of the cost of electricity that is used to compare the various energy production methods.

An energy-generating asset's LCOE is the average cost of building and operating the facility over its lifetime. The levelized cost of energy can also be regarded as the minimum price that the electricity produced by an energy-generating facility must be sold to cover its operating costs. The LCOE is a measure of a project's net present value. It can be used to evaluate a project's chances of success. The LCOE is calculated by dividing the total cost of electricity production by the total electric load:

$$LCOE = \frac{C_{ann,tot} - c_{boiler} * H_{served}}{E_{served}} \quad (19)$$

Where $C_{ann.tot}$ is the total annualized cost of the system [$/yr], c_{boiler} is boiler marginal cost [$/kWh], H_{served} is the total thermal load served [kWh/yr], E_{served} is the total electrical load served [kWh/yr]

3 Literature review

3.1 Wind energy micro-siting and wake challenges

As discussed previously, the wind potential in urban areas is challenging to identify due to the significant influence of obstacles and structures on the atmospheric flow. Buildings often create flow separation, wind speed reduction and high turbulence on the top and around buildings [64]. However, various data sources may describe the wind flow in urban environments, such as databases are the national and regional wind potential atlas. These sources have different resolutions and generally apply data from either mesoscale models, e.g. Weather Research and Forecasting (WRF) or microscale models, e.g. Wind Atlas Analysis and Application Program (WASP). However, despite their validity, both types are not adapted well to urban environments, where the wind potential is often overestimated [65]. The performance of CFD models to characterize the wind behaviour around buildings is nowadays state of the art.

Nevertheless, applying these models is highly time-consuming, particularly when one needs to adequately model large areas to evaluate the impact of structures on the wind flow [66]. The complexity of the domain's geometry requires the use of powerful computers in order to get reliable results and reinforce the non-suitability of most CFD programs for the study of large areas. Usually, ultrasound and conventional anemometers are used to assess the wind in urban areas. Additionally, the scientific community has also used Light Detection And Ranging (LiDAR) measurement systems and statistical methods such as the Weibull distribution based on large wind databases for this purpose in the last decade [67].

Moreover, the urban digital terrain model UDTM is generally adapted when simulating urban conditions. UDTM is a methodology based on generating a digital terrain model that involves the terrain and the existing buildings. The urban DTM method can be managed as a very complex terrain and be utilized as input for a standard wind resource assessment model (e.g. Wasp, WindSim). This methodology dramatically reduces the computational costs compared with standard CFD models to simulate groups of buildings. It simplifies the urban mesh's geometry and permits the increase of the simulation area to a city scale. The use of the UDTM methodology showed to help identify the wind potential in urban areas, thus allowing the identification of suitable areas for the installation of small wind turbines [31]

A few studies have convoyed analysing wind turbulence characteristics within urban sites, e.g. at the rooftop of a building, considering the urban boundary layer (UBL). The authors in [68] evaluated the wind energy resource on the rooftop of a depot in an urban environment and assessed the sensitivity of wind resource distribution for different operating conditions, e.g. building height, roof shape, wind direction, turbine installation height, and turbine installation location, using CFD simulations and measurement methods. Furthermore, these studies concentrated on the wind turbulence characteristics and the wind accelerating influence over the building. The results were regularly confirmed using the conventional wind vane and wind tunnel tests. Similarly, the study in [66] suggests the optimum installation height for wind turbines in urban sites to be from 1.51 to 1.79 times the height of the building, and the most suitable locations are at the forefront where the wind acceleration gives the maximum, as the wind direction changes at the relatively low rise buildings in the medium urban environment. The wind energy distribution assessment over geometrical bodies has been considerably improved by applying the computational fluid dynamics technique. The Weibull distribution function and von Mises distribution functions are widely used to represent wind speed and direction.

Furthermore, The wind distribution over the building has been studied by many researchers, among the works of whom the most general and widely referenced data is attributed to Castro and Robins on the wind distribution around a cube. Their research provided the pressure distributions along various symmetry lines of the cube given for wind approach directions of 0° , 45° , and 90° . The CFD method is applied to the building model to estimate the roof-top acceleration of wind speed [69]. For the numerical study, the cube-shaped building model of 50 m (height) × 50 m (width) × 50 m (length) is used. The experiment was carried out in the wind tunnel on a scaled cube with the model dimension of 0.02 m and the Reynolds number of 100000 over the top surface of the cube. Their wind distribution

data is also widely used to validate computational fluid dynamic codes and turbulent models [70]. In a more extensive work, the Mongolia University of Technology, a case study in Hohhot [71] provided a range of work on urban wind energy utilization issues, for example, urban boundary layer and rooftop wind turbine utilization, turbulence design of building wind environment, and the impact of obstacles on turbulence.

Regarding various characteristics, the accuracy of various turbulence models in the numerical simulations was compared, the numerical study method selection of wind turbine micro siting was analyzed, and the specific installation height of wind turbines at diverse varieties of roofs was considered. Moreover, a new method for numerical research and study of rooftop wind turbine microsite selection based on the urban atmospheric boundary layer approach was suggested. The power of a particular rooftop wind turbine for buildings in the city was predicted [71]. Furthermore, the impact of non-architectural factors in the turbulent urban environment, such as the disturbance effect of different inflow angles, wind profile, surface roughness, and hedge wall, on the micro-site selection of the wind turbine. In this study, ZephIR Lidar was applied to observe the wind environment indicators10–19 m above the open area of an experimental base in the urban outskirts of Hohhot for one year. The Weibull distribution function was utilized to analyze its statistical characteristics. The results explained that the three-parameter Weibull probability distribution model has good applicability to the wind speed characteristics of urban-suburban buildings. The exponential form based on the natural logarithm can well fit the station's changes in wind speed and TI. 12–19 m is an almost constant wind-shear height zone within the observed height range. From the view of the sample source of wind data and the characteristics of its Weibull distribution, taking the dispersed and growing wind energy in cities by fitting parameters of each month alone is helpful. The system, shape, and position parameters generally change linearly within the height of 10–19 m. The wind speed probability distribution at 38 m, in the range of 0–2 m/s, is significantly lower than the probability value of the actual distribution at this position. Therefore, the wind speed region within 0–2 m/s is underestimated. However, the limitations of urban observation conditions can still be solved on the whole [71].

Regarding the wake problems, some studies [23] [72] show that wind energy system configurations are not significantly optimal for the project's total energy and final profitability. This is essentially due to the wake effect. That is because the wind turbines extract energy from the wind, and wind flow downstream is characterized as turbulent and disturbed, where wind speed is decreased. The wake spreads and grows towards free stream conditions as the flow continues downstream. Since a wind farm is composed of many turbines, this disturbance causes the wind speed field to be intensely dependent on the position of each wind turbine. Some studies [23] [73] [72] describe the layouts would provide an improvement in the AEP by at least 5%. This improvement in AEP would have necessary consequences in terms of annual income and consequently on the project's profitability. Therefore, the attention paid to optimization techniques utilized to the problem of the micro-siting of wind turbines on a wind farm is justified. Earlier studies [74] [75] essentially focused on the calculations or experiments on wake flow and the optimization approaches on micro-siting. A genetic algorithm (GA) is the most commonly used among the optimisation approaches. Some researchers [76] have done a detailed analysis of GA. Most of these approaches employ the linear model for calculating turbine wake flow that Jensen proposed in 1983, where the wind turbine affects the wind speed downstream and the wake effect of a wind turbine [76]. The Jensen model [22] is an estimated description of the velocity distribution within the wake flow area, with experiential constants according to experimental measurements. Jensen model handles the wake flow as a conical area, in which the velocity only depends on the distance downstream from the turbine center. This model calculates the wake flow very fast on flat terrain. It is utilized during the GA optimization to estimate the whole power output for each layout [74].

3.2 Microgrids

Microgrids are commonly used to provide electricity to rural areas or remote regions. They can also operate independently or in concert with other small power grids. A microgrid can be defined as a network of interconnected power plants and storage facilities commonly found in rural areas. Generators or solar panels can operate to provide backup power during high demand, which helps minimise the impact of local blackouts by integrating renewable energy sources such as solar and wind. Joining up

with smart grid deployments can help local microgrids make money by selling excess energy back to them [77]. Hybrid microgrids are systems that are composed of multiple electrical sub-grids. These grids are usually linked by electronic circuits and are designed to operate autonomously. As more power electronic converters are used in distributed generation and energy storage systems, their applications become more sophisticated [78].

The increasing penetration of single-phase/unbalanced loads and non-linear loads has raised the need for more robust power quality controls in hybrid microgrids. DC-Sub grids have the potential to face various power quality issues. Most of these issues can be caused by voltage variations and harmonics. AC-subgrids can also face these issues. The main factors that affect their power quality are voltage variations and harmonics [5]. In [78], the authors showed how additional compensation devices could be installed to improve such power quality issues. For example, unbalanced AC-side three-phase can be compensated using static synchronous equipment power electronics-based equipment such as a unified power quality conditioner (UPQC). More example, for AC-side harmonics, active and passive power filters (APFs) (PPFs) can help minimize the effects of these components and install large capacitors, and tuned filters can easily filter the DC-side harmonics and variations. Also, the authors discussed some power quality issues in real-world hybrid microgrids. For example, Data centres are expected to consume 20% of electricity in the United States by 2030. Unfortunately, poor power quality can result in millions of dollars of loss annually. Although it is possible to mitigate power quality issues through centralized compensation methods, the additional equipment required to deal with it does not solve the problem. Due to the increasing number of smart grid devices, such as intelligent interfacing converters, which can be used in hybrid AC/DC microgrids, they can help minimize the issue of power quality [78].

The characteristics of various power sources used in Microgrid operation have been studied to establish stability. The research in [79] aimed to investigate the feasibility of dynamic control of an electrolyzer system for achieving real power balance and discussed the various control techniques that can be utilized to extend the system's capabilities. This method is considered a means of improving the frequency fluctuation control capability of the system. Since wind and solar generators can produce unstable power output, they can cause sudden power to unbalance in hybrid systems. A dynamic control method is presented for an electrolyzer system to secure natural power balance. Control frequency fluctuation and the frequency and tie-line power fluctuations are analyzed to show that the proposed dynamic control method can improve the quality of the system's power [79].

A microgrid can be operated autonomously and connected to the primary grid (utility grid. If any fault occurs while operating in grid-connected mode, the microgrid can disconnect itself from the grid and work independently [80]. In the microgrid system, there are two modes of operation

The Grid-connected mode, where the primary grid is connected to the utility grid, and the feeders are linked. The grid-connected mode regulates the network's voltage, frequency, and phase. The phase at the point of standard connection (PCC) is also known as the common coupling. This is where the electronic components are coupled to a distributed energy source. The converters system is electronically connected to distributed energy sources dedicated to one load or group. When used as network-feeding, their network controls these devices and can operate similarly to current sources. Moreover, the grid-connected mode is mainly used for non-dispatchable intermittent energy sources that require maximum power point tracking (MPPT) algorithms, which are credited for extracting the maximum obtainable power from generation sources [81]. Power converters can also control the voltage component of non-disposable sources. They can also supply the network feeders with the required power quality standards. A network-forming converter is a type of device that is commonly used in dispatchable generators and energy storage devices. It uses a phase-locked loop (PLL) function to control the voltage and frequency at the grid [82]

The island mode allows operating without the primary grid's power supply. It can also prevent power outages once the grid is offline. For specific reasons, such as network quality issues or faults, a utility or a grid operator can initiate the intentional islanding mode. Island operation mode is a process that involves maintaining the continuity of supply, which can save money and reliability improvement [83]. A transient operation mode refers to the grid-connected mode transitions to an islanded one. This process usually involves connecting the supply to the power grid as it is crucial for the restoring process to be reliable with minimal or non-disturbance. During the transient phase, the transmission and

distribution of electricity must be synchronized. This can be done by forming a distributed generator network or establishing a cooperative network [84].

The two main components of a hybrid microgrid are the AC and DC generators. The generators can be interconnected through power converters to form a more significant, reliable, and resilient system [85]. The AC and DC microgrids can be isolated and operate seamlessly. The DC microgrid can include various electrical components such as PV systems, Energy Storage Systems (ESSs), and related loads, typically connected to a common DC bus [86]. The AC microgrid can have different components, such as a diesel generator, a wind turbine, and an AC load. It can also be isolated from the primary power system [87]. Hybrid microgrids can use parallel-connected power converters to connect their buses. However, this method can be challenging due to specific technical issues [88]. To regulate Power Flow Control of Interconnected AC–DC Microgrids in Grid-Connected Hybrid Microgrids, the study [89] presented a new approach for controlling the flow of electricity. Instead of using parallel-connected power generators, these interconnected systems are powered by a modified unified interphase power controller (UIPC). The modified structure of the UIPC allows a reduction in the number of power converters. As a result, the UIPC has been considered an alternative power flow control method in hybrid microgrids. It can provide better efficiency and lower cost than the parallel-connected power converters in the grid-connected hybrid microgrid. The UIPC have various advantages, such as it can easily control the flow of electricity between a microgrid and its ILC without requiring the use of cumbersome constraints. Moreover, the proposed UIPC features a voltage isolation feature that can be utilized with parallel-connected ILCs [90] and can control a DC microgrid's DC bus and AC bus voltage. This feature was not possible with the parallel-connected ILCs.

Hybrid AC/DC microgrids are considered advantageous for various reasons such as lower component cost, better power quality, and higher efficiency. They are also known to operate efficiently and provide security. Interlink AC/DC converters connect a hybrid microgrid's AC and DC components. The proper operation and control of the AC and DC components are necessary to maintain the system's security. The control system of these devices is essential to maintain the system's security [91] [92]. In [93], the research aimed to develop a coordinated control strategy for interlinking bidirectional AC/DC converters (IC) and a battery storage system (BESS) under standalone operation to provide better power-sharing between the AC and DC subgrids. In standalone mode, the system's security can be jeopardized if the output power of one subgrid cannot meet the load demand of another. The proposed coordination strategy between the BESS and IC converters can help minimize the risk of power transfer between DC and AC subgrids in standalone mode. Since The IC plays a crucial role in operating a hybrid AC/DC microgrid, it should be equipped with a proper power management system to ensure continuous operation. They conclude that the active power injection should be managed along with the battery's physical limits when the BESS is fully charged or exhausted. This concept can provide a smooth transition from the active to the standby mode, even in low-voltage conditions. The simulation results showed that this control strategy could efficiently handle the power transfer even in low-voltage conditions.

In South Korea [94], many efforts are focused on developing microgrids that can operate on island or university campuses. They proposed using a pumped hydroelectric system as a storage system. The utilization rate of the pumped hydroelectric system is lower than that of other power plants, which indicates that its generators are not being used efficiently. They looked to find a way to generate electricity by using the idle surface of water through floating solar panels. This method is considered as a potential solution to the power shortage. This study focused on developing a microgrid that could provide stable and secure power to end-users. Using a battery and a pumped hydroelectric system offers a balance of power. The main goal of this study was to minimize the battery's capacity to avoid its disadvantages, such as high-cost competitiveness. The microgrid's ability to provide reliable and resilient power is expected to benefit significantly from grid reliability research. Aside from reducing grid uncertainty, this system can also provide reliable and robust power to meet the needs of nearby regions.

3.3 Hybrid microgrid design and optimization Techniques

Hybrid microgrids that combine multiple energy sources such as solar and wind are becoming more prevalent. They can provide reliable and cost-effective power while reducing carbon footprint [95]. A microgrid system's optimal design and sizing can help minimize its life cycle cost and provide high-quality power. The optimal microgrid scheduling model is a multiobjective problem. There are different methods to solve this problem. One of the most standard methods is transforming the multiobjective problem into a single-objective problem [96]. Metahistic optimization techniques are more advantageous than traditional methods in designing and operating microgrid systems [97].

The authors in [98] proposed an operation optimization model for standalone microgrids, which considered the battery system's depreciation, environmental protection, and economic costs. A strategy based on the grey target decision-making method is proposed to help users pick the optimal solution for the distributed energy system. This method is tested in a standalone microgrid in China. This research combined the particle swarm optimization algorithm (PSO) and the simulated annealing algorithm (SA) to search for the optimal solution set for the operation problem that both algorithms take advantage of. This approach introduced a mathematical model for the various microgrid system devices, which was then proposed as one of the main goals of the system's operation. A multiobjective function is needed to determine the economic operation of a standalone microgrid. It involves taking into account the various factors related to the system's operation. The results showed that the economic and environmental costs are not exclusive to standalone microgrids on remote islands. The increasing battery depreciation cost significantly influences microgrids' economic and environmental costs. The simulation results show that an energy storage battery

can effectively absorb solar energy during the day and release it at night, and the maximum capacity of the battery system is reached when the economic cost is the minimum. The study showed that the hybrid SA-PSO algorithm could improve the objective function value and provide better robustness.

Similarly, the authors in [99] proposed an elite converter that can maximize the utilization of hybrid energy sources such as solar, wind, and battery in microgrid systems. The proposed elite converter is a high conversion ratio DC-DC converter that is optimized for use in microgrids. The hybrid approach integrates the adaptive whale optimization algorithm (AWOA) and the adaptive neuro-fuzzy interference system (ANFIS). The resulting product, which is called (AWO-ANFIS), is suggested, and hence, it is named as AWO-ANFIS technique. The (AWOA) technique is used to control the output signals of a wireless device by monitoring the power variation between the source side (renewable energy source) and the load source. ANFIS technique is used for error underestimation by using the achieved dataset from the AWOA technique. The proposed system is composed of a DC-DC converter and an AWO-ANFIS control scheme. The system's primary goals are to maximize the utilization of available RESs and minimize the switching loss. AWO-ANFIS controller handles the optimal generation of a control signal. Then the signal is exchanged with wind and PV systems' (MMPT) controllers. This technique is compared with the existing methods such as the genetic algorithm (GA) [100], particle swarm optimization algorithm (PSO) [99] and the whale optimization algorithm (WOA) [101] by using the three types of case studies. Through a simulation, it has been shown that integrating MGs with the AWO-ANFIS control scheme can improve the system's efficiency and showed that the proposed method could improve the performance of these components in terms of current, voltage, and power signal.

Moreover, One of the most important considerations that a hybrid system designer has to consider is the optimal sizing of its components. This helps ensure that the system can handle the load requirements with minimum financial investment. In [102], the hybrid genetic algorithm and particle swarm optimization technique (GA-PSO) were used for an off-grid house's optimal size with solar panels, wind turbines, and batteries for the suburbs of Tehran to minimize the total present cost of a hybrid PV-wind turbine system and maximize its reliability. The multiobjective technique (MOPSO) was also applied, which could reduce the total cost of operations and maintenance by considering the various factors involved in running a system. The proposed approach is based on designing optimal systems that can handle multiple configurations. The Levelized Cost of Energy (LCE) factor evaluates the system's validity. Various scenarios were considered for the simulation, including a battery bank system, a PV

panel, and a wind turbine with a battery bank. The loss of power supply (LPS) was calculated using GA-PSO. The results indicate that the PV/WT/BAT system has a lower cost than the other systems.

In a similar pattern, the authors in [103] presented the performance of different PSO variants to determine the optimal dimensions of hybrid solar, wind power, and storge battery bank systems. The optimal size of the system was one of the main factors influencing the cost-effectiveness of a hybrid system. The study was conducted in different remote regions of Iran, using various particle swarm optimization variants (PSO). The results showed that the algorithm with a particle swarm optimization constriction factor (PSO-CF) is better than other PSO methods. The particle swarm optimization algorithm with adaptive inertia weight (PSO-W) can also be used to determine the optimal size of a hybrid system. According to an economic analysis of Iran, hybrid systems are generally suitable for areas with low solar radiation and low wind speed.

In [104], the research aimed to optimize the capacity sizes of various hybrid solar/wind power components by modelling the various components through an iterative approach. The case study analyzed in this paper pertains to a hybrid project designed to supply electricity to a residential household in Bouzaréah, Algeria. The proposed model considers the various submodels of hybrid systems, the Deficiency of Power Supply Probability (DPSP) and the Levelized unit electricity (LUEC). With this incorporated model, the system reliability and capacity utilization of grid-independent hybrid solar/wind power generation systems can be optimized technically and economically. The results showed that when the system's reliability is higher, the configuration of the system's modules and wind turbine power also increases, and the structure of a system can help minimize system downtime and maximize system longevity. When the system has multiple days of storage capacity, the wind turbine and PV modules' power is more moderate than a single day-storage battery bank.

The optimal configuration for a system meets the system's reliability requirement with the least amount of LUEC. In most cases, this configuration is recommended when the system's capacity and the number of PV modules are moderate. Different sizing tools are used for estimating the optimal size of various components of a system. They provide detailed information about the energy flows within the system, such as Homer [105]. The Hybrid Optimization Model (HOMER) is commonly used in renewable electric energy. It is free software that can be used to perform quick preferability assessments. It uses various inputs such as components costs, technology options, and available resources to generate a list of feasible configurations. HOMER can help identify the optimal structures for multiple systems. It can also create tables and graphs that can be exported [11]. In [106], the authors discussed the feasibility of using hydrogen as an energy carrier in Newfoundland, Canada. Diverse renewable and non-renewable energy sources and their associated energy storage methods are also discussed. The study was performed with the help of the HOMER tool. It was used to analyze the various factors related to the operation of a remote house, such as wind speed, solar radiation level, and fuel cell cost. A reduction in the price of fuel cell technology would make a wind-fuel cell system a better choice. This paper analyzed the various factors that affect the profitability of such systems. The results showed that Newfoundland has abundant wind resources that can be utilized efficiently. However, the cost of solar energy is not always economical in most cases and instead of single standalone generators, hybrid systems could be used for remote communities. Moreover, a wind-fuel cell system would be attractive if the fuel cell cost is reduced to 15% of its current market price. However, before a wind-powered fuel cell system can be considered commercially viable, further studies must be conducted.

3.4 Wind energy integration into a microgrid

One of the most significant contributors to the modern electric grid is wind energy. However, its various characteristics, such as its intermittent nature, protection issues, and technological limitations, can affect the efficiency and reliability of the system [107]. The following are various challenges that wind energy integration can bring to the grid [108]. However, some of these challenges will be reviewed later in this section

- Output power prediction
- Reactive power and voltage support
- Impact of the frequency
- Protection challenges
- Low voltage ride-through capability
- Planning challenges

- Socio-economic and environmental challenges
- Impact of the harmonics /power quality
- Grid reliability and resiliency
- Transmission, communication and security challenges
- Electricity market challenges
- Angular stability /inter-area oscillation

The integration of wind power into the grid presented various challenges. Simulation and modelling techniques are needed to address these issues. There are multiple ways to solve problems, such as oversizing everything. However, these are typically ineffective and result in costly and inefficient power systems [109]. The various solution methodologies are available to resolve the challenges, such as grid codes, advanced monitoring, control strategies, energy storage systems and the last renewable energy policies.

Today's world, wind turbines have become more sophisticated in their designs and can handle various network problems [108]. Despite the improvement that has been completed in the field of wind energy, there are still concerns about its integration into the electricity grid, and it is expected that various new solutions will be developed shortly. The durability and longevity of energy storage systems are among the most critical factors manufacturers and energy storage companies consider when developing their products. Researchers should also study the various aspects of energy storage to find solutions that can prolong the life of these systems. The characteristics of these systems can help integrate wind energy into the grid. They can also help avoid issues related to the dispatchability of the system. Besides, new probabilistic methods uncertainties/studies can improve prediction accuracy and reduce the computational burden. The researcher should also study the link between the wind energy system's uncertainties and the demand side management strategies to ensure the system's reliability [108, 109].

The increasing number of wind energy connected to microgrids presents various dynamics and power quality challenges to the electrical grid since the varying nature of wind and the different generation systems used for electricity generation can affect the operation of the grid. This can result in various issues, such as the system's failure or power quality. The authors in [110] aimed to address these issues through flywheel energy storage and improve the FES controller's performance, where simulation tests are performed to analyze the behaviour of the flywheel energy storage (FES) device when it is used in combination with wind generation. Since flywheel energy storage (FES) can help minimize the effects of power flow fluctuations in distributed generation systems, a dynamic model of a flywheel energy storage device was presented to demonstrate a technique to control the power that the device sends to the grid. A control algorithm for a device was proposed that uses three control modes. The first one is a fuzzy inference system that can control the wind power fluctuations caused by wind generators. The second control mode prevents the frequency control from affecting specific faults. The third control mode maintains the constant voltage. The study results indicated that the control algorithms developed for the FES device work well. They effectively compensate for the effects of the active power fluctuations. The system's complete design contributes to a smoother power response. It also helps recover the frequency when faults occur. Therefore, The FES controller can better compensate for wind turbine AC microgrids[110].

In a similar topic, the authors in [111] strived to study the intermittent characteristics of wave and wind power generation systems by proposing an integrated approach. The proposed system would involve a wind and wave power generator fed into an ac power grid or connected to a DC microgrid. The system would use a voltage-source converter (VSC) and a wave power generator to connect to the grid. It would also utilize a battery storage system. The system is modelled and simulated using a written program based on the MATLAB/Simulink software. They presented a laboratory-grade test system to investigate the operating characteristics of an integrated system that uses a DC microgrid to provide isolated load conditions. The study revealed that an integrated system with a DC microgrid could maintain stable operation when subjected to a sudden load-switch condition. The DC microgrid can maintain a stable operation even in different operating conditions.

3.5 Preliminary Study

This study is based on preliminary work done in the fall semester of 2021 [112] and will briefly be described in this section. The preliminary examination is based on the micro-siting of wind turbines and a review that considers the issues when micro-siting wind turbines in an urban area. The study case is located in Agder county, in an industrial location called Kjerlingland in Lillesand municipality. The study was conducted for a food production facility called Gorines, where the primary goal is to get at least 500 MWh from the proposed wind turbines project, covering its shortage in the annual demand. However, the plan is to become a prosumer, i.e. energy exporter, where the excess energy should be exported to neighbours in the industrial site or directly to the grid. Therefore, several scenarios (layouts) have been tested to estimate the size, number, and AEP by selecting different types of wind turbines and turbulence models, see Figure 14. in this sense, the simulations considered two different turbulence models, namely k-omega and k-epsilon to simulates the wind flow correctly in the terrain.

Nevertheless, these simulations did not consider the buildings surrounding Gorines and its future expansion plans. However, a modification to the raw grid terrain data was done to manipulate the elevation and the roughness data to mimic the existence of the building in the studied terrain see Figure 15. According to the results, a minimum 600 kW total capacity system is determined either as one single turbine or as four turbines of 150 kW each. The turbines should be located in specific areas. These areas have been identified, considering the future expansion plans Gorines has. Table 1 shows the proposed layouts' specifications.

Table 1. Layouts' turbine specifications.

	Layout 1	Layout 2
Number of turbines	4	1
Turbine's capacity	150 kW	600 kW
Rated speed	16 m/s	13 m/s
Hub height	34 m	50 m
Rotor diameter	24 m	44 m

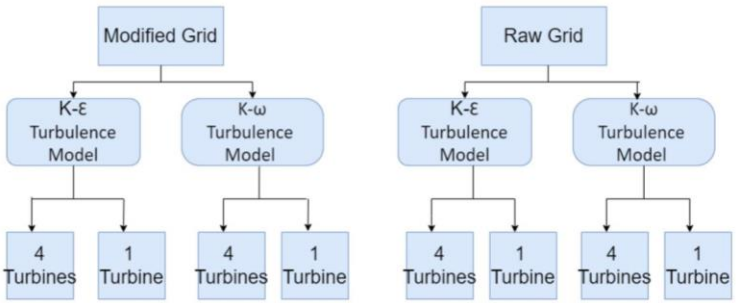

Figure 14. Previous research methodology flowchart.

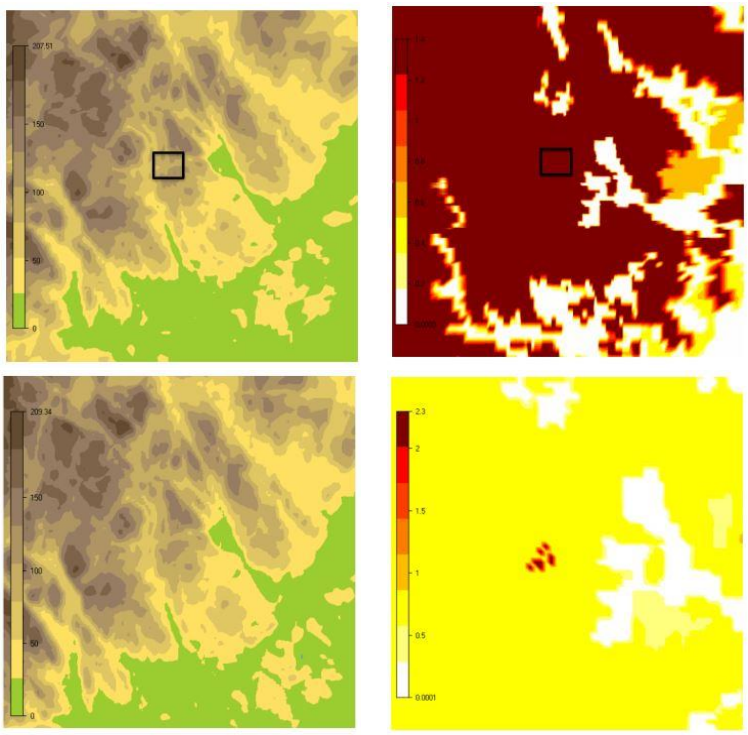

Figure 15. Raw grid data (top) vs modified grid data (bottom).

The convergence of wind field simulations is analyzed by inspecting the residual values for the various velocity components and the turbulent kinetic energy. The simulations for wind direction sectors converged after around 100 iterations. Using a more advanced turbulence model (k-omega) yielded more iterations to reach convergence than a simple turbulence model (k-epsilon). Moreover, it was found that the simulations based on using modified grid data (elevation and roughness) with the k-epsilon turbulence model have not affected the convergence criteria in establishing the wind database in the wind fields module. Surprisingly, the number of iterations for all the wind direction sectors is precisely the same as using the raw grid data. This behaviour can be explained as the modifications were applied to a small area inside the studied domain, which would not have a remarkable effect on the stability of the flow. Also, the simulations based on using modified data with the k-omega turbulence model have the same number of iterations for all the wind direction sectors compared to the simulations using raw data with k-omega. Also, the k-omega model with modified data has shown the same pattern when used with raw grid data. Nevertheless, the mean wind speed and power density have increased while using the k-omega compared to the k-epsilon model results.

The proposed modifications (elevation and roughness) have reduced the AEP for layout 1(4 turbines), considering k-epsilon and k-omega. It is thought that in layout 1 the hub height is within the effect of the modified roughness. In contrast, the turbine in layout 2 has produced more as it is located at a higher level (50m). It is thought that the modified roughness effects have not reached the layout two hub height, contrary to the modified elevation proposed in the surrounding, which may increase the occurrences of the rated wind speed, which yield a higher capacity factor. It should be mentioned that the capacity factor for layout 1 for all the simulations is around 0.33, while for layout 2, it ranges between 0.35 to 0.37.

4 Study case

4.1 Introduction

Gorines has co-located its three production facilities in a new and future-oriented production facility at Kjerlingland in Lillesand kommune, as seen in Figures 16 and 17, which is located in Agder county in the southern part of Norway. Gorines has created a unique facility in terms of climate effects and has used the most optimal, innovative energy and climate solutions possible to use. The solutions achieved in the Climate Impact project significantly improve energy and climate performance compared to existing solutions. ENOVA's support of NOK 10,955,020 of the investment has contributed to reduced risk and sufficient profitability in the project.

Figure 16. Map of the south part of Norway, source: NVE Atlas.

Figure 17. Gorines location in the red polygon, source: Google maps.

In the south region of Norway, there are abundant wind and solar resources to develop a hybrid electricity supply system. Gorines has already installed and implemented solar cells on the rooftop of the building to provide energy when the production line is in need. An integrated monitoring system, 'maximum guard system,' has been developed to monitor and control power production and energy consumption at any instant, as shown in Figure 18. The system recalculates expected production and consumption every minute and adjusts all units. Gorines is also equipped with a battery bank of 350 kWh, and 15 energy wells provide thermal energy used with accumulator tanks to decrease the power requirement for both cold and hot water production. Furthermore, they enable more efficient operation of the heat pump, waste heat utilization and increased own consumption of produced solar power.

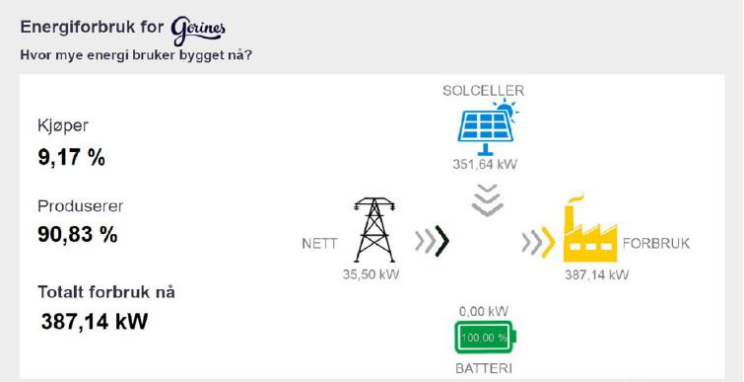

Figure 18. Real-time monitoring for total energy production and consumption.

The annual company consumption exceeds 1000 MWh/yr, whereas the current annual solar cells and thermal production is around 500 MWh. However, the future plan is to transform into prosumer by integrating small wind turbines to produce over 500 MWh annually, as the small wind turbines are thought to show significant improvements in the following aspects:

- Stabilization of power network.
- Local production of energy in an area with high demand.
- Cooperation on energy and power locally and regionally.
- Dispersion effect-strong impact on other businesses in the same segment.
- New solution for economically sustainable models to succeed in creating a climate-neutral society.
- Utilize an area to build smaller turbines that do not bother and give a significant effect.
- Reduce the need for network development in the area.

4.2 Terrain and roughness data

In order to simulate the wind flow in the studied site, both elevation and roughness data are essential, which are available at different sources. Concerning the elevation data, the Shuttle Radar Topography Mission (SRTM) database has been used to provide good resolution information (90m) and is publicly accessible. SRTM consisted of a specially modified radar system that flew onboard the Space Shuttle Endeavour during an 11-day mission in February of 2000. These data are obtained elevation on a near-global scale to generate Earth's most complete high-resolution digital topographic database [113]. Figure 15 (top-left) shows the extracted elevation data for the studied site, which is located at around 100m above sea level. The surroundings vary in elevation ranging from sea level up to 210m for the Nearby mountains, indicating the site's complexity regardless of being urban. It should be mentioned that the buildings in the studied site were built after the creation date of SRTM data. Therefore, it is necessary to consider including these buildings as obstacles in the simulations.

The CORINE Land Cover (CLC) inventory provides data collection on land in Europe to support environmental policy development regarding the roughness data. CLC was initiated in 1985 and consists of 44 land cover and land use classes derived from a series of satellite missions since it was first established. Figure 15 (top-right) shows the roughness data for the studied site from the 2006 update. In a significant part of the terrain studied, the roughness was above 1m, which indicates a terrain with forests (trees), natural vegetation, stubs and rocks spread around [114, 115].

4.3 Wind data

The studied site does not have any historical wind measurements that are crucial to the simulation. Alternatively, reanalysis data from the European Centre for medium-range weather forecasts (ECMWF), particularly ERA5 data, are available. ERA5 provides hourly estimates of many atmospheric, land and oceanic climate variables. The data cover the Earth on a 30km grid and resolve the atmosphere using 137 levels from the surface up to a height of 80km. ERA5 also combines vast amounts of historical observations into global estimates using advanced modelling and data assimilation systems. Figures 19

and 20 show a period between 2018 and late 2021 for both wind speed and direction, respectively, extracted at 50 m height which was utilized in this study. According to the data, the studied site has an average hourly wind speed of 7m/s. Figure 21 shows that the wind mainly blows from 240 and 270, WSW and W, respectively, and from 30 and 60 NNE and NE. To illustrate more, Figure 22 shows the wind direction versus wins speed highlighting the two main clusters where the wind blows from.

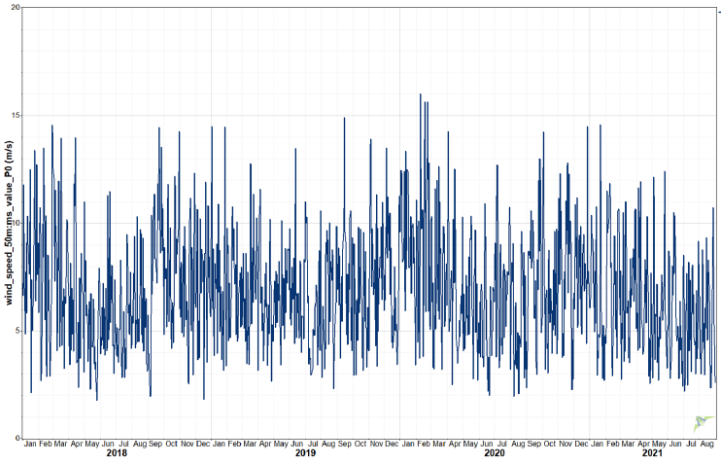

Figure 19. The average daily wind speed.

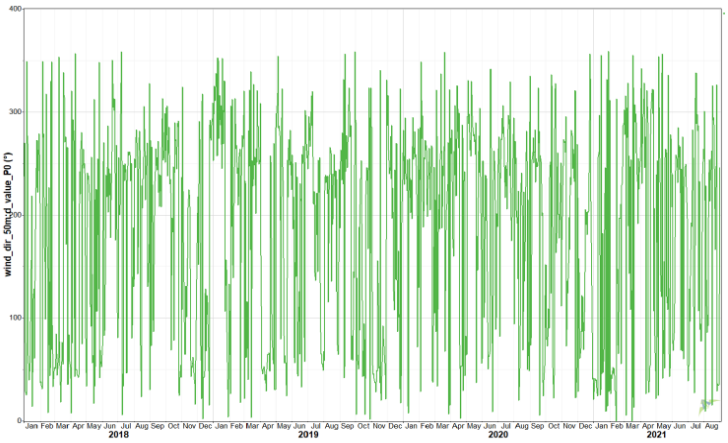

Figure 20. The average daily wind direction.

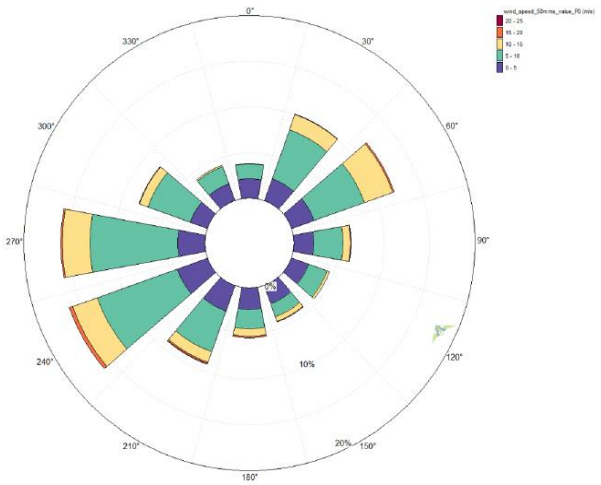

Figure 21. The site wind rose (speed vs direction).

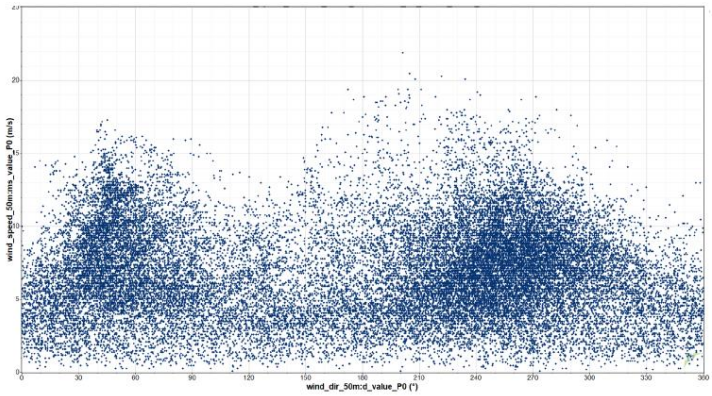

Figure 22. Hourly wind direction versus wind speed.

As mentioned earlier, through the previous research, a decision of two layouts has been made, where two kinds of wind turbines have been selected following two simulations. Figures The power curve of the 600 kW wind turbine is presented in Figures 23 and 24, showing the power curves for the selected types of turbines (600 and 150 kW). Some of the turbines` specifications are described in Table 3.

Table 2. Selected turbines` specifications.

	Turbine type 1	Turbine type 2
Turbine capacity	600 kW	150 kW
Hub height	50 m	34 m
Rotor diameter	44 m	24 m
Cut- in wind speed	4 m/s	4 m/s
Cut-out wind speed	20 m/s	25 m/s
Rated wind speed	16 m/s	13.5 m/s

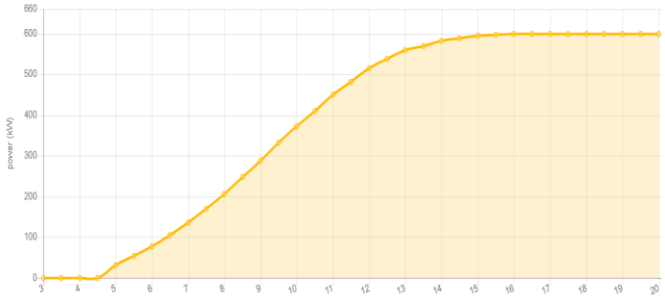

Figure 23. The power curve of 600 kW wind turbine.

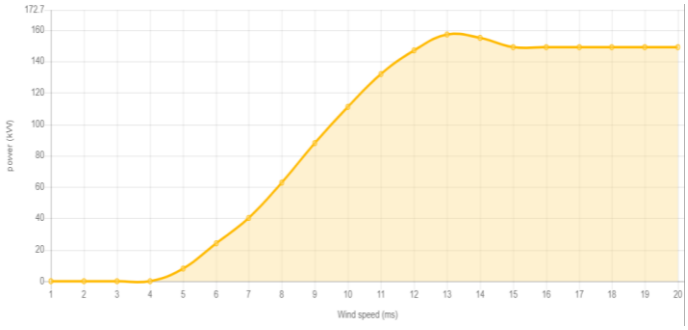

Figure 24. The power curve of 150 kW wind turbine.

Due to the increasing demand for wind turbines, the price of these products has been increasing. There is a wide range of sizes and types available. Typically, 1 MW of installed capacity would cost over 1 M USD. In this study, a 600 kW wind turbine is used with an estimated cost of 700000 USD. Not every wind turbine component will scale up to the same size. Many components are similar to other turbines (a few extra metres of wire will not cost very much). Moreover, the size of the wind turbine may vary, and the time it takes to build two different ones will not be significantly different [116].

4.4 Solar data

4.4.1 Location horizon and sun path

The amount of solar radiation needed to produce electricity is significant when choosing a solar system location. The region's latitude and the surrounding mountains determine the solar system's height and path. Also, clouds and rainfall can affect the amount of solar radiation produced. The sun path and height of the specific location in the Lillesand can be seen in Figure 25. In Lillesand, the sun path never reaches higher than about 60 degrees above the horizon. The amount of air mass that the sunlight must pass through before it reaches the panels affects the output of solar panels. This increases the amount of diffuse light that can scatter and lowers the panel's output.

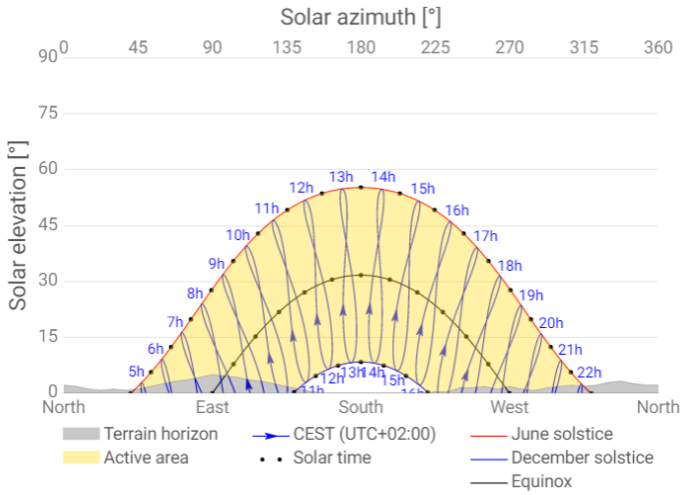

Figure 25. Horizon and sun path diagram of company location (source: Global Solar Atlas).

4.4.2 Gorines' installed solar panels

The solar cells were installed on the Gorines roof to provide the maximum energy output when the production needed it, as shown in Figure 26. A solar cell system of 6,000 m^2 has been installed and is now in full operation. The size of a solar panel system is a significant factor that will affect the cost of installation. Other factors such as the area where the company is located and the local incentives available will also affect the cost of solar panels. The price of solar panels is also influenced by the type of equipment that the manufacturer uses. Aside from the manufacturer's brand, other factors will also affect the cost of a solar panel system, for instance, the type of inverter, the racking system installed, etc.

Gorines decided to install two types of solar panels with a total capacity of 614 kW. The Canadian Solar brand supplies the first one with a flat plate panel with a total rated capacity of 362 kW. These panels use mono-crystalline PERC cells with a dark-coloured back sheet and black frame to enhance the aesthetic appearance with a nominal max power of 290W. The Jinko Eagle brand supplies the second type with a rated capacity of 252 kW, with a nominal maximum power of 300 W. Some properties of these two types of solar panels are explained in Table 4.

Figure 26. Gorines' roof equipped with solar cells.

Table 3. Solar poanels properties.

Property	Solar Canadian CS6K -290MS	Jinko Eagle PERC60 300W
Panel Type	Flat plate	Flat Plate
Rated Capacity (kW)	362	251.4
Temperature coefficient	-0.390	-0.390
Operating Temperature (C°)	45	45
Efficiency %	17.72	18.33
Manufacturer	Canadian Solar	Jinko Solar

The cost of the Canadian Solar CS6K-290MS in the market for 290 W is around kr.3000, and the Jinko60/300 costs around 1500 kr for each 300W. A 614 kW system was installed, consisting of 1048 panels. Table 5 presents the cost summary of the PV modules installed.

Table 4. Cost summary of the installed solar panels.

Canadian CS6K-290MS & Jinko60/300	300W for each type
Panels numbers	1048 panels
Total capacity	614 kW
The average cost in $	472.528
The average cost in NOK	3,780.224

From early June to mid-October 2021, the modules produced 425,000 kWh. In the first three months of 2021, electricity production decreased by 10% due to technical issues with the inverter.

Figure 27 shows the production profile in a typical year. If this is used as a basis for estimating the annual production, it will be able to produce around 788,000 kWh, as it includes the operational problems that have occurred during that year. This is 10% higher than the volume of 714,000 kWh / year estimated in Enova's application, which shows a very positive sign.

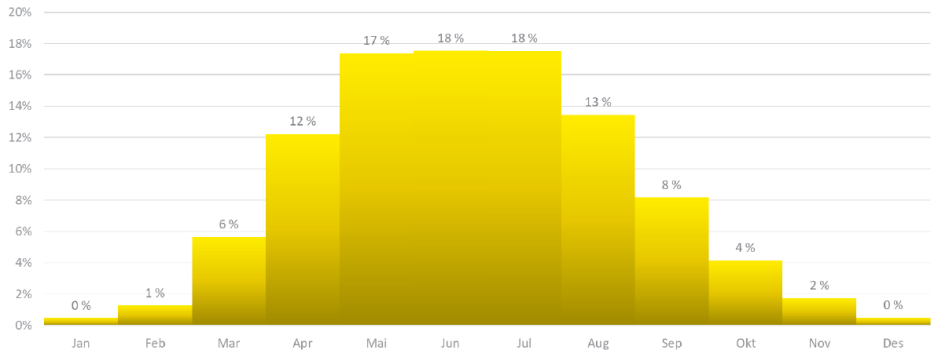

Figure 27. Simulated profile of solar energy production.

However, Figure 28 presents the monthly solar production of 2021, which varies throughout the year. That is expected since there is less sun in the winter than in the summer. Moreover, the peak Production is between May and September months. The solar altitude is the highest on 21st of June. Therefore, it is expected to have a peak production around June. However, June 2021 has had some issues, and some modules have had to be shut off.

Moreover, having a higher production in March than in October can reflect the solar irradiance due to snow or just weather conditions. During the winter season, most parts of the company's electricity are imported from the grid. But on the other hand, the electricity needed from the grid became less when the solar production was significantly good in the summer months.

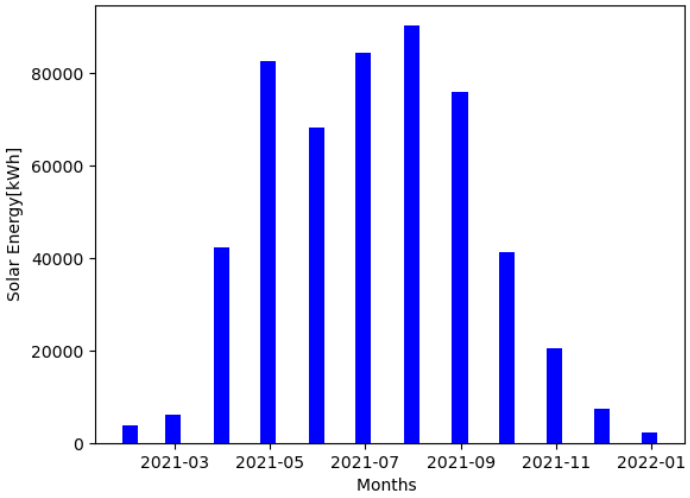

Figure 28. Gorines' solar power system production for 2021.

4.5 Battery

Gorines is equipped with a battery bank of 350 kWh, which can be charged and discharged unlimited times a day. This study selected the battery NEC DSS 340 kWh 739 kW, costing around NOK 7500 for each kW and its properties, as shown in Table 2.

Table 5. The installed battery specifications.

Nominal voltage (V)	720
Nominal capacity (kWh)	340
Nominal capacity (Ah)	472
Roundtrip efficiency(%)	96
Maximum charge current (A)	$1.26*10^3$
Maximum discharge current(A)	$1.26*10^3$

4.6 Load profile

The profile load of Gorines is an essential part of the design process for the hybrid system. It shows the requirements needed of an entity that consumes electricity. As shown in Figures 29, 30, and 31, the peak hours of the consumption are between 06:00 and 15:00 in the daily profile Figure 29. This is further shown in Figure 30, where the red spots present the peak operation hours for the machines. However, the monthly profile load shows fewer variations throughout the year with a constant monthly consumption Figure 31.

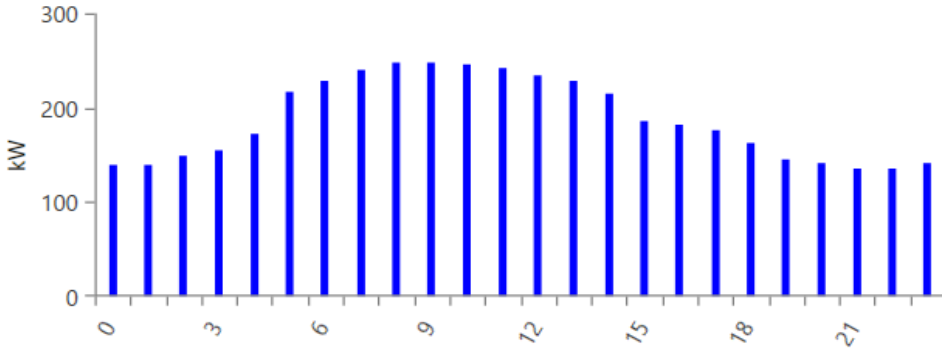

Figure 29. Daily profile of the electric load.

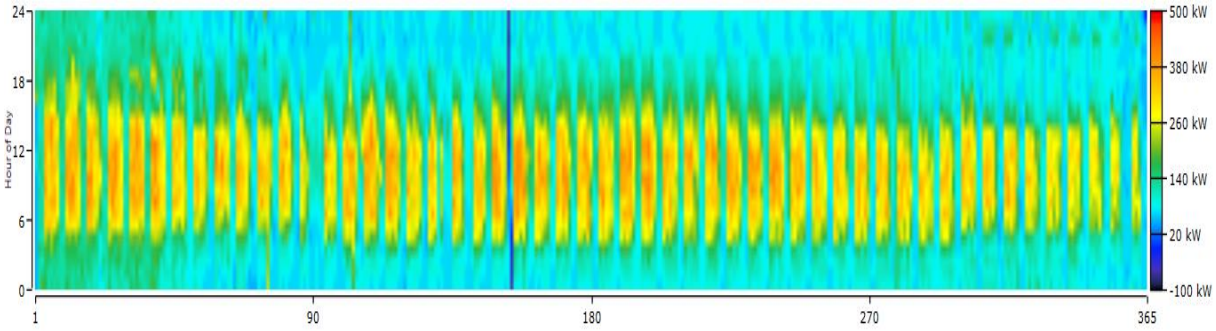

Figure 30. Hourly profile vs hourly price of the electric load.

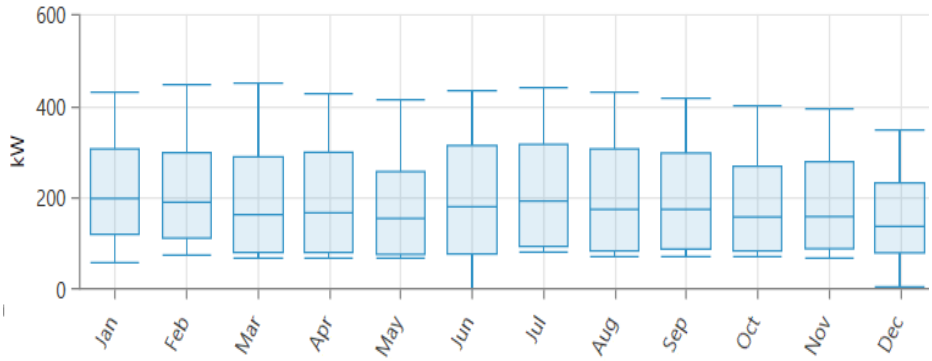

Figure 31 Monthly profile of the electric load.

4.7 Electricity data

The electricity prices used in this project are imported from Nord pool and include hourly values from area Kristiansand (NO3) from the year 2021. Nord Pool is a central marketplace for electricity. There are five price zones in Norway, and the underlying cause of the congestion is that different regions have varying power supply and demand conditions. The data provided by Nord Pool is given in NOK/MWh, which will be converted to the Dollar/kWh to be suitable for the techno-economic study, as shown in Figure 32.

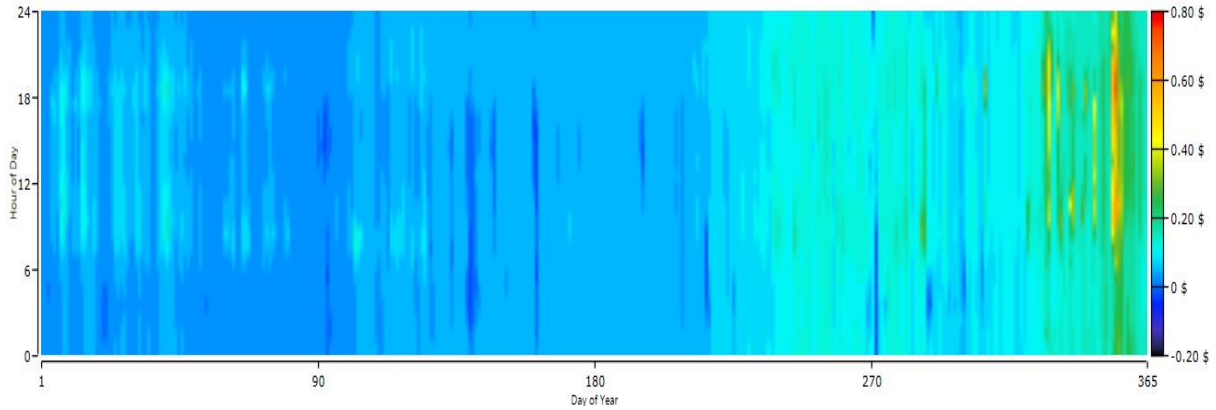

Figure 32. Hourly power prices in Dollars for 2021.

5 Methods

5.1 Micro-siting using (WindSim)

WindSim is a wind resource assessment/wind farm design tool that is based on CFD. Its objective is to maximise the AEP for the farm while also considering the site and terrain constraints. Numerically calculated wind directions and wind speeds are linked against available climate conditions at the site to get the optimal placement for each turbine. On-site observations typically provide the climate conditions, but these conditions can be obtained from meteorological models, as mentioned previously, if observations are not available.

WindSim utilises a modular approach of six modules where all of the modules must be done sequentially in order to complete the micro-siting see in detail [117]. The following subsections will introduce the six modules, terrain, wind fields, objects, results, wind resources, and energy, describing their functions, as seen in Figure 33.

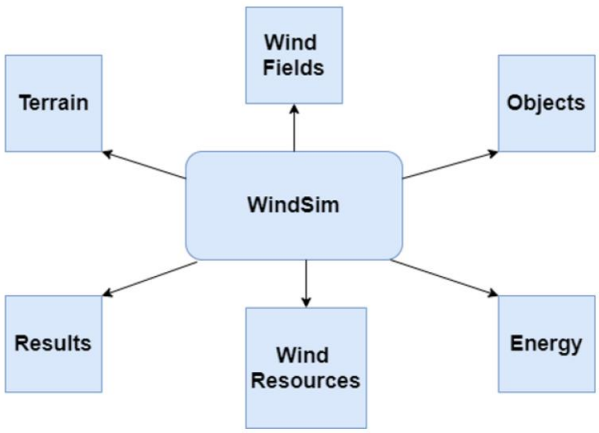

Figure 33. WindSim Software components.

5.1.1 Digital terrain module

A 3D model of the area is generated for the site studied based on roughness and elevation data extracted from different sources, see sub-section 4.2. It is also possible to model forests and other physical objects like buildings to include their influence on the wind fields module. The 2D data set consisting of the elevation and roughness for the studied site will be transformed into a specific grid format (gws) compatible with windsim software. The roughness heights are read from this grid file, where Eq. (20) shows how the roughness is defined.

$$\frac{U}{U_T} = \frac{1}{K} * In\,(\frac{z}{z_0}) \tag{20}$$

Where U is the wind velocity, U_T is the friction velocity, K is the von Karman's constant equal to 0.435, z is the coordinate in the vertical direction, and z_0 is the roughness height.

To understand the urban effects on the studied site, simple modifications were introduced to alter the previously mentioned elevation and roughness data. Previously in [112], a list of coordinates representing the current buildings at the site was defined where elevation data were increased according to the buildings' and the roughness data were increased to match the roughness in corresponding urban areas see Figure 15 (bottom), which were estimated to be between 1.5 and 3 in urban environments. The computational domain is then constructed as a system of hexahedral cells called mesh in 3D, formed based on the digital domain in (gws) [118], as shown in Figure 34.

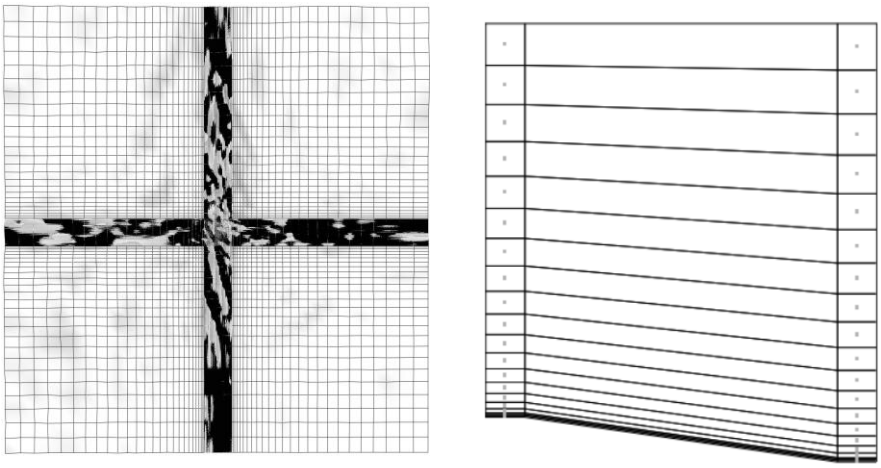

Figure 34. Digital terrain model-Grid (xy) (left), Digital terrain model- Grid (z) (right).

5.1.2 Wind Field module

In the wind field module, the wind database will be created to simulate how the local wind conditions are influenced by the terrain and the other factors in the area. These simulations are based on CFD, which will begin at initial conditions, and then calculate wind estimations at each grid cell. Iterations will progressively determine the solution before a converged solution is found. The in-compressible Reynolds Averaged Navier Stokes (RANS) equations are used as shown in Eqs. (21,22 and 23), paralleled with several available turbulence models.

$$\rho \frac{u_i}{x_i} = 0 \tag{21}$$

$$\rho \frac{\delta}{\delta x_i}\left(u_i - \tau_{ij}\right) = -\frac{\delta P}{\delta x_i} \tag{22}$$

$$\tau_{ij} = \mu\left[\frac{\delta u_i}{\delta x_j} - \frac{\delta u_j}{\delta x_i}\right] - \rho u_i u_j \tag{23}$$

Where x_i is the spatial domain that gets obtained by fluid, u_i is the Cartesian coordinates of a point, i is the velocity, ρ is the fluid density respectably, P is the pressure, The Reynolds stress tensor is τ_{ij} defined as a turbulent flow, and μ is the fluid viscosity.

This module can utilise the K-ϵ model as the default turbulence model, which belongs to the family of eddy viscosity models. The eddy viscosity V_t is calculated by the following analytical equation (24).

$$V_T = C_\mu * K^2/\varepsilon \tag{24}$$

For high turbulent Reynolds numbers, the standard form of the k-$\mathcal{E}$ model may be summarized as follows

$$\frac{\partial(u_i K)}{\partial x_i} = \frac{\partial}{\partial x_i}\left[\frac{V_T}{\sigma_K}\frac{\partial K}{\partial x_i}\right] - \epsilon + P_K + P_b + \frac{1}{\rho} S_K \tag{25}$$

$$\frac{\partial(u_i \epsilon)}{\partial x_i} = \frac{\partial}{\partial x_i}\left[\frac{V_T}{\sigma_\epsilon}\frac{\partial \epsilon}{\partial x_i}\right] - C_{\epsilon 2}\frac{\epsilon^2}{K} + C_{\epsilon 1}\frac{\epsilon}{K}\left(P_K + C_{\epsilon 3}P_b\right) + \frac{1}{\rho} S_\epsilon \tag{26}$$

However, a more complex turbulence model is required to simulate the urban conditions. In this sense, a two-equation model Wilcox k-omega has been used as seen in Eq. (27 and 28) [119] [120]

$$\frac{\partial(\rho K)}{\partial t} + \frac{\partial\left(\rho u_j K\right)}{\partial x_j} = P - \beta * \rho\omega K + \frac{\partial}{\partial x_j}\left[\left(\mu + \sigma_K \frac{\rho K}{\omega}\right)\frac{\partial K}{\partial x_j}\right] \tag{27}$$

$$\frac{\partial(\rho\omega)}{\partial t}+\frac{\partial(\rho u_j\omega)}{\partial x_j}=\frac{\omega\Upsilon}{K}P-\beta\rho\omega^2+\frac{\partial}{\partial x_j}\left[\left(\mu+\sigma_w\frac{\rho K}{\omega}\right)\frac{\partial\omega}{\partial x_j}\right]+\frac{\rho\sigma_d}{\omega}\frac{\partial K}{\partial x_j}\frac{\partial\omega}{\partial x_j} \quad (28)$$

Where:

$$P=\tau_{ij}\frac{\partial u_i}{\partial x_j} \quad (29)$$

$$\tau_{ij}=\mu_t\left(2S_{ij}-\frac{2}{3}\frac{\partial u_k}{\partial x_k}\delta_{ij}\right)-\frac{2}{3}*\rho k\delta_{ij} \quad (30)$$

$$S_{ij}=1/2(\frac{\partial u_i}{\partial x_j}-\frac{\partial u_i}{\partial x_i}) \quad (31)$$

Furthermore, the turbulent eddy viscosity is computed from:

$$\mu_t=\frac{\rho k}{\hat{\omega}} \quad (32)$$

Where:

$$\hat{\omega}=\max\left[\omega,C_{lim}\sqrt{\frac{2\bar{S_{ij}}\bar{S_{ij}}}{\beta^*}}\right] \quad (33)$$

$$\bar{S_{ij}}=S_{ij}-\frac{1}{3}\frac{\partial u_k}{\partial x_k}.\delta_{ij} \quad (34)$$

5.1.3 Objects module

This module will perform the placement of the wind turbines and the climatology stations based on the extracted meteorology data. One can install wind turbines by referencing a global (or local) coordinate system while defining and visualizing the turbine specifications.

As this study targets small wind turbines, different turbine sizes below 600 kW are considered to maintain a maximum hub height of 50m

5.1.4 Results module

The results module explores the wind field simulations stored in a reduced database covering the vertical extension from the ground up to the height of the decreased wind database as specified in the Wind Fields module. An analysis of the numerical flow variables will then be carried out. Here, one can look in more detail in a 2D horizontal plane at different variables such as wind speed, turbulent density, wind shear and wind direction shifts. Nevertheless, it is also possible to extract 3D sets.

5.1.5 Wind resources module

The wind resource map is established by weighing the wind database created in the wind fields module against the inserted climatology data at the site. This module allows for defining the highest speed-related areas, where these areas are clustered according to their size and wind speeds. The module can also evaluate the possible power production of the area. It is possible to measure the wake effects by applying three different CFD based methods. All of them are single wake models that will determine the normalised velocity deficit, shown in Eq (35).

$$\delta V=\frac{U-V}{U} \quad (35)$$

Where U is wind velocity, V is wake velocity. The velocity deficit is based on the wind database that was settled in the Wind Fields module. Model 1 is based on the Jensen model [121], which provides a

straightforward linear development of the expected wake. The model's equation is based on Eq (36), where the wake grows with the raised level of turbulence. Jensen model has become the base for every wake model

$$1 - \frac{U}{U_0} = \frac{1 - \sqrt{1 - C_t}}{(1 + \frac{2bx}{D})\text{^}2} \tag{36}$$

Where U/U_0 is velocity deficit, x is downstream distance, C_t thurst coefficient, b constant. Model 2 is based on the Larsen model, which is similar to the Jensen model and obtained from the turbulent boundary layer [122]. Eq. (37) shows how the velocity deficit is found. Where A is the rotor area, C_T is the thrust coefficient.

$$\delta V = \left(\frac{1}{9}\right).\left(\frac{C_t A_r}{x^2}\right)^{\frac{1}{3}}.\left[r^{\frac{2}{3}}\left(3 * C1^2 C_T A_x\right)^{-\frac{1}{2}} - \left(\frac{35}{2\pi}\right)^{\frac{3}{10}}.\left(3C1^2\right)^{-\frac{1}{5}}\right]^2 \tag{37}$$

Model 3 uses a wake expansion that is based on the turbulent depending rate to find the velocity deficit [123].

$$\delta V = \left(\frac{\sqrt{C_T}}{32}\right).\left(\frac{1.666}{K_1}\right)^2 \left(\frac{x}{D}\right)^{-p} EXP\left(\frac{-r^2}{b^2}\right) \tag{38}$$

5.1.6 Energy module

According to the climatology data, the annual energy production is determined for all inserted turbines, their power thrust curve, location on xyz and the frequency table. The AEP based on each climatology is determined separately. Any differences in the AEP based on different climatology are readily available. A climatology is given by its frequency distribution and presented graphically in the wind rose. Additionally, a climatology is given by its Weibull distribution, where the AEP is calculated for both representations [117]

5.2 Python

Python is a general-purpose programming language that can be used for high-level programming. It can be used for developing web and desktop applications. Also, it allows developers to focus on the core functionality of their applications. The simple syntax rules of Python make it easier for developers to keep their code base readable and maintainable. There are many reasons why developers should choose Python over other programming languages. These include its robust standard library, multiple programming paradigms, and ability to work with various platforms and systems [124].

5.3 Techno-economic design and optimization (HOMER Pro)

The Hybrid Optimization Model for Multiple Energy Resources (HOMER) was established by the National Renewable Energy Laboratory in the US. It is now operated by Homer energy. The HOMER model considers various factors such as the load profile, renewable energy sources, and financial details of a component to create a grid-interactive energy system. The program then runs simulations to find the optimal combination of components that can meet the load requirements. The results are then presented in terms of their relative cost-effectiveness. The HOMER program uses a mathematical calculation to simulate various scenarios. For instance, it can integrate renewable energy sources with traditional sources to meet the load demand. The program can also be used for standalone investigations and grid-integrated studies. It can also make inputs of renewable energy sources according to the users' needs. This tool will allow the user to thoroughly investigate the potential of small-power systems before they are used in the final product. It also allows them to compare various configurations.

The HOMER platform helps users visualize and compare various hybrid energy system design options. It also designs the system's physical components and lifecycle costs. The program also considers the effects of uncertainty on the system's load demand. It then decides if renewable energy can meet the

load demand. If the renewable energy sources are insufficient, other sources, such as the grid or a generator, will have to operate and meet the load demand [125].

The HOMER performs various simulation, optimization, and sensitivity analysis tasks. These tasks are designed to analyze a hybrid system's technical feasibility and cost. The software simulates the operation of a hybrid energy system for a year. It takes about a minute to one hour to perform the steps. The software can also perform various optimization tasks, such as calculating the ideal value of the various variables controlled by the user. The software also performs sensitivity analysis, which measures the effects of uncertainty on the optimization results. This technique helps determine the effects of uncertainty on the optimization results. For instance, if the program designer has no control over the user's variables, then the optimization results might not be as good as expected. Eventually, the most economical hybrid configuration can be identified based on the optimization result [125]. The connection between simulation and sensitivity analysis is shown in Figure 35. Optimization may contain multiple simulations or one simulation. The sensitivity analysis can also contain multiple optimizations. However, only one analysis is likely for a given system.

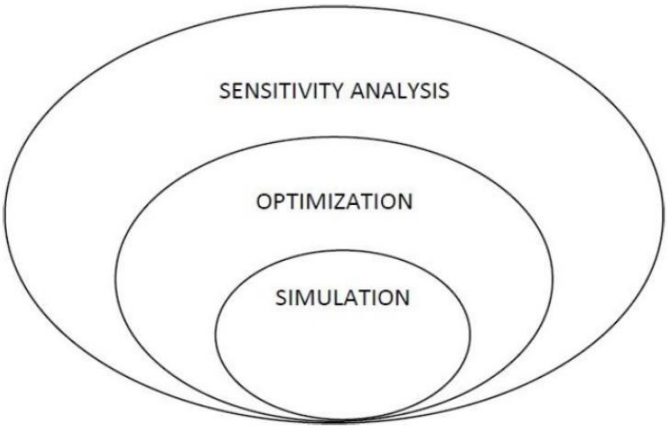

Figure 35 HOMER diagram system [125].

In order to understand how systems work together, HOMER must first model the behaviour of each component. It involves making decisions about the operation of the generators, their charging capabilities, and their sale to the grid. The concept of the operating reserve is critical to HOMER as it affects the decisions that the agency makes regarding the dispatch of power. Operating reserve is a safety margin that helps ensure the reliability of the electricity supply even during times of high electric load and renewable power supply. Every micropower system capable of generating electricity must have some operating reserve to ensure that the electricity supply can be maintained during times of high electric load. The control of the system components is one of the factors that can affect the decisions made by the agency regarding the dispatch of electricity. Each hour of the year, the agency checks to see if the renewable power sources can meet the electricity load and the required operating reserve. If the renewable power sources can meet the load and the operating reserve, the agency will dispatch the necessary system components to provide the necessary electricity. This is the most complex part of the agency's simulation logic. Although the non-dispatchable renewable power sources are easy to model, the complex system modelling required to dispatch them requires time and effort. The complexity of the system modelling process for the dispatchable renewable power sources is due to the need to control the various aspects of their operation to ensure that they can meet the demand and supply conditions [126] [127].

5.4 Modelling and simulation methodology

As mentioned previously, this study continues previous research [112], which shares the same approach. However, some changes have been introduced to tackle the problem of a micro-siting wind energy system in an urban site. The following is a description of the adopted methodology in this research.

This research introduces a modified code (developed in Python) to integrate the buildings in the studied site simulating the flow more accurately than in previous research. To do that, the Windsim mesh file is refined in the correspondent studied area, as shown in Figure 34, and the grid cells containing the buildings are identified based on the coordinates of the buildings. Later, a block is created (as an obstacle) at each identified grid cell representing a part of the building in that exact location.

The modified domain (the new mesh file) is then used to simulate the wind resources by implementing two different turbulence models, simple and advanced, namely k-epsilon and k-omega [112], respectively. Moreover, the simulation results are to be compared with previous results, which are based on the raw grid and modified grid data (see section 3.5), to quantify losses that might arise due to the existence of the buildings.

Contrary to the previous research, only one layout with a single turbine of 600 kW will be realized, based on in-depth discussions with Gorines' team and considering future site developments and the time needed to run the simulations. Concerning these simulations, some general configurations have been unified, as shown in Table 6.

Table 6. Simulations' general configurations.

Refinement area	centred
Height of boundary layer	500 m
Number of wind direction sectors	12
Number of iterations	500 with early stopping
Reference height	50

In addition to that, a techno-economic feasibility study is conducted to realize the economic profit of installing the wind turbine with the existing installed solar and battery storage. The primary goal of a grid-connected hybrid system (wind and PV) is to fulfil the load demand, regardless of the grid's availability or not. If renewable energy production exceeds the load demand, the surplus energy will be utilized to charge the battery or export it to the grid. The grid also can supply the amount of energy required by the system. Suppose the system's production exceeds the load demand. In that case, the excess energy can be used to recharge the battery or feed into the local grid. In this case, the company can fulfil the energy demand in the summer period when the solar production is sufficient or when the wind speed is high enough. However, in peak hours, the energy needed from the grid will be purchased.

This study took into account the load profile of Gorines, the electricity prices in the corresponding region and the solar power production based on data from 2021. To illustrate more, the study examines the economics of wind energy connected to the grid, involving various components such as the battery storage, the solar array, the power converter, the electricity prices, and the electric load. The simulation evaluated the system's performance utilizing weather data under various conditions and estimated the economics of its life cycle. One of the critical elements in this type of study is the grid sell-back price, typically lower than the price of purchasing. A deal must be done with the power supplier to sell back surplus power. However, it is assumed to be equal to the regional spot price at the time-step of production, so the purchase price is equal to the selling price.

It should be mentioned that Python has been, also used in order to process and clean both production and raw weather data. This process prepares the raw data to be suitable for use with the other software used in this study. The observed data at the site was measured at five-minute intervals and converted into hourly data by taking the mean. Moreover, there were missing values in some observed data which they were removed

6 Results and discussion

6.1 Wind energy system simulation

6.1.1 Layout setups

Gorines' primary goal is to get at least 500 MWh from the proposed wind turbines project, covering its shortage in the annual demand. However, the future plan is to become a prosumer, i.e. energy exporter, where the excess energy should be exported to neighbours in the industrial site or directly to the grid. Based on previous research simulations [112], a wind system of a minimum of 600 kW is determined to be installed. However, these simulations did not consider the buildings surrounding Gorines. The system should be located in specific areas (red and blue dots) corresponding to the two proposed layouts, as shown in Figure 36. These areas have been identified initially, considering the future expansion plans Gorines has. However, a decision was made to use the red dot location for the proposed single 600 kW turbine.

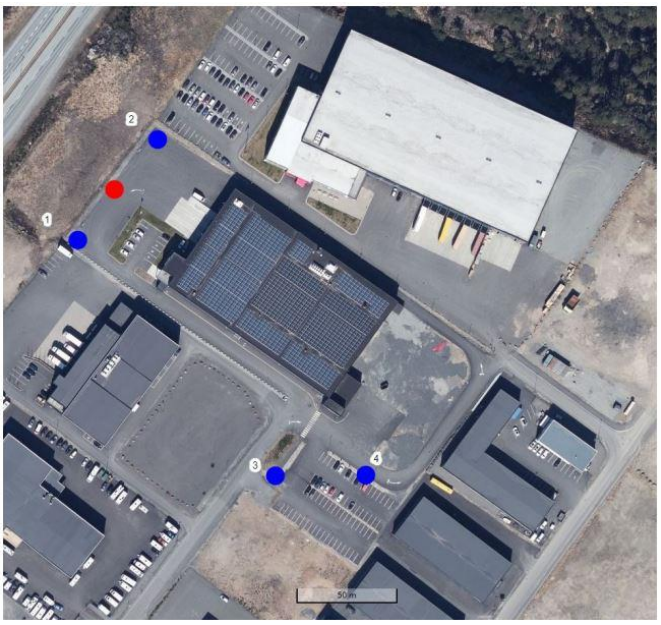

Figure 36. Potential areas for the wind energy system.

To quantify the impact of the buildings on the wind flow, the buildings were added as obstacles to the domain by modifying the grid file using Python (see the code in Appendix A). Figure 37 shows the elevation data with the buildings integrated. The corresponding mesh visualization for the xy plane and z plane is shown in Figure 34, which is heavily refined in the area of the buildings with a horizontal resolution of 0.7 m. The proposed modification increased the number of cells significantly in the digital domain (>3.1 M), which increased the simulation time to 4 hours per wind direction sector.

Figure 37. Terrain data with integrated buildings.

6.1.2 Simulation based on k-epsilon turbulence model

The convergence of the wind field simulations is evaluated by inspecting the spot and residual values for the velocity components (U1,V1,W1), the turbulent kinetic energy (KE) and its dissipation rate (EP) or the turbulent frequency (OMEG). All variables are scaled according to the min and max values. On average, the simulations for each wind direction sector converged after 230 iterations. Figure 38 shows the spot and residual values (left and right, respectively) for the parameters mentioned above plotted against the number of iterations for the 240° sector. For more sectors, see Appendix (B 1.1). The building's integration has affected the convergence criteria in establishing the wind database in the wind fields module, where the number of iterations needed for convergence has been increased due to the complexity of the flow and increased number of cells in the mesh compared to the previous research simulation [112], see also Appendix (B 1.1).

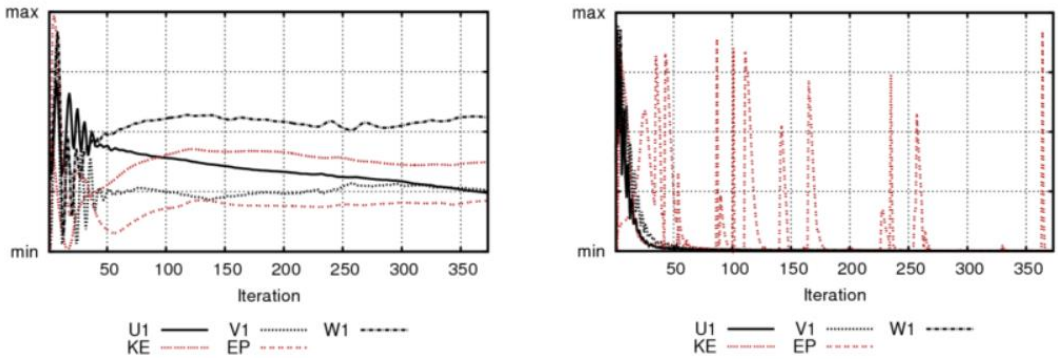

Figure 38. K-epsilon spot (left) and residual values versus the number of iterations for sector 240°.

Figure 39 shows the mean wind speed and power density at the hub height (50 m). According to the resource maps, the hub height will express a mean wind speed of around 6.2 m/s across different wind sectors, while the correspondent's power density is around 273 W/m^2. Based on the power density map, the turbulent intensity maps and the wind speed maps (see Figure 39 and Appendix B 1.2), the turbine location is not significantly affected by the turbulence produced by the buildings at the hub height across different wind sectors, which confirms the optimal selection of the single turbine location. In addition, the vertical height difference between the hub height and the top of the buildings is around 30 m which means that the turbulence induced by the buildings would require a longer horizontal distance to propagate to a higher height level.

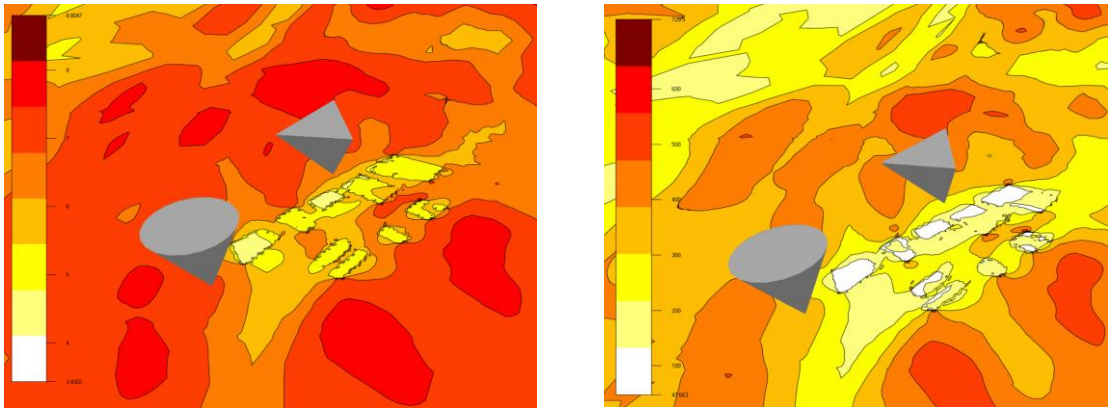

Figure 39. Mean wind speed and power density at the hub height based on the k-epsilon.

Concerning energy production, Table 7 presents the AEP results for the selected wind turbine associated with its average wind speed and full load hours (capacity factor). In comparison with previous research results, the integration of the buildings in the simulation has shown a reduction in the average wind speed across the wind sectors, where the wind speed is less by 10% compared to simulations based on raw grid and modified data. However, the capacity factor is still similar to the one from the simulation based on raw grid data. Therefore, the AEP has not shown any reduction. It should be noted that the capacity factor is the number of full load hours divided by the total number of the year's hours.

Table 7. Wind turbine's energy estimation with the k-epsilon model.

K-epsilon Simulations	Raw grid data*	Modified grid data*	Buildings integrated grid data
Wind speed [m/s]	6.96	6.94	6.25
AEP [MWh/y]	1874.5	1960	1875.3
Full load [hours]	3124	3267	3125.3

*: Previous research results

6.1.3 Simulation based on k-omega turbulence model

Using a more advanced turbulence model yielded, on average more iterations to reach convergence than a simple turbulence model. The simulations for each wind direction sector converged after an average of 250 iterations. Figure 40 shows the spot and residual values (left and right, respectively) for sector 240°. For more sectors, see Appendix (B 2.1)

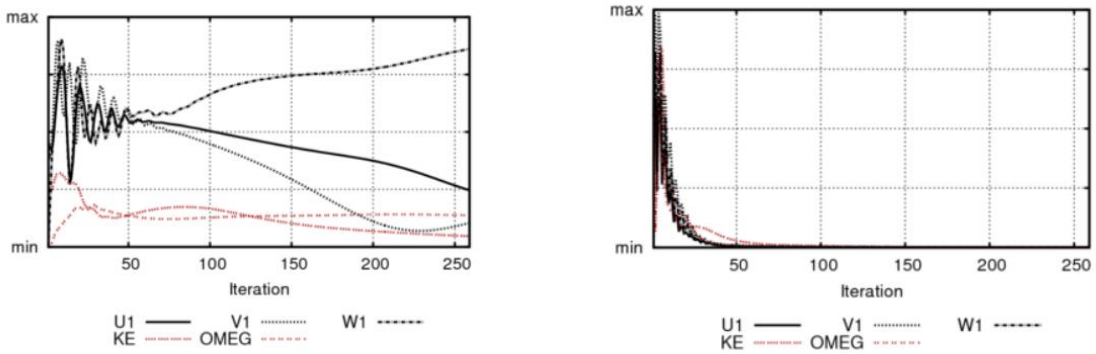

Figure 40. K-omega spot (left) and residual values versus the number of iterations for sector 240°.

Regarding the wind resource maps established using the k-omega model, Figures 41 shows the mean wind speed and power density at the hub heigh. The maps do not show a significant change in the flow compared to the maps using the k-epsilon model. However, Table 8 shows that using the k-omega model resulted in a slightly higher mean wind speed than the k-epsilon results. Nevertheless, compared to previous research results, the integration of the buildings has decreased the average wind speed by approximately 6% and the full load hours across the wind sectors by 1%, which indicates that the rated wind speed occurrence is only reduced by 1%, which is reflected in the AEP calculation.

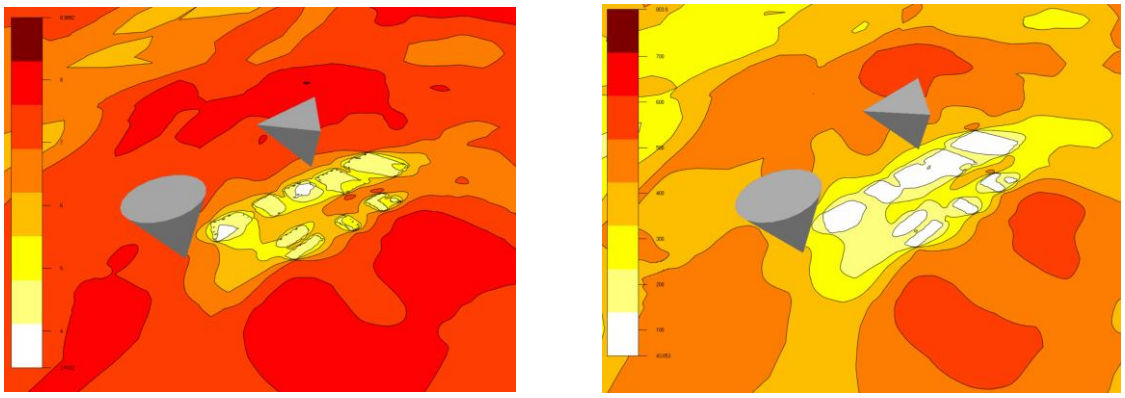

Figure 41. Mean wind speed and power density at the hub height based on the k-omega model.

Table 8. Wind turbine's energy estimation with the k-omega model.

K-omega Simulations	Raw grid data*	Modified grid data*	Buildings integrated grid data
Wind speed [m/s]	6.95	6.92	6.40
AEP [MWh/y]	1920	1942	1900.7
Full load [hours]	3200	3237	3167

*: Previous research results

6.1.4 Techno-economic analysis

As mentioned previously, Gorines has already installed a photovoltaic system integrated with battery storage and planning to install a wind turbine with a capacity of a minimum of 600 kW. in this sub-section, a life-cycle economic analysis is conducted considering the planned architecture of the system analyzing the various operational scenarios to improve the system's efficiency. Figure 42 shows the planned architecture based on the installed PV and battery storage system used and the proposed wind turbine Nordex600.

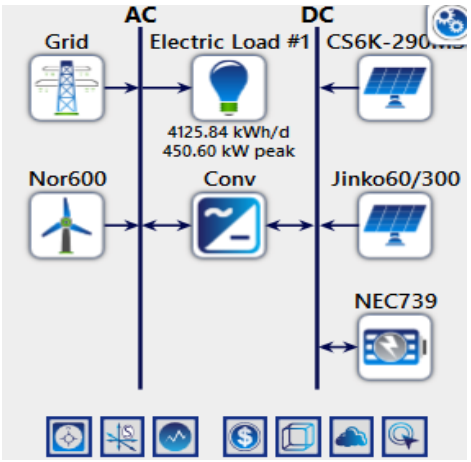

Figure 42. The planned architecture of the grid-connected hybrid system.

The system components` optimization analysis results are shown in Figure 43, which displays different options based on different combinations of the microgrid's components to meet the load requirements of the study case. The results are organized based on the most cost-effective configuration, which is ranked according to the system's increasing net present cost (NPC). However, in the case of Gorines, the second option is the one to be further analyzed as it is the option that involves all the installed and planned components.

It should be noted that all the costs and electricity prices are converted to USD.

Architecture							Cost				System		CS6K-290MS		Jinko60/300	
CS6K-290MS (kW)	Jinko60/300 (kW)	Nor600	NEC739	Grid (kW)	Conv (kW)	NPC ($)	COE ($)	Operating cost ($/yr)	Initial capital ($)	Ren Frac (%)	Total Fuel (L/yr)	Capital Cost ($)	Production (kWh/yr)	Capital Cost ($)	Production (kWh/yr)
362	251	1		800	9,999,999	$1.05M	$0.0291	-$48,492	$1.68M	84.6	0	724,000	406,997	251,400	282,787
362	251	1	1	800	9,999,999	$1.43M	$0.0398	-$38,324	$1.93M	84.6	0	724,000	406,997	251,400	282,787
362	251			800	9,999,999	$2.34M	$0.108	$105,502	$975,400	38.9	0	724,000	406,997	251,400	282,787
362	251		1	800	9,999,999	$2.71M	$0.125	$114,948	$1.23M	39.0	0	724,000	406,997	251,400	282,787

Nor600			NEC739				Conv		Grid	
Capital Cost ($)	Production (kWh/yr)	O&M Cost ($)	Autonomy (hr)	Annual Throughput (kWh/yr)	Nominal Capacity (kWh)	Usable Nominal Capacity (kWh)	Rectifier Mean Output (kW)	Inverter Mean Output (kW)	Energy Purchased (kWh)	Energy Sold (kWh)
700,000	1,707,514	5,000					0	74.0	429,313	1,278,759
700,000	1,707,514	5,000	1.98	37,667	340	340	3.51	77.1	427,477	1,272,052
							0	74.8	1,027,938	177,299
			1.98	6,039	340	340	0	74.8	1,026,015	175,142

Figure 43. system components` optimization analysis options.

Homer`s simulations show that the AEP of the selected wind turbine is below the simulated results achieved previously using Windsim, where there is a reduction of approximately 10% compared to the ones achieved using Windsim. It can be argued that Homer's simulation is conservative in estimating the AEP. However, Figure 44 shows the monthly wind turbine estimated production with the associated uncertainty. Moreover, Table 9 presents some of the turbine`s simulation results. The capacity factor is lower than the simulated one through Windsim, which explains further the reduction in the AEP. Nevertheless, adding the 600 kW wind turbine resulted in a significant increase in electricity production where the wind penetration accounted for 113%, considering the Gorines` load profile.

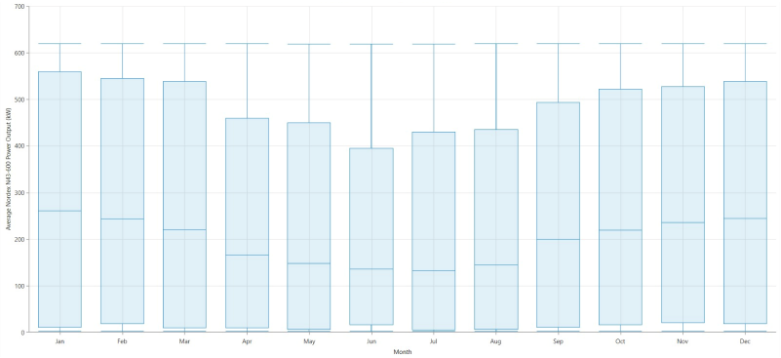

Figure 44. Wind turbine monthly power production.

Table 9. Wind turbine simulation results.

AEP [MWh/yr]	Mean output[kW]	Capacity factor [%]	Wind Penetration [%]	Hours of operation [hrs/yr]	Levelized cost [$/kWh]
1707.5	195	32.5	113	7891	0.0391

Similarly, Homer`s simulation underestimated the production of the installed PV system by 4 to 12 % compared to the original simulation done during the application phase (see section 4.5.2). Figures 45 and 46 show the monthly solar production for both solar panel types used in the installed system, with the associated uncertainty. Also, Table 10 presents the installed PV system's estimated production and economic results. Although the total installed capacity is slightly higher than the installed wind turbine, the solar penetration in the system is around 46% which counts for 40% of the wind penetration. This is expected, taking into consideration the geographical location of the studied site.

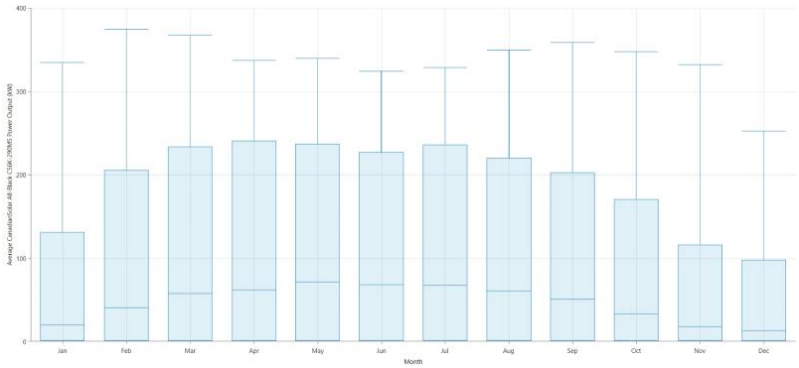

Figure 45. Canadian solar panels` monthly power production.

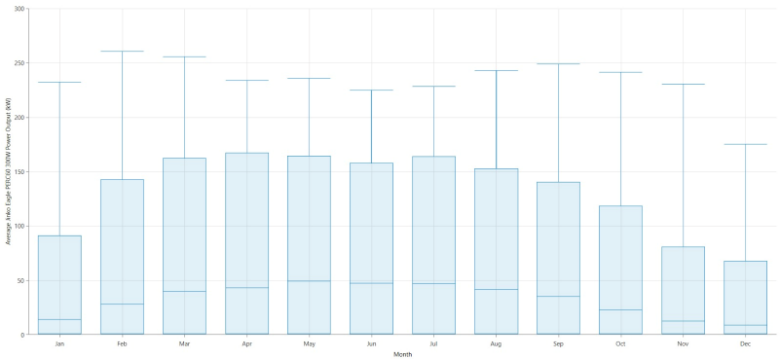

Figure 46. Jinko Eagle solar panels` monthly power production.

Table 10. PV simulation results.

PV System	Rated capacity [kW]	Mean output [kW]	Capacity factor [%]	AEP [MWh/yr]	PV penetration [%]	Levelized cost [$/kWh]
CanadianSolar	362	46.5	12.8	407	27	0.166
Jinko Eagle	252	32.3	12.8	283	18.8	0.087

Nevertheless, the total selected system life-cycle cost, which is the same as the NPC would be 1.43 M USD. This value is the present value of all the costs of installing and operating the components over the project lifetime minus the present value of all revenues it earns (see Table 11. Also, Figure 47 visualizes the total cost and revenues throughout the project's lifetime of 25 years.

Note that the operation and maintenance of the grid and the salvage are considered revenues.

Table 11.The cost summary of the selected system and its components.

Component	Capital ($)	Replacement ($)	O&M ($)	Salvage ($)	Total ($)
CanadianSolar	724,000	230,816.52	46,797.61	130,079.91	871,534.22
Grid	0.00	0.00	997,365.64	0.00	997,365.64
Jinko Eagle	251,400	80,148.17	32,499.78	45,168.63	318,879.31
NEC DSS. Battery	250,000	106,068.46	38,782.55	19,963.15	374,887.85
Nordex N43-600	700,000	223,165.15	64,637.58	125,767.87	862,034.86
System	1,925,400	640,198.29	814,648.12	320,979.57	1,429,970.60

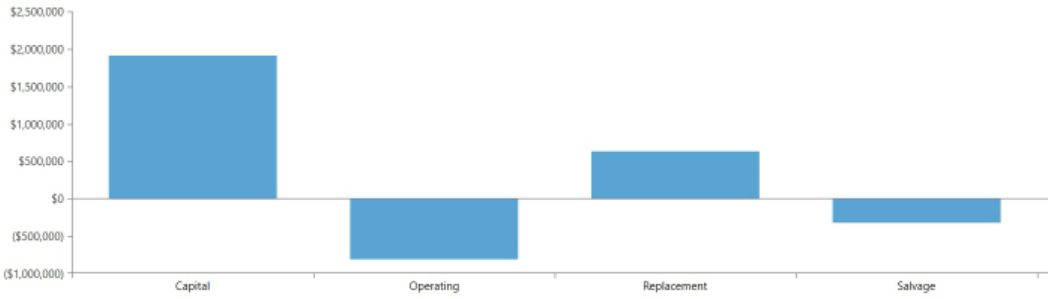

Figure 47. The total cost and revenue summary of the selected system components.

In general, having a positive NPC means that the system is not feasible, but in Gorines' case, a considerable amount of electricity production is being consumed rather than sold to the grid. Figure 48 shows the monthly production from the system components, including the grid's purchasing. Also, Table 12 shows the annual production and consumption. Renewable energy production would count for 85 % of the total production, which includes purchasing from the grid. Nevertheless, the total demand accounts for 63 % of renewable energy production and around 53% of the total production, including purchasing from the grid. In addition to that, the hybrid system would allow Gorines to sell around 45% of its total production.

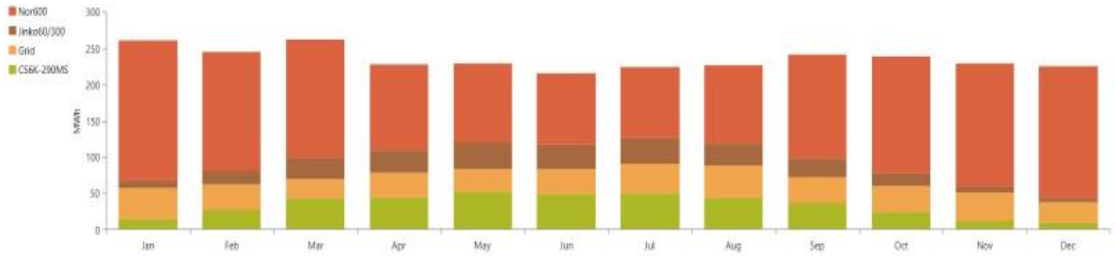

Figure 48. Monthly system components production and annual system production and consumption.

Table 12. Annual production and consumption of the selected system.

Production	kWh/yr	%	Consumption	kWh/yr	%
CanadianSolar	406,997	14.4	**AC Primary Load**	1,505,933	54.2
Jinko Eagle	282,787	10.0	**DC Primary Load**	0	0
Nordex N43-600	1,707,514	60.4	**Deferrable Load**	0	0
Grid Purchases	427,477	15.1	**Grid Sales**	1,272,051	45.8
Total	2,824,776	100	**Total**	2,777,985	100

In more detail, Table 13 presents the monthly and annual energy purchased from and sold to the grid with the estimated prices based on 2021 electricity market prices. The estimated annual revenue is around 77,150 USD based on buying from and selling the excess electricity to the grid, which is estimated to be around (1272-427=845 MWh/yr). However, more than 1.6 times this revenue Gorines would have to pay in order to purchase its total demand (1505 MWh/yr) from the grid. Adding this to the calculations would result in a profitable investment over the project`s lifetime. Figure 49 presents heat maps for hourly energy purchasing from and selling to the grid.

Moreover, the system's LCOE is 0.0398 $, which is highly affected by the system's leading LCOE (wind energy LCOE) compared to the PV production. Where the wind energy LCOE is 2 to 4 times less than the solar power LCOE

Table 13. Monthly and annual energy purchasing from and selling to the grid.

Month	Energy Purchased (kWh)	Energy Sold (kWh)	Net Energy Purchased (kWh)	Peak Load (kW)	Energy Charge $	Demand Charge $
January	42,678	108,637	-65,959	402	4,308.68	402.26
February	35,485	113,685	-78,200	387	4,438.96	386.79
March	27,308	135,151	-107,843	356	5,451.87	355.72
April	33,953	100,831	-66,877	374	3,644.33	373.93

May	30,346	107,251	-76,905	328	4,974.91	327.88
June	35,194	80,968	-45,774	326	3,185.56	326.36
July	40,564	79,539	-38,975	371	3,075.32	371.46
August	43,724	88,839	-45,115	361	4,477.89	360.83
September	36,042	110,808	-74,766	369	9,382.88	368.99
October	35,441	117,671	-82,230	394	10,539.22	394.46
November	38,589	110,714	-72,125	357	9,458.50	356.69
December	28,154	117,958	-89,805	320	18,557.50	319.63
Annual	427,477	1,272,051	-844,574	402	81,495.61	4,345.01

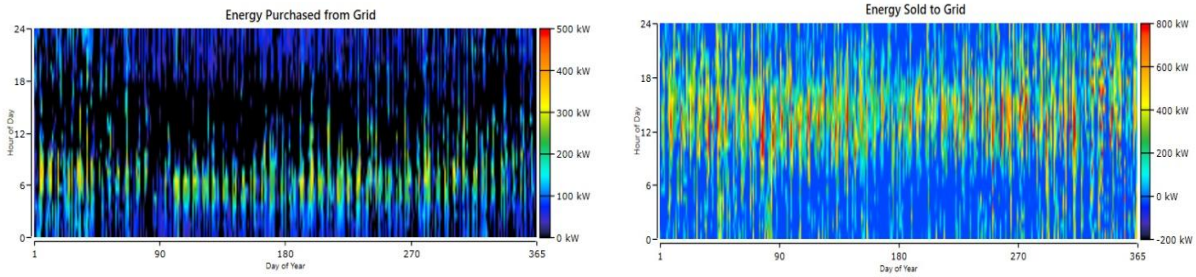

Figure 49.Hourly energy purchase and selling.

7 Conclusion

Urban environments present a challenge concerning the turbulent wind flow conditions simulation. This study has investigated the feasibility of wind power utilization by micro siting a wind energy system in an urban site for a company to become a prosumer using commercial CFD software (Windsim). In order to simulate these conditions, the surrounding buildings have been integrated with the terrain data as obstacles at the studied site, where the simulations based on this integration have been compared with simulations done on a previous research project which adapts both raw and modified terrain data for the studied site. In addition to that, the simulations employed two different turbulence models to assess their strength in simulating urban conditions. The main findings can be summarized in the following bullet points:

- The integration of buildings decreased the average wind speed at the hub height of the selected wind turbine by 10 and 6 %, considering the k-epsilon and k-omega models, respectively, compared to previous research results.
- The full load hours associated with the rated wind speed have been slightly decreased, reflecting a slight change in capacity factor, leading to a small change in the AEP calculations compared to the previous research results.
- The advanced turbulence model (k-omega) yielded a longer simulation time to reach convergence but a negligible difference in AEP and average wind speed compared with a simple turbulence model (k-epsilon).
- The simulations` convergence criteria are achieved with a higher number of iterations due to the increased number of cells with buildings in the urban digital domain.

Moreover, the conclusions of the techno-economic analysis of the planned system are summarized in the following bullet points:

- HOMER simulations are conservative in estimating the AEP for wind and solar power production, where the annual wind energy production is 10 % lower than estimated ones using Windsim, while it is lower by 4 to 12 % for solar
- Regardless of NPC being positive for the selected hybrid system, the electricity consumed by the facility, which is not included in the calculation of NPC, would improve the project's profitability over its lifetime.
- The integration of wind energy into the current system would result in having a system's LCOE of 0.0398 $, which is mainly driven by the wind energy LCOE, which is 2 to 4 times less than the solar power LCOE
- The total demand would account for 63 % of renewable energy production. In addition to that, the hybrid system would allow Gorines to sell around 45% of its total production (renewable and grid purchasing).

Reference

1. Szabó, L. *The history of using solar energy*. in *2017 International Conference on Modern Power Systems (MPS)*. 2017.
2. Europe, S.P., *Global Market Outlook For Solar Power 2021-2025*. 2021.
3. n.d., I., *Wind Energy.* 2022.
4. Vestergaard, J., L. Brandstrup, and R. Goddard, *A Brief History of the Wind Turbine Industries in Denmark and the United States.* 2004.
5. Dang, T. *Introduction, history, and theory of wind power*. in *41st North American Power Symposium*. 2009. IEEE.
6. Shahan, Z. *History of wind turbines*. 2014 [cited 2022 10/04/2022]; Available from: https://www.renewableenergyworld.com/storage/history-of-wind-turbines/#gref
7. IRENA, *Renewable capacity statistics highlights 2019*, in *Renewable capacity statistic*. 2019.
8. Lachs, W.R. and D. Sutanto, *Battery storage plant within large load centres.* IEEE Transactions on Power Systems, 1992. **7**(2): p. 762-767.
9. Erickson, L.E. and J. Cutsor, *Batteries and Energy Storage*, in *Solar Powered Charging Infrastructure for Electric Vehicles*. 2016, CRC Press. p. 67-74.
10. Fathima, A.H. and K. Palanisamy, *Optimization in microgrids with hybrid energy systems – A review.* Renewable and Sustainable Energy Reviews, 2015. **45**: p. 431-446.
11. Sinha, S. and S.S. Chandel, *Review of software tools for hybrid renewable energy systems.* Renewable and Sustainable Energy Reviews, 2014. **32**: p. 192-205.
12. Méndez, V.H., et al., *Impact of distributed generation on distribution investment deferral.* International Journal of Electrical Power & Energy Systems, 2006. **28**(4): p. 244-252.
13. Manwell, J.F., J.G. McGowan, and A.L. Rogers, *Wind energy explained: theory, design and application*. 2010: John Wiley & Sons.
14. Akorede, M.F., H. Hizam, and E. Pouresmaeil, *Distributed energy resources and benefits to the environment.* Renewable and Sustainable Energy Reviews, 2010. **14**(2): p. 724-734.
15. Tong, W., *Wind power generation and wind turbine design*. 2010: WIT press.
16. Borowy, B.S. and Z.M. Salameh, *Dynamic response of a stand-alone wind energy conversion system with battery energy storage to a wind gust.* IEEE Transactions On energy conversion, 1997. **12**(1): p. 73-78.
17. Hankins, M., *Stand-alone solar electric systems: the earthscan expert handbook for planning, design and installation*. 2010: Routledge.
18. Walford, C.A., *Wind turbine reliability: understanding and minimizing wind turbine operation and maintenance costs*. 2006, Sandia National Laboratories (SNL), Albuquerque, NM, and Livermore, CA ….
19. Song, M., et al., *Optimization of wind farm micro-siting for complex terrain using greedy algorithm.* Energy, 2014. **67**: p. 454-459.
20. Ulker, F., D. Allaire, and K. Willcox, *Sensitivity‐guided decision‐making for wind farm micro‐siting.* International Journal for Numerical Methods in Fluids, 2017. **83**(1): p. 52-72.
21. Wan, C., et al. *Optimal micro-siting of wind farms by particle swarm optimization*. in *International Conference in Swarm Intelligence*. 2010. Springer.

22. Tao, S., et al., *Optimal micro-siting of wind turbines in an offshore wind farm using Frandsen–Gaussian wake model.* IEEE Transactions on Power Systems, 2019. **34**(6): p. 4944-4954.
23. González, J.S., et al., *A review and recent developments in the optimal wind-turbine micro-siting problem.* Renewable and Sustainable Energy Reviews, 2014. **30**: p. 133-144.
24. Sumner, J., C.S. Watters, and C. Masson, *CFD in wind energy: the virtual, multiscale wind tunnel.* Energies, 2010. **3**(5): p. 989-1013.
25. Dilimulati, A., T. Stathopoulos, and M. Paraschivoiu, *Wind turbine designs for urban applications: A case study of shrouded diffuser casing for turbines.* Journal of Wind Engineering and Industrial Aerodynamics, 2018. **175**: p. 179-192.
26. Kuo, J.Y., et al., *Wind farm layout optimization on complex terrains–Integrating a CFD wake model with mixed-integer programming.* Applied Energy, 2016. **178**: p. 404-414.
27. Tominaga, Y. and T. Stathopoulos, *CFD simulation of near-field pollutant dispersion in the urban environment: A review of current modeling techniques.* Atmospheric Environment, 2013. **79**: p. 716-730.
28. Yue, J.-s., S.-p. Wu, and F.-s. Xu. *Modelling of a CFD microscale model and its application in wind energy resource assessment*. in *MATEC Web of Conferences*. 2016. EDP Sciences.
29. Tadie Fogaing, M.B., et al., *A review of wind energy resource assessment in the urban environment.* Advances in Sustainable Energy, 2019: p. 7-36.
30. Zhang, J., et al., *Comparison of numerical weather prediction based deterministic and probabilistic wind resource assessment methods.* Applied Energy, 2015. **156**: p. 528-541.
31. Simões, T. and A. Estanqueiro, *A new methodology for urban wind resource assessment.* Renewable Energy, 2016. **89**: p. 598-605.
32. Romanić, D., A. Rasouli, and H. Hangan, *Wind resource assessment in complex urban environment.* Wind Engineering, 2015. **39**(2): p. 193-212.
33. Yilmaz, S., et al., *The analysis of different PV power systems for the determination of optimal PV panels and system installation—A case study in Kahramanmaras, Turkey.* Renewable and sustainable energy reviews, 2015. **52**: p. 1015-1024.
34. Selvaraj, J. and N.A. Rahim, *Multilevel inverter for grid-connected PV system employing digital PI controller.* IEEE transactions on industrial electronics, 2008. **56**(1): p. 149-158.
35. Häggmark, S., et al., *Aspects of different distributed generation technologies, CODGUNet WP 3.* Vattenfall Utveckling Ab 2003-03, 2003. **14**.
36. Roman, E., et al., *Intelligent PV module for grid-connected PV systems.* IEEE Transactions on Industrial electronics, 2006. **53**(4): p. 1066-1073.
37. Kouro, S., et al., *Grid-connected photovoltaic systems: An overview of recent research and emerging PV converter technology.* IEEE Industrial Electronics Magazine, 2015. **9**(1): p. 47-61.
38. King, D.L., J.A. Kratochvil, and W.E. Boyson, *Photovoltaic array performance model.* 2004.
39. Stultz, J. and L. Wen, *Thermal performance testing and analysis of photovoltaic modules in natural sunlight. LSSA Project Task Report 5101-31.* Jet Propulsion Laboratory, California Institute of Technology, Pasadena, CA, 1977. **29**.
40. Skoplaki, E. and J.A. Palyvos, *Operating temperature of photovoltaic modules: A survey of pertinent correlations.* Renewable energy, 2009. **34**(1): p. 23-29.
41. Stultz, J.W., *Thermal and other tests of photovoltaic modules performed in natural sunlight.* Journal of Energy, 1979. **3**(6): p. 363-372.

42. Eckstein, J.H., *Detailed modelling of photovoltaic system components*. 1990.
43. Townsend, T.U., *A method for estimating the long-term performance of direct-coupled photovoltaic systems*. 1989.
44. Skoplaki, E., A.G. Boudouvis, and J.A. Palyvos, *A simple correlation for the operating temperature of photovoltaic modules of arbitrary mounting.* Solar Energy Materials and Solar Cells, 2008. **92**(11): p. 1393-1402.
45. Kolhe, M., S. Kolhe, and J.C. Joshi, *Economic viability of stand-alone solar photovoltaic system in comparison with diesel-powered system for India.* Energy Economics, 2002. **24**(2): p. 155-165.
46. Ali, A., N. Liu, and L. He, *Multi-party energy management and economics of integrated energy microgrid with PV/T and combined heat and power system.* IET Renewable Power Generation, 2019. **13**(3): p. 451-461.
47. Sharma, A., et al., *Performance assessment of institutional photovoltaic based energy system for operating as a micro-grid.* Sustainable Energy Technologies and Assessments, 2020. **37**: p. 100563.
48. Mehrjerdi, H., *Modeling, integration, and optimal selection of the turbine technology in the hybrid wind-photovoltaic renewable energy system design.* Energy Conversion and Management, 2020. **205**: p. 112350.
49. Loh, P.C., et al., *Autonomous Operation of Hybrid Microgrid With AC and DC Subgrids.* IEEE Transactions on Power Electronics, 2013. **28**(5): p. 2214-2223.
50. Lasseter, R.H. *Microgrids*. in *2002 IEEE power engineering society winter meeting. Conference proceedings (Cat. No. 02CH37309)*. 2002. IEEE.
51. Rolland, S. and G. Glania, *Rural electrification with renewable energy: technologies, quality standards and business models.* Alliance for Rural Electrification, Brussels, Belgium, 2011.
52. Banerjee, B. and W.W. Weaver, *Generalized geometric control manifolds of power converters in a DC microgrid.* IEEE Transactions on Energy Conversion, 2014. **29**(4): p. 904-912.
53. Solorzano del Moral, J. and M.Á. Egido. *Simulation of AC, DC, and AC-DC coupled mini-grids. In search of the most efficient system*. 2012. Ies.
54. Mahlia, T., et al., *A review of available methods and development on energy storage; technology update.* Renewable and sustainable energy reviews, 2014. **33**: p. 532-545.
55. Price, A. *The future of energy storage in a deregulated environment*. in *2000 Power Engineering Society Summer Meeting (Cat. No. 00CH37134)*. 2000. IEEE.
56. Divya, K.C. and J. Østergaard, *Battery energy storage technology for power systems—An overview.* Electric Power Systems Research, 2009. **79**(4): p. 511-520.
57. Soloveichik, G.L., *Battery technologies for large-scale stationary energy storage.* Annual review of chemical and biomolecular engineering, 2011. **2**: p. 503-527.
58. Osika, O., *Stability of micro-grids and inverter-dominated grids with high share of decentralised sources*. 2005, Zugl.: Kassel, Univ., Diss., 2005.
59. Munro, D., *Inside inverters. How they work, and what is on the market.* Renewable Energy World, 2006: p. 89-90, 92, 94.97.
60. Mohd, A., et al., *Review of control techniques for inverters parallel operation.* Electric Power Systems Research, 2010. **80**(12): p. 1477-1487.
61. International, S.E., *Photovoltaics: Design and installation manual*. 2004: New society publishers.
62. Formica, T.J., H.A. Khan, and M.G. Pecht, *The effect of inverter failures on the return on investment of solar photovoltaic systems.* IEEE Access, 2017. **5**: p. 21336-21343.

63. Antonio Barrozo Budes, F., et al., *Energy, economic, and environmental evaluation of a proposed solar-wind power on-grid system using HOMER Pro®: A case study in Colombia.* Energies, 2020. **13**(7): p. 1662.
64. Drew, D.R., et al., *The importance of accurate wind resource assessment for evaluating the economic viability of small wind turbines.* Renewable Energy, 2015. **77**: p. 493-500.
65. Kalmikov, A., et al., *Wind power resource assessment in complex urban environments: MIT campus case-study using CFD Analysis.* 2010.
66. Wang, Q., et al., *Micrositing of roof mounting wind turbine in urban environment: CFD simulations and lidar measurements.* Renewable Energy, 2018. **115**: p. 1118-1133.
67. Arteaga-López, E., C. Ángeles-Camacho, and F. Bañuelos-Ruedas, *Advanced methodology for feasibility studies on building-mounted wind turbines installation in urban environment: Applying CFD analysis.* Energy, 2019. **167**: p. 181-188.
68. Zhang, S., et al., *Study on the operation of small rooftop wind turbines and its effect on the wind environment in blocks.* Renewable Energy, 2022. **183**: p. 708-718.
69. Arteaga-López, E. and C. Angeles-Camacho, *Innovative virtual computational domain based on wind rose diagrams for micrositing small wind turbines.* Energy, 2021. **220**: p. 119701.
70. Ovgor, B., S.-K. Lee, and S. Lee, *A method of micrositing of wind turbine on building roof-top by using joint distribution of wind speed and direction, and computational fluid dynamics.* Journal of mechanical science and technology, 2012. **26**(12): p. 3981-3988.
71. Yang, B., et al., *Influence of Wind Energy Utilization Potential in Urban Suburbs: A Case Study of Hohhot.* 2020.
72. Lam, H. and H. Peng, *Development of a wake model for Darrieus-type straight-bladed vertical axis wind turbines and its application to micro-siting problems.* Renewable Energy, 2017. **114**: p. 830-842.
73. Wan, C., et al. *Optimal micro-siting of wind turbines by genetic algorithms based on improved wind and turbine models*. in *Proceedings of the 48h IEEE Conference on Decision and Control (CDC) held jointly with 2009 28th Chinese Control Conference*. 2009. IEEE.
74. Song, M., et al., *Wake flow model of wind turbine using particle simulation.* Renewable energy, 2012. **41**: p. 185-190.
75. Devibala, P. and C. Rajendran, *OPTIMAL MICRO-SITING OF WIND TURBINES IN A WIND PARK USING PARTICLE SWARM OPTIMIZATION ALGORITHM.* International Journal Eng, CS&Tech, 2012. **102**: p. 1-6.
76. Shakoor, R., et al., *Wake effect modeling: A review of wind farm layout optimization using Jensen' s model.* Renewable and Sustainable Energy Reviews, 2016. **58**: p. 1048-1059.
77. Yunwei, L., D.M. Vilathgamuwa, and L. Poh Chiang, *Design, analysis, and real-time testing of a controller for multibus microgrid system.* IEEE Transactions on Power Electronics, 2004. **19**(5): p. 1195-1204.
78. Nejabatkhah, F., Y.W. Li, and H. Tian, *Power Quality Control of Smart Hybrid AC/DC Microgrids: An Overview.* IEEE Access, 2019. **7**: p. 52295-52318.
79. Li, X., Y. Song, and S. Han. *Study on Power Quality Control in Multiple Renewable Energy Hybrid MicroGrid System*. in *2007 IEEE Lausanne Power Tech*. 2007.
80. Ou, T.-C. and C.-M. Hong, *Dynamic operation and control of microgrid hybrid power systems.* Energy, 2014. **66**: p. 314-323.
81. Miret, J., et al., *A flexible experimental laboratory for distributed generation networks based on power inverters.* Energies, 2017. **10**(10): p. 1589.

82. Zhang, C., et al., *Robustly coordinated operation of a multi-energy microgrid with flexible electric and thermal loads.* IEEE Transactions on Smart Grid, 2018. **10**(3): p. 2765-2775.
83. Prakash, M. and J. Paul, *Control of microgrid for different modes of operation.* International Journal of Engineering Research & Technology, 2016. **5**: p. 815-820.
84. Azevedo, G.M.S., et al. *Safe transient operation of microgrids based on master-slave configuration*. in *2011 IEEE Energy Conversion Congress and Exposition*. 2011.
85. Olivares, D.E., et al., *Trends in microgrid control.* IEEE Transactions on smart grid, 2014. **5**(4): p. 1905-1919.
86. Choi, J., et al., *Robust control of a microgrid energy storage system using various approaches.* IEEE Transactions on Smart Grid, 2018. **10**(3): p. 2702-2712.
87. Molzahn, D.K., et al., *A survey of distributed optimization and control algorithms for electric power systems.* IEEE Transactions on Smart Grid, 2017. **8**(6): p. 2941-2962.
88. Acharya, S., et al., *A control strategy for voltage unbalance mitigation in an islanded microgrid considering demand side management capability.* IEEE Transactions on Smart Grid, 2018. **10**(3): p. 2558-2568.
89. Zolfaghari, M., M. Abedi, and G.B. Gharehpetian, *Power Flow Control of Interconnected AC–DC Microgrids in Grid-Connected Hybrid Microgrids Using Modified UIPC.* IEEE Transactions on Smart Grid, 2019. **10**(6): p. 6298-6307.
90. Pourhossein, J., G. Gharehpetian, and S. Fathi, *Unified interphase power controller (UIPC) modeling and its comparison with IPC and UPFC.* IEEE Transactions on power delivery, 2012. **27**(4): p. 1956-1963.
91. Liu, X., P. Wang, and P.C. Loh, *A hybrid AC/DC microgrid and its coordination control.* IEEE Transactions on smart grid, 2011. **2**(2): p. 278-286.
92. Paidi, E. and T. Jain. *Hybrid AC/DC micro grid: an overview*. in *Int. Conf. on Power and Energy Systems, Kathmandu, Nepal*. 2013.
93. Aryani, D.R. and H. Song, *Coordination control strategy for AC/DC hybrid microgrids in stand-alone mode.* Energies, 2016. **9**(6): p. 469.
94. Choi, Y.-J., et al., *Optimal Operation of a Hybrid Power System as an Island Microgrid in South-Korea.* Sustainability, 2021. **13**(9): p. 5022.
95. Ghaem Sigarchian, S., et al., *Optimum design of a hybrid PV–CSP–LPG microgrid with Particle Swarm Optimization technique.* Applied Thermal Engineering, 2016. **109**: p. 1031-1036.
96. Carpinelli, G., et al., *A multi-objective approach for microgrid scheduling.* IEEE Transactions on Smart Grid, 2016. **8**(5): p. 2109-2118.
97. Maleki, A., *Design and optimization of autonomous solar-wind-reverse osmosis desalination systems coupling battery and hydrogen energy storage by an improved bee algorithm.* Desalination, 2018. **435**: p. 221-234.
98. Zhang, G., et al., *A multiobjective optimal operation of a stand-alone microgrid using SAPSO algorithm.* Journal of Electrical and Computer Engineering, 2020. **2020**.
99. Padhmanabhaiyappan, S., R. Karthik, and K. Ayyar, *Optimal utilization of interconnected RESs to microgrid: a hybrid AWO-ANFIS technique.* Soft Computing, 2020. **24**(14): p. 10493-10513.
100. Flaih, F.M., et al. *Distribution system reconfiguration for power loss minimization and voltage profile improvement using Modified particle swarm optimization*. in *2016 IEEE PES Asia-Pacific Power and Energy Engineering Conference (APPEEC)*. 2016. IEEE.
101. Sharma, P.K. and N. Sahu, *A hybrid voice identification system with fuzzy technique and ART2 neural network on BPF technique.* J. Commun. Eng. Syst, 2018. **8**(3): p. 1-6.

102. Ghorbani, N., et al., *Optimizing a hybrid wind-PV-battery system using GA-PSO and MOPSO for reducing cost and increasing reliability.* Energy, 2018. **154**: p. 581-591.
103. Maleki, A., M. Ameri, and F. Keynia, *Scrutiny of multifarious particle swarm optimization for finding the optimal size of a PV/wind/battery hybrid system.* Renewable Energy, 2015. **80**: p. 552-563.
104. Kaabeche, A., M. Belhamel, and R. Ibtiouen, *Sizing optimization of grid-independent hybrid photovoltaic/wind power generation system.* Energy, 2011. **36**(2): p. 1214-1222.
105. Turcotte, D., M. Ross, and F. Sheriff. *Photovoltaic hybrid system sizing and simulation tools: status and needs*. in *PV Horizon: Workshop on Photovoltaic hybrid systems*. 2001.
106. Khan, M.J. and M.T. Iqbal, *Pre-feasibility study of stand-alone hybrid energy systems for applications in Newfoundland.* Renewable Energy, 2005. **30**(6): p. 835-854.
107. Zhao, X., et al., *Wind power smoothing by controlling the inertial energy of turbines with optimized energy yield.* IEEE Access, 2017. **5**: p. 23374-23382.
108. Ahmed, S.D., et al., *Grid integration challenges of wind energy: A review.* IEEE Access, 2020. **8**: p. 10857-10878.
109. Ulbig, A. *Grid integration challenges of renewable energy sources and prospective solutions*. in *Swiss Federal Inst. Technol. Zurich*. 2013.
110. Suvire, G.O., M.G. Molina, and P.E. Mercado, *Improving the integration of wind power generation into AC microgrids using flywheel energy storage.* IEEE Transactions on smart grid, 2012. **3**(4): p. 1945-1954.
111. Lu, S., et al., *Integration of Wind Power and Wave Power Generation Systems Using a DC Microgrid.* IEEE Transactions on Industry Applications, 2015. **51**(4): p. 2753-2761.
112. Almostafa, H., *Micro-siting and performance simulation of an urban wind energy system using CFD*, UiA, Editor. 2021, UiA / ORIA: UiA/ ENE503.
113. Farr, T.G. and M. Kobrick, *Shuttle Radar Topography Mission produces a wealth of data.* Eos, Transactions American Geophysical Union, 2000. **81**(48): p. 583-585.
114. Silva, J., C. Ribeiro, and R. Guedes. *Roughness length classification of Corine Land Cover classes*. in *Proceedings of the European Wind Energy Conference, Milan, Italy*. 2007. Citeseer.
115. Pekkarinen, A., L. Reithmaier, and P. Strobl, *Pan-European forest/non-forest mapping with Landsat ETM+ and CORINE Land Cover 2000 data.* ISPRS Journal of Photogrammetry and Remote Sensing, 2009. **64**(2): p. 171-183.
116. Fingersh, L., M. Hand, and A. Laxson, *Wind turbine design cost and scaling model*. 2006, National Renewable Energy Lab.(NREL), Golden, CO (United States).
117. Wallbank, T., *WindSim validation study.* CFD validation in complex terrain, 2008.
118. Mjølhus, K., *Three-dimensional micro-siting of a windfarm-A CFD based analysis: A potential wind farm site in Norway, Kylland, has been analysed. An innovative 3D approach for micro-siting the wind turbines is applied together with CFD methods by using the wind farm design tool WindSim*. 2020, University of Agder.
119. Wilcox, D.C., *Turbulence modeling for CFD*. Vol. 2. 1998: DCW industries La Canada, CA.
120. Wilcox, D.C., *Formulation of the kw turbulence model revisited.* AIAA journal, 2008. **46**(11): p. 2823-2838.
121. Katic, I., J. Højstrup, and N.O. Jensen. *A simple model for cluster efficiency*. in *European wind energy association conference and exhibition*. 1986. A. Raguzzi Rome, Italy.

122. Larsen, G.C., *A simple wake calculation procedure*. 1988: Risø National Laboratory.
123. Ishihara, T., A. Yamaguchi, and Y. Fujino, *Development of a new wake model based on a wind tunnel experiment.* Global wind power, 2004. **6**.
124. Srinath, K., *Python–the fastest growing programming language.* International Research Journal of Engineering and Technology (IRJET), 2017. **4**(12): p. 354-357.
125. Singh, A., P. Baredar, and B. Gupta, *Computational Simulation & Optimization of a Solar, Fuel Cell and Biomass Hybrid Energy System Using HOMER Pro Software.* Procedia Engineering, 2015. **127**: p. 743-750.
126. Lambert, T., P. Gilman, and P. Lilienthal, *Micropower system modeling with HOMER.* Integration of alternative sources of energy, 2006. **1**(1): p. 379-385.
127. Sharma, A., *Techno-Economic Performance Evaluation of Photovoltaic based Micro-Grid with Energy Management Strategies.* 2021.

Appendices

Appendix A

Python code integrating the buildings

```
import numpy as np
import shutil
import linecache
import math
import pandas as pd
import utm
from shapely.geometry import Point, Polygon
LAT=[58.23641,58.24219]
LAT.sort()
LOG=[8.29967,8.31106]
LOG.sort()
LAT_x=[]
LOG_y=[]
for i in range (len(LAT)):
    xy=utm.from_latlon(LAT[i], LOG[i])
    LAT_x.append(xy[0])
    LOG_y.append(xy[1])
print(LAT_x[1]-LAT_x[0])
print(LOG_y[1]-LOG_y[0]
nr_x_layer=100
nr_y_layer=100
x_layers=[]
y_layers=[]
for i in np.arange(0,nr_x_layer,1):
    x_coord=float("{0:.5f". format(round(LAT_x[0]+((LAT_x[1]-LAT_x[0])/nr_x_layer)*i,5)))
    x_layers.append(f'{x_coord:.5f}'[:-1])
    y_coord=float("{0:.5f}". format(round(LOG_y[0]+((LOG_y[1]-LOG_y[0])/nr_y_layer)*i,5)))
    y_layers.append(f'{y_coord:.5f}'[:-1])
bws_file='simple_refinement.bws'
with open(bws_file, 'r') as file1:
    lines = file1.readlines()
count = 0
ll=[]
for line in lines:
    # print(count)
    ll.append(line)
    # checking string is present in line or not
    if 'i-logical'  in line:
        x_line=count
```

```
    if 'j-logical'  in line:
        y_line=count
    if 'junctions    ' in line :
        junc_line=count
    if 'volumes_obstacle   ' in line :
        vol_line=count
    count += 1

new_lines=lines.copy()
new_line_x=[]
new_line_y=[]
for i in np.arange(1,nr_x_layer):
    new_values_x= [str(item) for item in lines[x_line+2]]
    new_values_x[29]= str(1+i)
    new_values_x[35]= str(1)
    new_values_x[36]= ' '
    new_values_x[37]= ' '
    new_line_x.append( ".join(new_values_x))
    new_values_y= [str(item) for item in lines[y_line+2]]
    new_values_y[29]= str(2+i)
    new_values_y[35]= str(1)
    new_values_y[36]= ' '
    new_values_y[37]= ' '
    new_line_y.append( ".join(new_values_y))

new_line_i =".join(new_line_x)
new_lines[x_line+2]=new_line_i
new_line_j =".join(new_line_y)
new_lines[y_line+2]=new_line_j
last_layer_x= [str(item) for item in lines[x_line+3]]
last_layer_x[29]= str(nr_x_layer+2)
new_line_i =".join(last_layer_x)
new_lines[x_line+3]=new_line_i
last_layer_y= [str(item) for item in lines[y_line+3]]
last_layer_y[29]= str(nr_y_layer+2)
new_line_j =".join(last_layer_y)
new_lines[y_line+3]=new_line_j
first_coords= [str(item) for item in lines[junc_line+1]]
last_coords= [str(item) for item in lines[junc_line+16]]
x_layers.insert(0,".join(first_coords[57:68]))
x_layers.append(".join(last_coords[57:68]))
y_layers.insert(0,".join(first_coords[70:82]))
y_layers.append(".join(last_coords[70:82]))
New_coordinates=[]
```

```
for j in np.arange(1,nr_y_layer+3):
    for i in np.arange(1,nr_x_layer+3):
        print(i,j)
        if i==1 and j==1:
            new_coord=first_coords= [str(item) for item in lines[junc_line+1]]
        else:
            new_coord=first_coords= [str(item) for item in lines[junc_line+1]]
            new_coord[29]=str(i)
            new_coord[37]=str(j)
            new_coord[57:68]=str(x_layers[i-1])
            new_coord[70:82]=str(y_layers[j-1])
        New_coordinates.append(''.join(new_coord))

new_layers =''.join(New_coordinates)

new_lines[junc_line+1:junc_line+16]=''
new_lines[junc_line+1]=new_layers

#########buildings
xx_layers=[float(x) for x in x_layers]
yy_layers=[float(y) for y in y_layers]
LAT_build=[
          [58.23781,58.23825,58.23865,58.23848],
          [58.23887,58.23923,58.23910,58.23902,58.23882,58.23862,58.23880,58.23879],
          [58.23939,58.23986,58.23970,58.23922],
          [58.23998,58.24041,58.23997,58.23946],
          [58.24042,58.24055,58.24089,58.24085,58.24115,58.24081,58.24030,58.24054],
          [58.23932,58.23943,58.23953,58.23942],
          [58.23927,58.23964,58.23959,58.23936,58.23917,58.23903],
          [58.23863,58.23882,58.23857,58.23840],
          [58.23801,58.23846,58.23831,58.23787],
          [58.23771,58.23826,58.23815,58.23760]
          ]
LOG_build=[
          [8.30217,8.30157,8.30217,8.30295],
          [8.30257,8.30299,8.30340,8.30331,8.30389,8.30364,8.30309,8.30296],
          [8.30329,8.30382,8.30436,8.30380],
          [8.30416,8.30466,8.30620,8.30574],
          [8.30569,8.30491,8.30512,8.30532,8.30550,8.30747,8.30715,8.30577],
          [8.30783,8.30744,8.30755,8.30794],
          [8.30667,8.30708,8.30727,8.30702,8.30762,8.30748],
          [8.30598,8.30620,8.30697,8.30679],
          [8.30430,8.30482,8.30526,8.30475],
          [8.30489,8.30554,8.30588,8.30525]
```

```
            ]
print(len(LAT_build))
obstacles=[]
for b in range(len(LAT_build)):
    build_LAT_x=[]
    build_LOG_y=[]
    for i in range (len(LAT_build[b])):
        print(b,i,LAT_build[b][i])
        xy=utm.from_latlon(LAT_build[b][i], LOG_build[b][i])
        build_LAT_x.append(xy[0])
        build_LOG_y.append(xy[1])

    coords = list(zip(build_LAT_x, build_LOG_y))
    poly = Polygon(coords)
    # Create Point objects

    li=[str(' ')]*116
    li[72:80]='obstacle'
    li[83:86]='0.0'
    li[91:96]='0.000'
    li[99:104]='0.000'
    li[110:115]='false'
    for j in range(len(yy_layers)):
        for i in range(len(xx_layers)):
            oo=li.copy()
            point=Point(xx_layers[i], yy_layers[j])
            if point.within(poly)==True:
                print(i,j)
                oo[28]=str(i+1)
                oo[36]=str(i+2)
                oo[44]=str(j+1)
                oo[52]=str(j+2)
                oo[60]=str(1)
                oo[68]=str(2)
                oo=''.join(oo)
                obstacles.append(''.join(oo)+'\n')
Obstacles = ''.join(obstacles)
vol_line=[line for line in new_lines if 'volumes_obstacle   ' in line]
vol_line=new_lines.index(''.join(vol_line))
new_lines[vol_line+1]=''
new_lines[vol_line+1]=Obstacles
with open('new_'+bws_file, 'w') as file1:
    file1.writelines(new_lines )
```

Appendix B

1. K-epsilon simulations results

1.1 Spot and residual values versus number of iterations

Sector	Spot values	Residual values
0	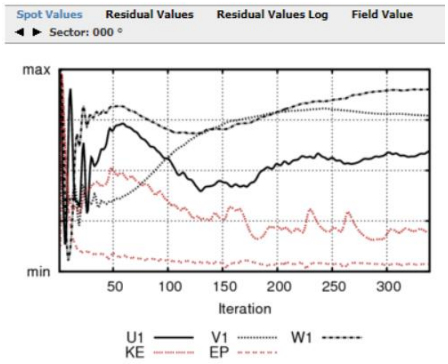	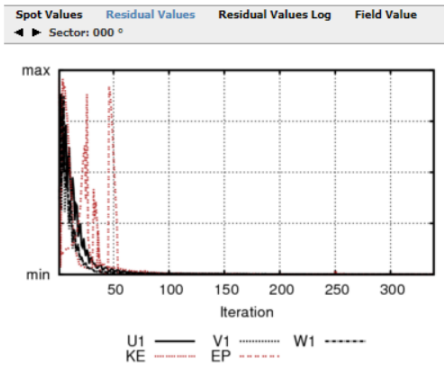
30	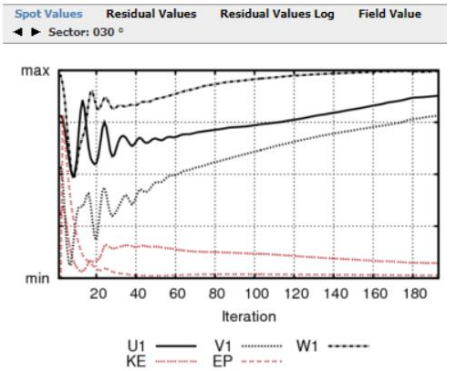	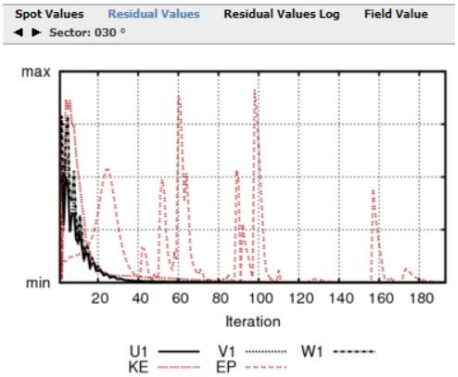
60	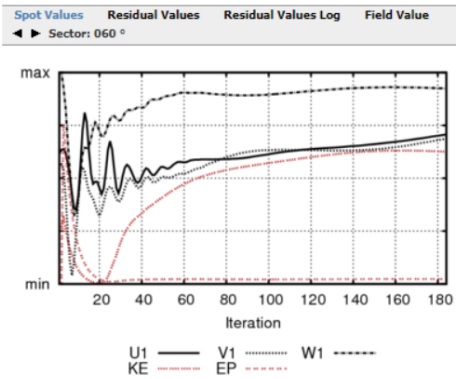	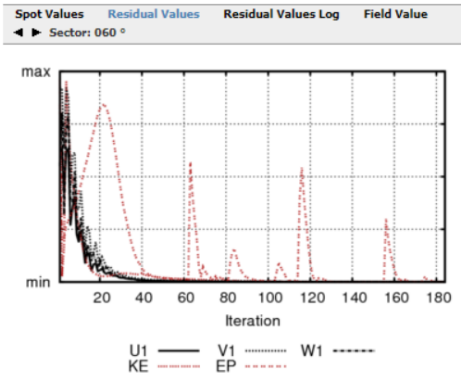
90	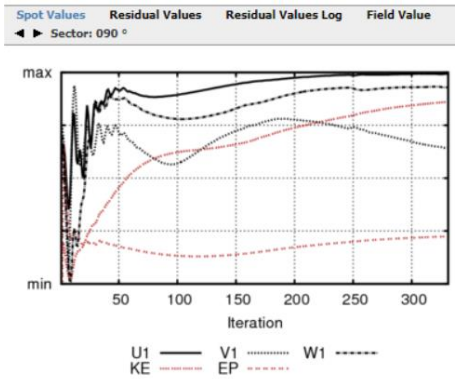	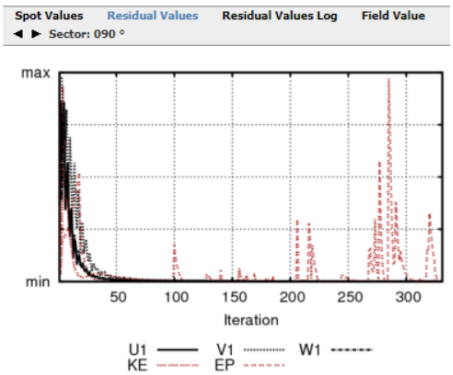

120	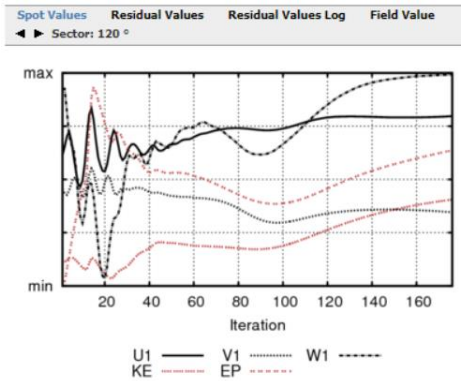	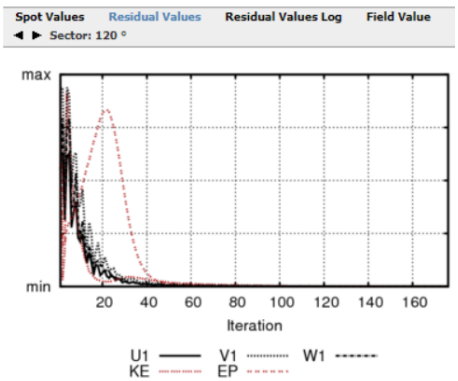
150	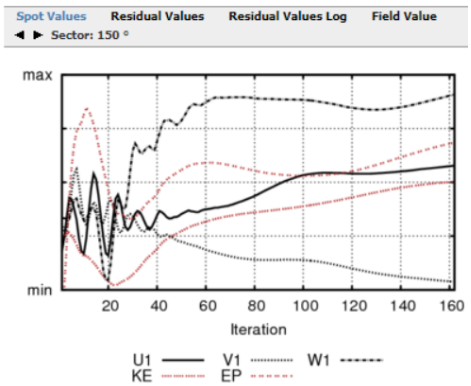	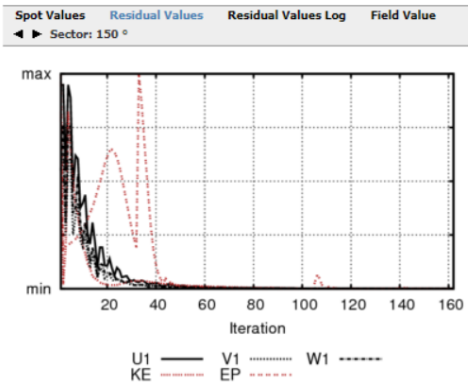
180	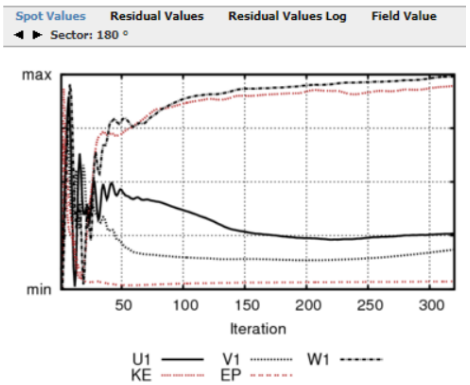	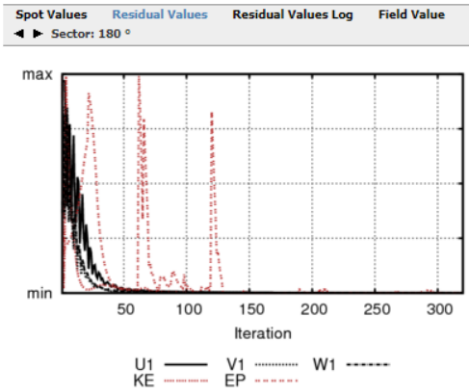
210	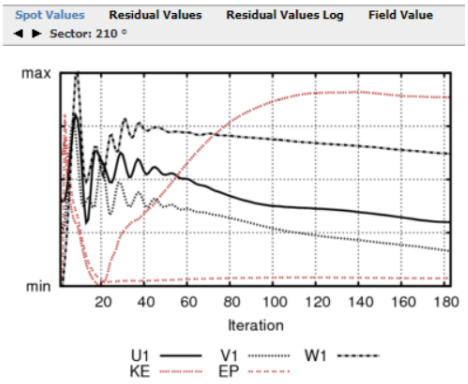	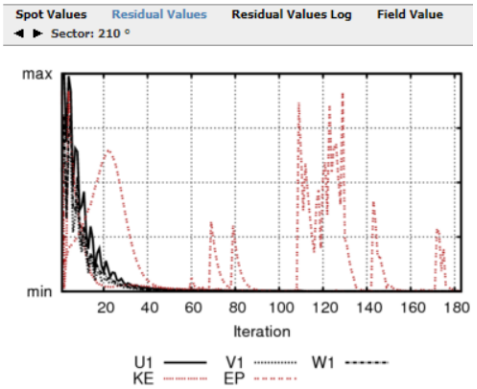

240	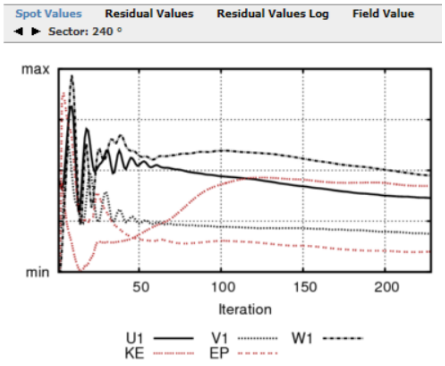	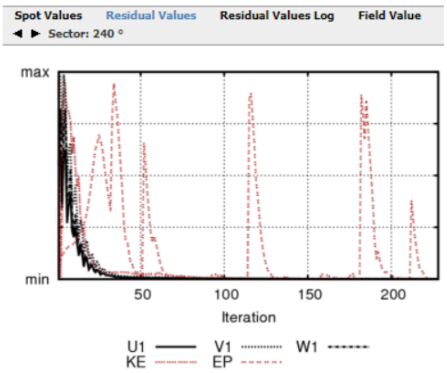
270	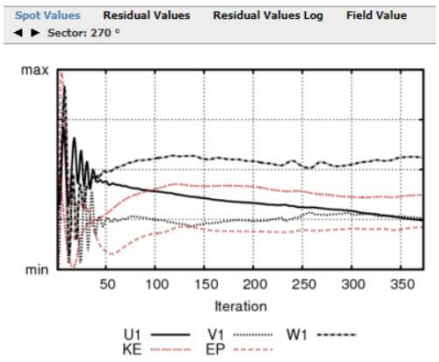	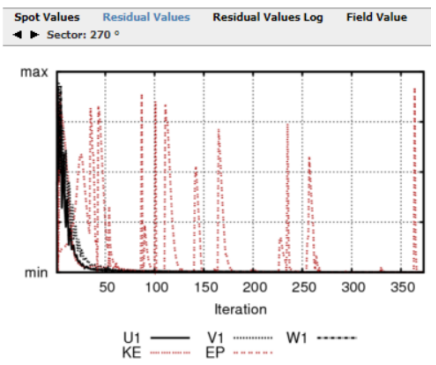
300	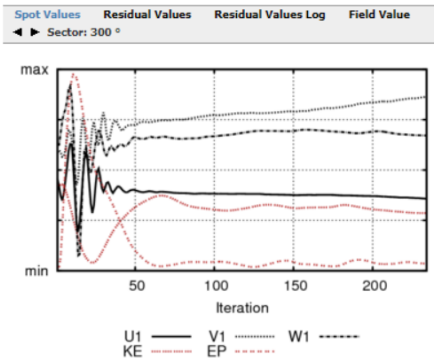	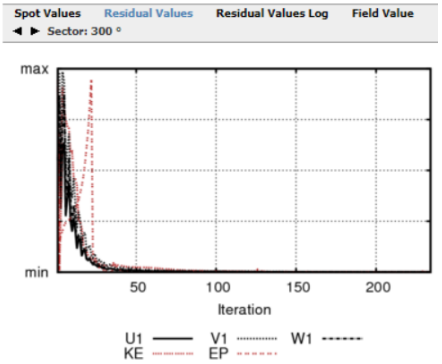
330	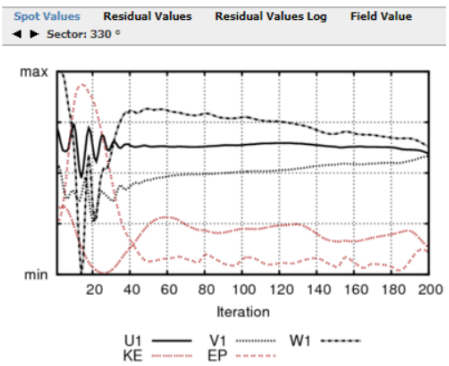	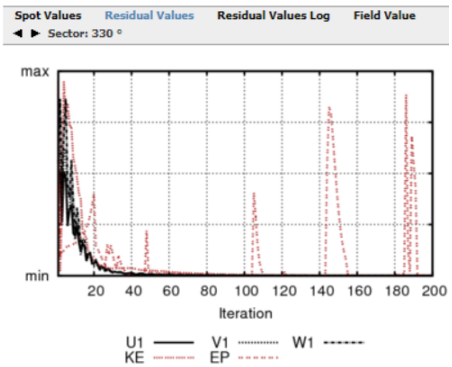

1.2 Wind speed (3D) and turbulent intensity maps

Sector	Wind speed maps	Turbulent intensity maps

0	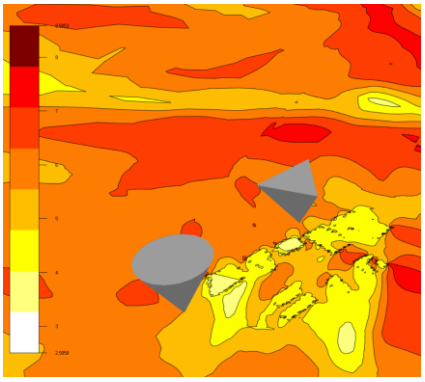	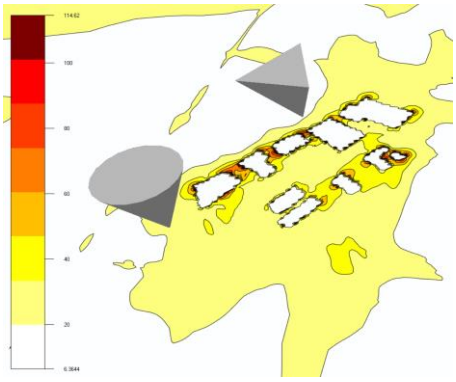
30	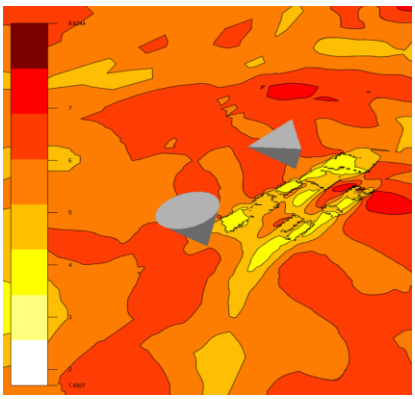	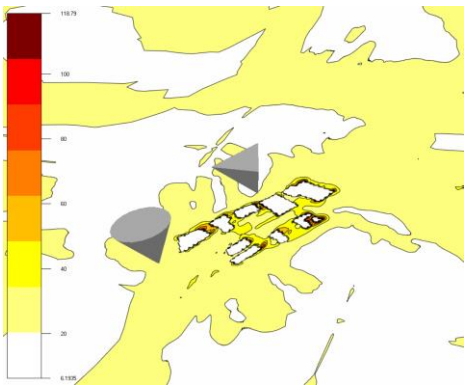
60	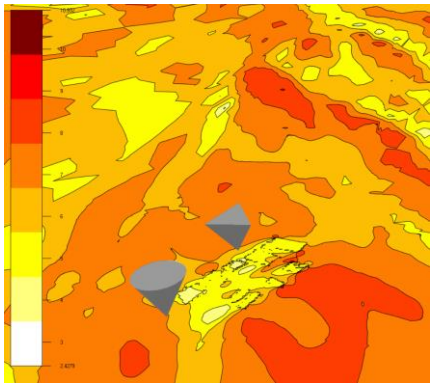	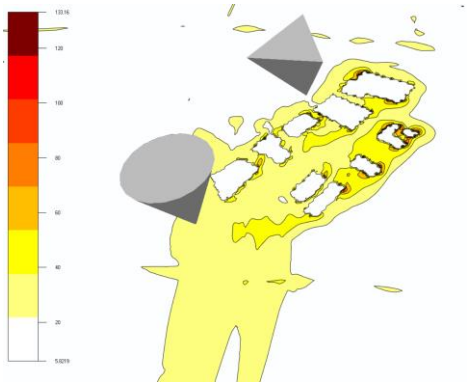
90	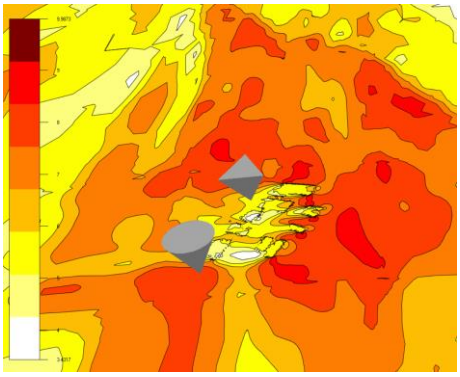	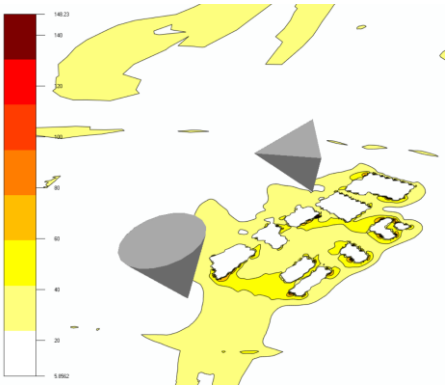

120	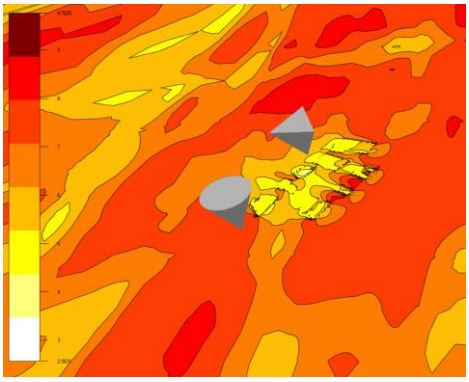	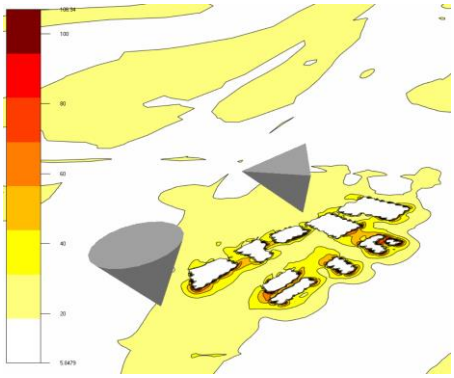
150	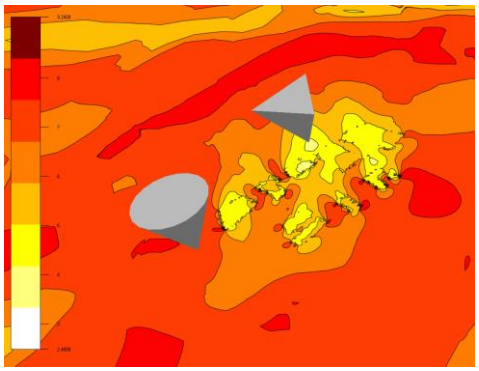	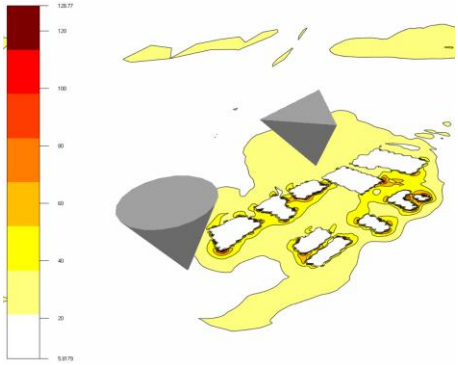
180	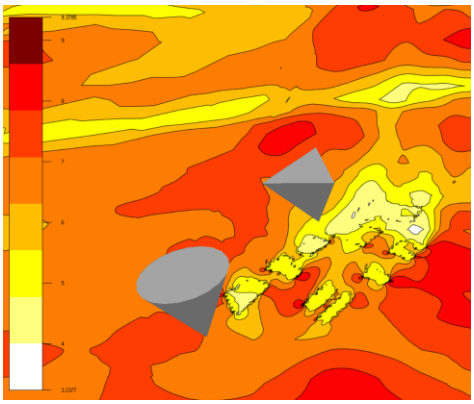	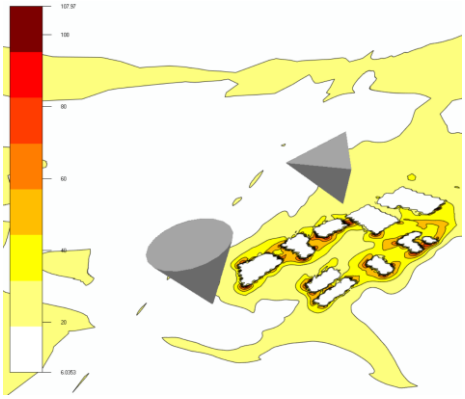
210	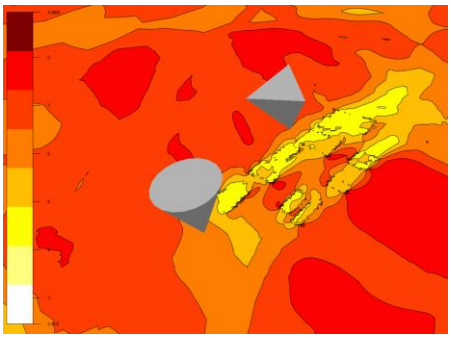	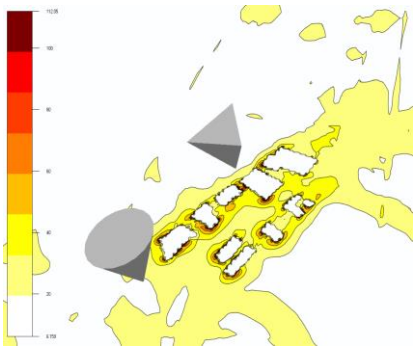

240	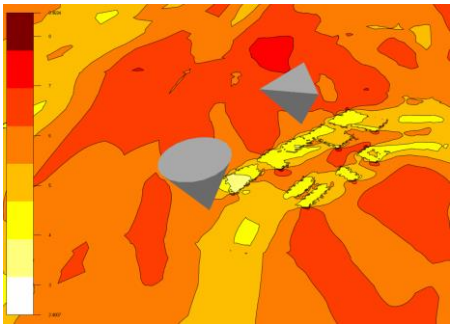	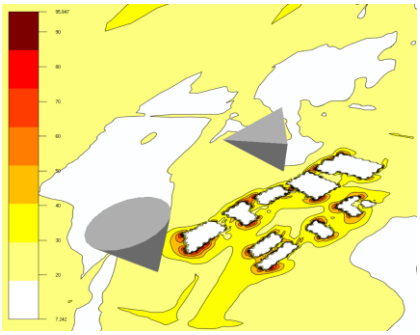
270	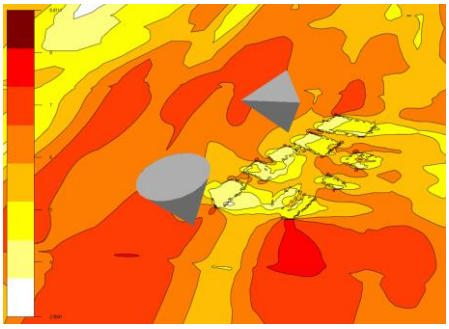	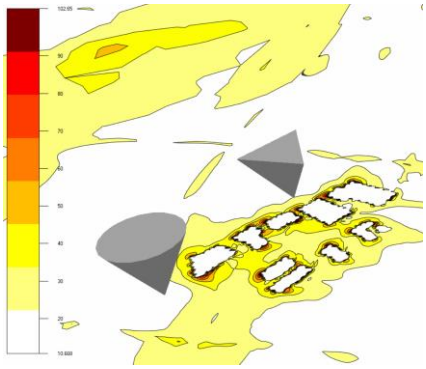
300	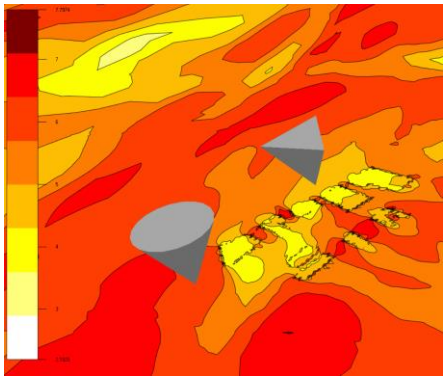	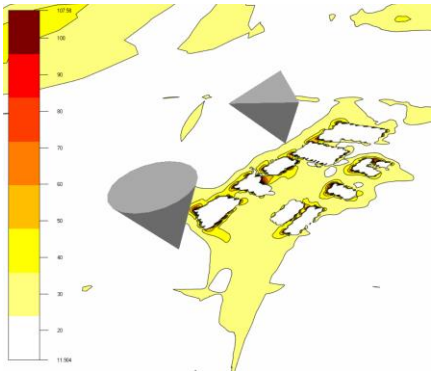
330	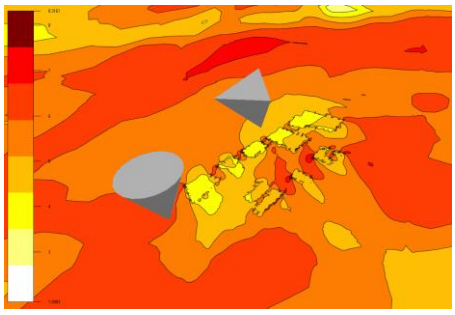	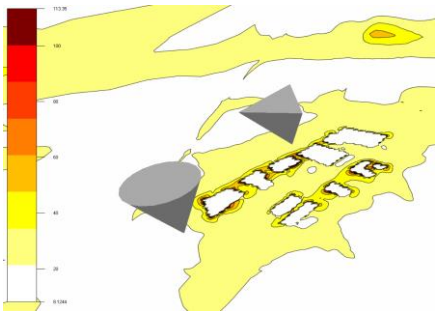

2. K-omega simulations results

2.1 Spot and residual values versus number of iterations

Sector	Spot values	Residual values

0	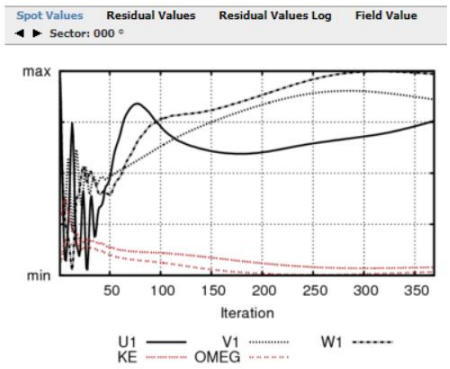 Spot Values Residual Values Residual Values Log Field Value Sector: 000 ° max min 50 100 150 200 250 300 350 Iteration U1 V1 W1 KE OMEG	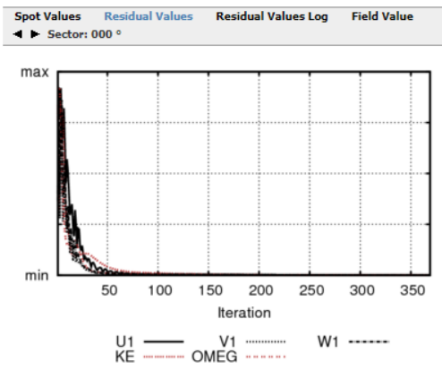 Spot Values Residual Values Residual Values Log Field Value Sector: 000 ° max min 50 100 150 200 250 300 350 Iteration U1 V1 W1 KE OMEG
30	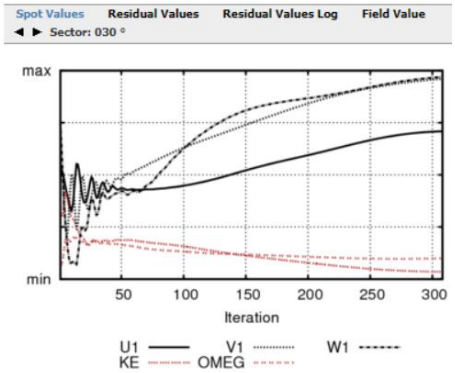 Spot Values Residual Values Residual Values Log Field Value Sector: 030 ° max min 50 100 150 200 250 300 Iteration U1 V1 W1 KE OMEG	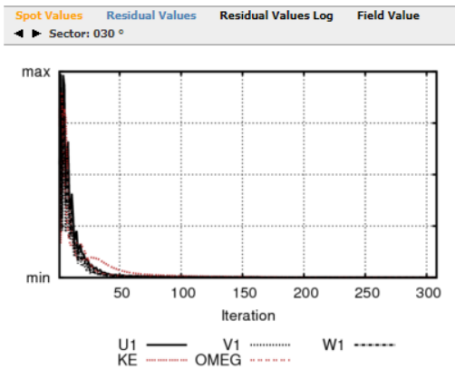 Spot Values Residual Values Residual Values Log Field Value Sector: 030 ° max min 50 100 150 200 250 300 Iteration U1 V1 W1 KE OMEG
60	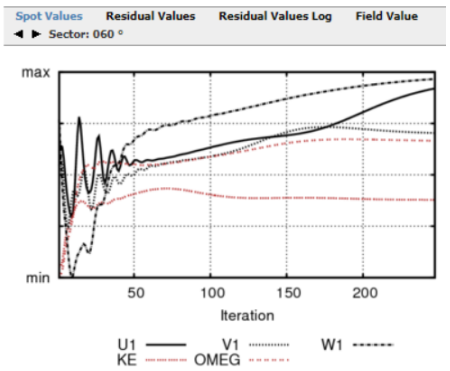 Spot Values Residual Values Residual Values Log Field Value Sector: 060 ° max min 50 100 150 200 Iteration U1 V1 W1 KE OMEG	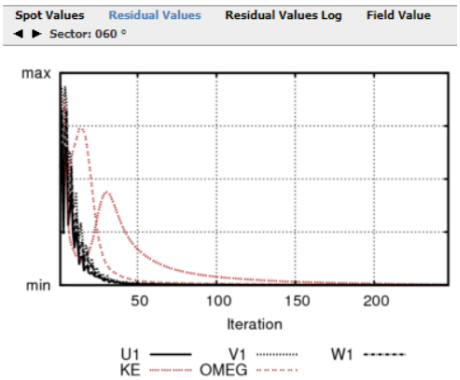 Spot Values Residual Values Residual Values Log Field Value Sector: 060 ° max min 50 100 150 200 Iteration U1 V1 W1 KE OMEG
90	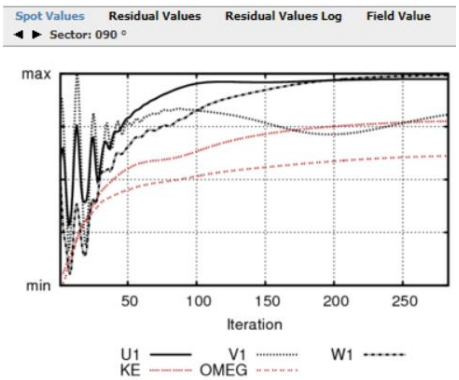 Spot Values Residual Values Residual Values Log Field Value Sector: 090 ° max min 50 100 150 200 250 Iteration U1 V1 W1 KE OMEG	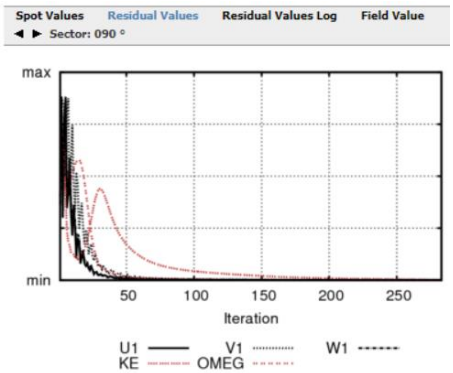 Spot Values Residual Values Residual Values Log Field Value Sector: 090 ° max min 50 100 150 200 250 Iteration U1 V1 W1 KE OMEG

120	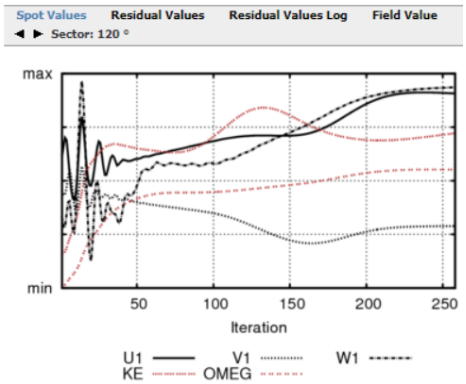	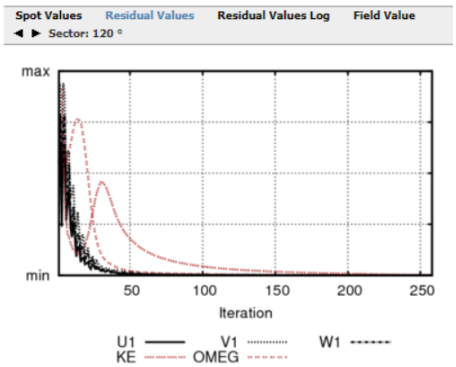
150	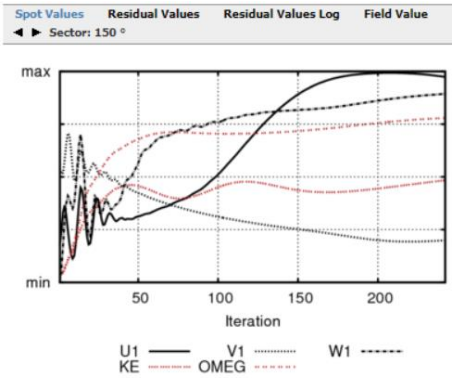	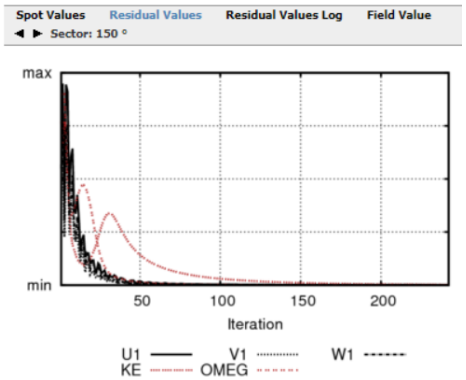
180	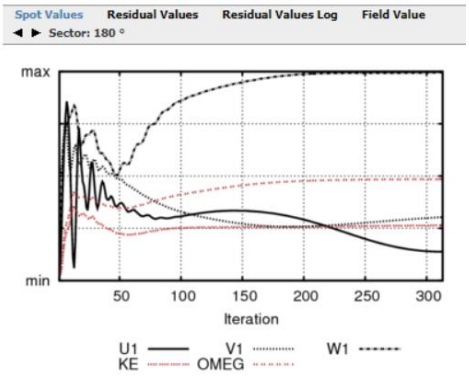	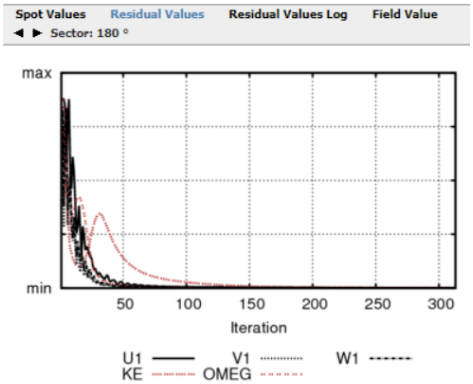
210	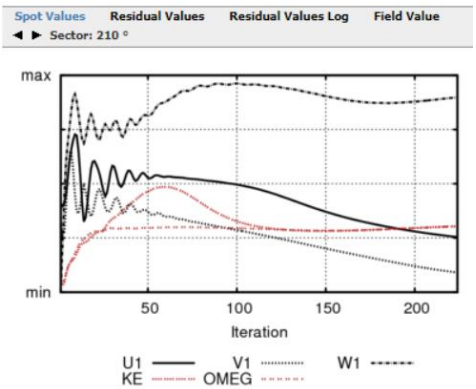	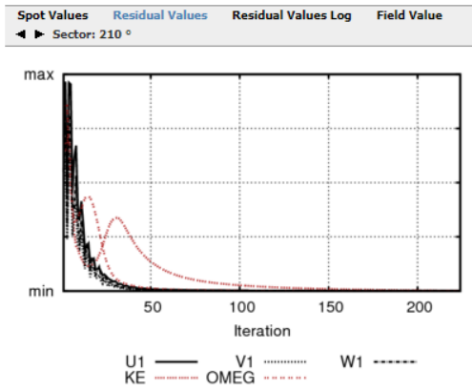

240	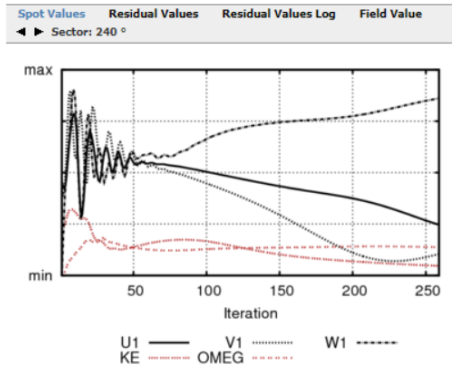	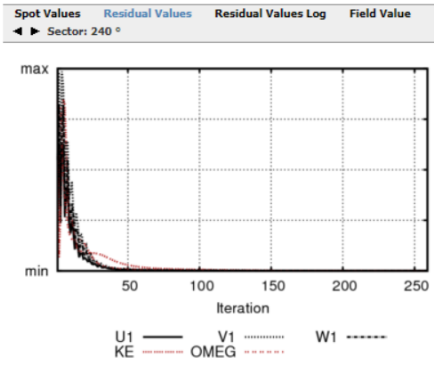
270	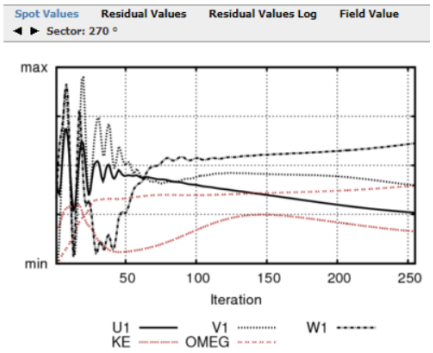	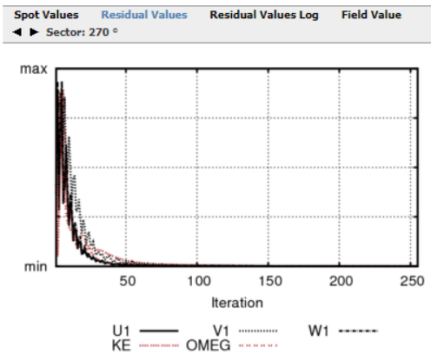
300	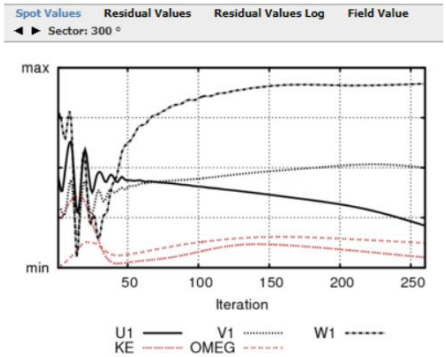	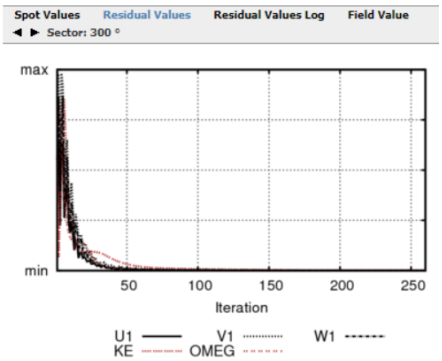
330	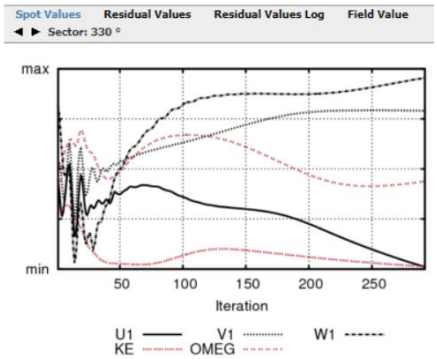	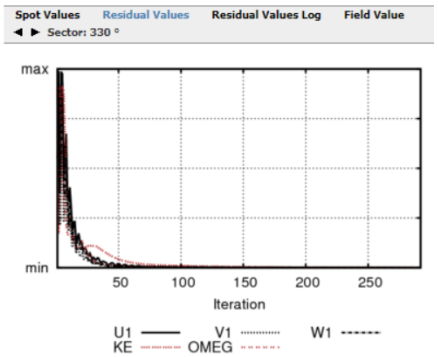

2.2 Wind speed (3D) and turbulent intensity maps

Sector	Wind speed maps	Turbulent intensity maps

0	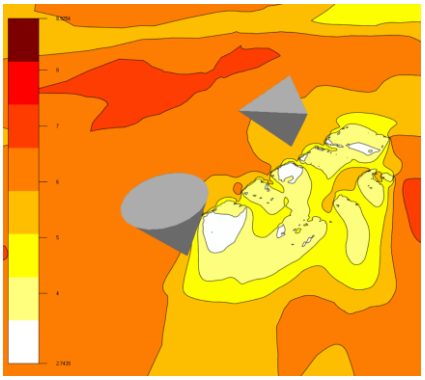	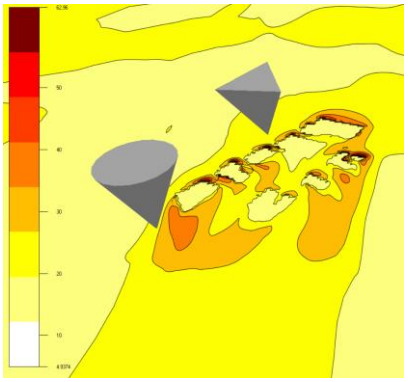
30	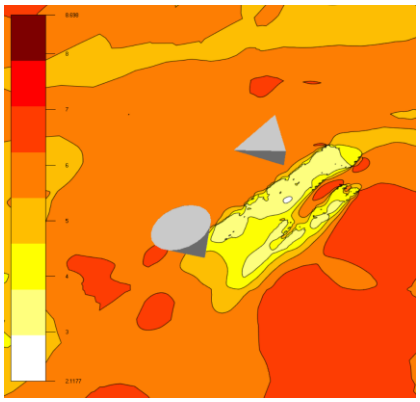	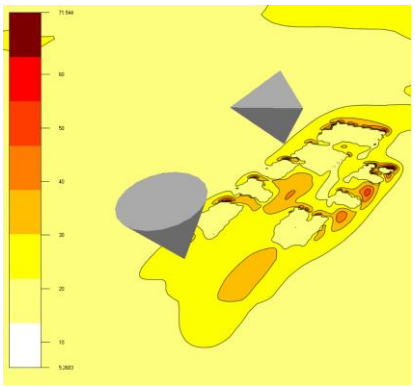
60	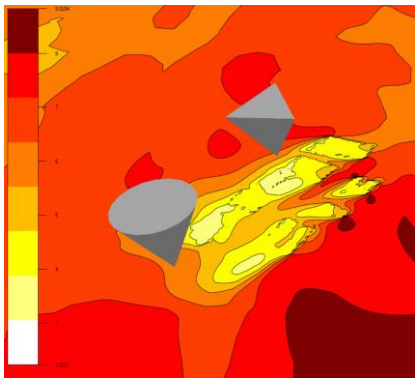	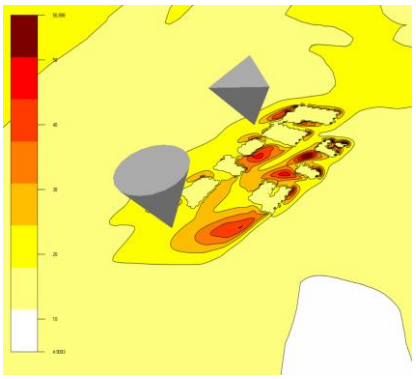
90	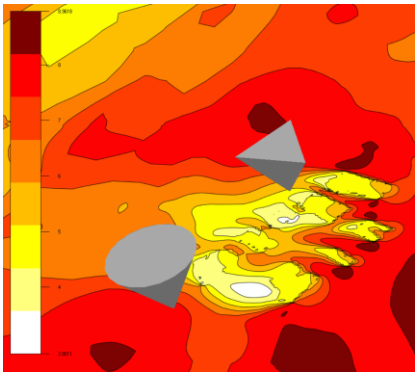	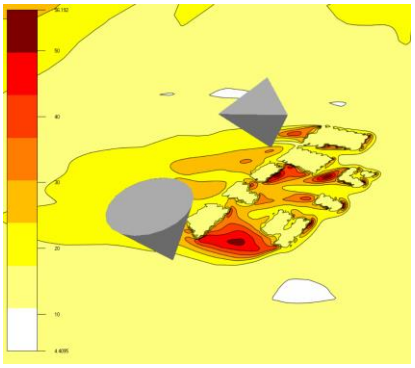

120	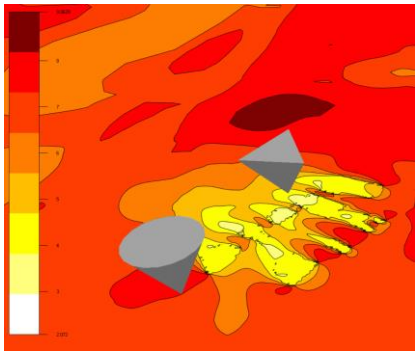	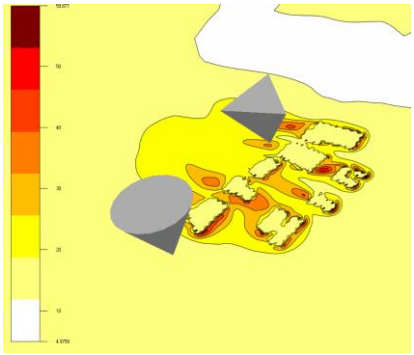
150	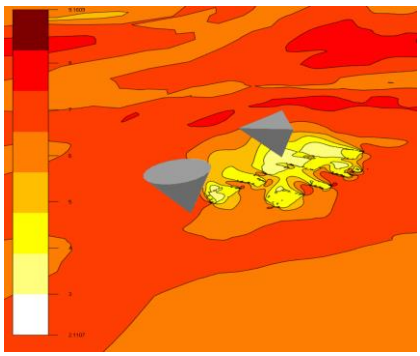	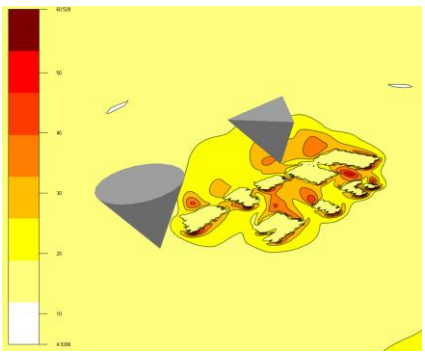
180	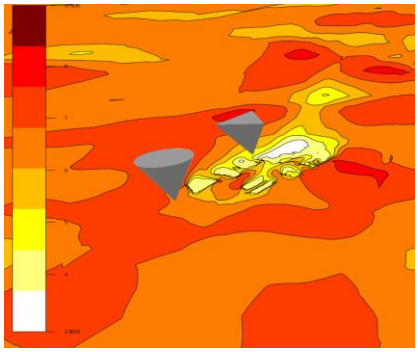	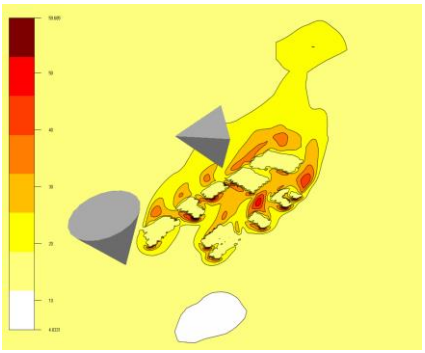
210	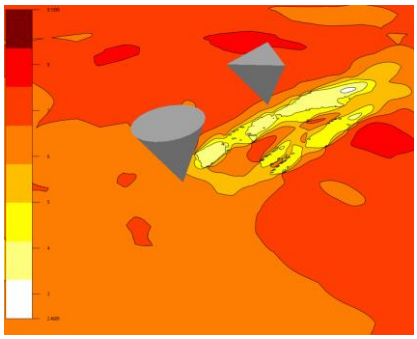	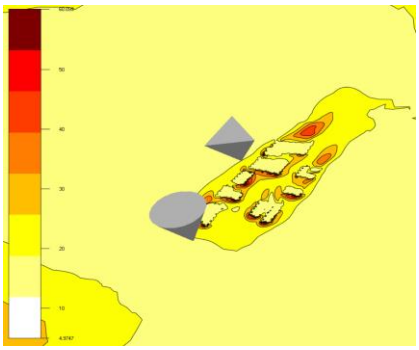
240	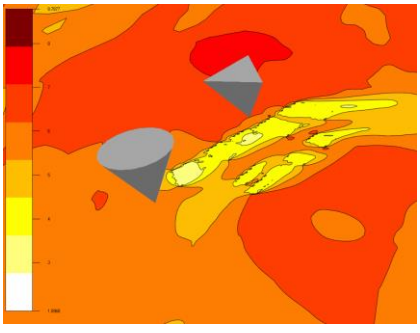	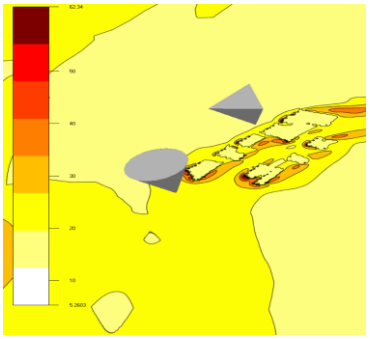

270	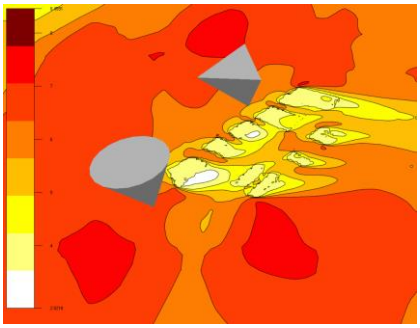	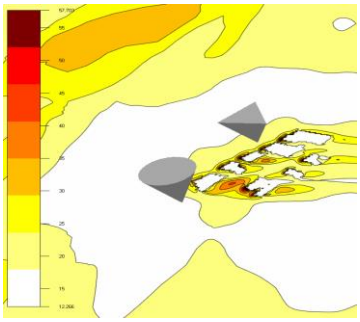
300	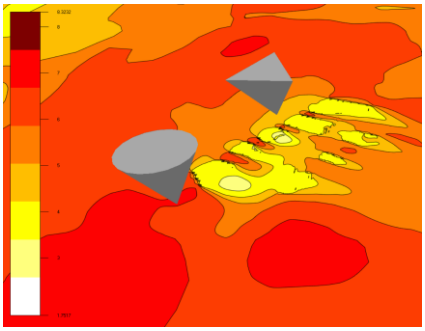	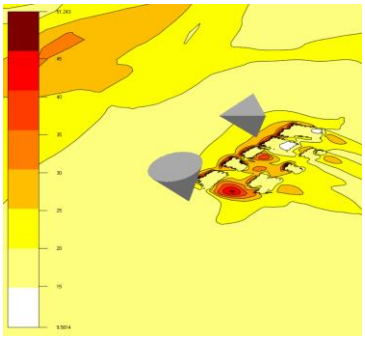
330